EXCELENCIA
MARÍA
DE MAEZTU



IFISC

Universitat de les Illes Balears

CSIC

PROCEEDINGS OF THE 2026 SURF@IFISC FELLOWSHIPS

Proceedings of the 2026 SURF@IFISC Fellowships

The SURF (Summer Undergraduate Research Fellowships) program is offered by IFISC since 2013 (only interrupted in 2020 due to the Covid-19 pandemic) with the goal of attracting excellent undergraduate students with majors compatible with IFISC research lines and offers summer research fellowships at IFISC, typically during the month of July, advised by members of IFISC.

SURF attracted for the summer of 2026 a total of 40 candidates (34 male and 6 female), out of which 6 candidates were selected, 5 of them male and 1 female candidates. The candidates came from 28 different universities belonging to 10 different countries, while the candidates were citizens of 11 different countries. The universities with more candidates were the Complutense University of Madrid and the University of Granada each with 4 applicants. More than half of the applicants, 21, were Spanish citizens, followed by India with 6 applicants.

These are the proceedings:

1. Marina Benítez Sánchez, (Supervisor: Luisa Toledo Tude), *Stochastic dynamics of a quantum oscillator under parity measurement*
2. David Vicent García, Miguel C. Soriano, *Exploring echo state networks: dynamical regimes, forecasting, control and biological reservoirs*
3. Javier Rodríguez-Escalona Sánchez, Emilio Hernández-García, *A simple model of active reproducing matter*
4. Andrea Staffieri, Albert Cabot, *Quantum synchronization and associative memories in a system of coupled quantum van der Pol oscillators*
5. Ricardo Costa Nunes, Sreetama Das and Roberta Zambrini, *Quantum reservoir computing in multiphoton Jaynes-Cummings systems*
6. Ángel Cáffaro Mendoza, Antonio Fernández Peralta, *Modeling opinion polarization: from binary choices to continuous spectra*

Stochastic Dynamics of a Quantum Oscillator under Parity Measurement

Marina Benítez Sánchez, Luísa Toledo Tude
Instituto de Física Interdisciplinar y Sistemas Complejos, IFISC (CSIC-UIB)
Campus Universitat de les Illes Balears, E-07122 Palma de Mallorca, Spain

Abstract

Quantum optics explores the intrinsically quantum properties of light, where coherent states provide a fundamental bridge between classical and quantum behavior. These states are key resources for quantum technology and information processing. In this context, the control and understanding of how to extract information from such states becomes fundamental. In this work, we investigate how different schemes used for measuring the parity of a single quantized cavity mode under coherent displacements can alter its dynamics. Specifically, we analyze three distinct physical measurement scenarios: projective parity measurements at fixed intervals, stochastic measurements at random times, and their continuous ensemble-average limit, given by the Lindblad equation. Our results illustrate how measurement can be used not only to extract information, but also to manipulate the dynamics of a system.

1 Introduction

At the beginning of the twentieth century, experimental observations such as blackbody radiation and the photoelectric effect revealed the limitations of classical physics and led to the development of quantum theory. In 1900, Max Planck postulated that the energy of the light field was quantised [1], and the principle of wave–particle duality were introduced into optics by the Einstein equation, $E = h\nu$, which relates the energy E of the light corpuscle (photon), the frequency ν of the associated electromagnetic wave, and Planck's constant h [2].

The invention of the laser in 1960 provided a highly coherent source of light and contributed to the development of quantum optics. In this framework, coherent states, originally introduced by Schrödinger, became particularly important because they provide a natural connection between the classical and quantum descriptions of light. Their properties make them fundamental in quantum optics and relevant to modern quantum technologies, including quantum information processing [1].

A major challenge in quantum systems is maintaining and controlling their quantum properties in the presence of decoherence and environmental interactions. Moreover, quantum measurements are not passive observations: extracting information from a system modifies its state through measurement back-action. In cavity quantum electrodynamics (cavity QED), where an electromagnetic field is confined inside a highly reflective cavity, quantum states can be prepared, manipulated, and monitored with high precision. This makes cavity QED a suitable platform for studying measurement-induced dynamics and for exploring measurement back-action as a resource rather than simply as a source of disturbance.

An especially interesting measurement in this context is photon-number parity, which determines whether the number of photons in the cavity is even or odd. Parity measurements can be used to characterize non-classical states [4] and, when applied to a coherent state, can project the field onto an even- or odd-parity superposition of coherent states, known as a Schrödinger cat state [5]. These non-Gaussian states are of particular interest in quantum information processing and quantum error correction [4].

When parity measurements are performed continuously, the measurement back-action becomes part of the system's dynamics rather than an isolated operation. The resulting interplay between coherent evolution, dissipation, and continuous measurement can generate complex nonlinear dynamics. This motivates the use of continuous quantum measurements not only to extract information from a system, but also to engineer its evolution.

All in all, the aim of this work is to investigate how different measurement schemes affect the dynamics of a cavity QED system. We consider three physical scenarios: projective parity measurements performed at fixed time intervals, with a displacement of amplitude α between measurements (section 3.1); stochastic parity measurements occurring at random times, which can represent either measurement uncertainty or random interactions with the environment (section 3.2); and the ensemble-averaged dynamics obtained from many stochastic trajectories, corresponding to continuous interaction with the environment (section 3.2).

2 Theoretical concepts

2.1 Quantized electromagnetic field in a cavity

To understand the physical system considered in this work, it is useful to start from the classical description of an electromagnetic field confined inside a cavity. The cavity imposes boundary conditions on the electromagnetic field, so that not every spatial field configuration is allowed. Instead, the field can be decomposed into a discrete set of normal modes, each characterized by a particular spatial distribution and oscillation frequency ω_κ. These modes provide the natural degrees of freedom of the electromagnetic field inside the cavity [3].

For an ideal cavity, the energy of the electromagnetic field can be written as a sum of independent contributions from the different modes. Each contribution has the mathematical form of the energy of a classical harmonic oscillator [2],

$$H_{\mathrm{EM}} = \sum_{\kappa} \frac{1}{2} \left(p_\kappa^2 + \omega_\kappa^2 q_\kappa^2 \right), \tag{2.1}$$

where q_κ and p_κ are the classical canonical variables associated with the κ-th electromagnetic mode. Thus, although the electromagnetic field is a spatially extended physical object, its dynamics can be reduced to a collection of independent harmonic oscillators, one for each allowed cavity mode.

In the present work, we consider only one of these modes, with frequency ω_c. This single-mode approximation allows the electromagnetic field to be described by the dynamics of a single harmonic oscillator. It is this single cavity mode that will constitute the quantum system studied throughout the rest of the work.

Quantization is performed by promoting these classical variables to Hermitian operators $\hat{q}$ and $\hat{p}$ satisfying the canonical commutation relation

$$[\hat{q}, \hat{p}] = i\hbar. \tag{2.2}$$

The Hamiltonian of the cavity mode then becomes

$$\hat{H}_{\mathrm{cav}} = \frac{1}{2} \left(\hat{p}^2 + \omega_c^2 \hat{q}^2 \right). \tag{2.3}$$

which is a mathematical description of the energy dynamics of one electromagnetic mode. The two canonical variables $\hat{q}$ and $\hat{p}$ describe the two conjugate degrees of freedom of that mode, in the same way that position and momentum describe a mechanical harmonic oscillator [8].

It is convenient to introduce the annihilation and creation operators

$$\hat{a} = \sqrt{\frac{\omega_c}{2\hbar}}\, \hat{q} + \frac{i}{\sqrt{2\hbar\omega_c}}\, \hat{p}, \tag{2.4}$$

and

$$\hat{a}^\dagger = \sqrt{\frac{\omega_c}{2\hbar}}\, \hat{q} - \frac{i}{\sqrt{2\hbar\omega_c}}\, \hat{p}, \tag{2.5}$$

which satisfy

$$[\hat{a}, \hat{a}^\dagger] = 1. \tag{2.6}$$

In terms of these operators, the Hamiltonian takes the form

$$\hat{H}_{\mathrm{cav}} = \hbar\omega_c \left(\hat{a}^\dagger \hat{a} + \frac{1}{2} \right). \tag{2.7}$$

The operator $\hat{n} = \hat{a}^\dagger \hat{a}$ counts the number of excitations of the selected cavity mode. The elementary excitation of the quantized electromagnetic field is a photon, so that $|n\rangle$ describes

a state with n photons occupying the same cavity mode, that is why it is called the photon-number operator. Consequently, the energy of the mode is quantized: its possible energy values are separated by integer and the energy eigenvalues of the cavity mode are

$$E_n = \hbar\omega_c \left(n + \frac{1}{2}\right). \tag{2.8}$$

Its eigenstates form the Fock basis,

$$\hat{n}\,|n\rangle = n\,|n\rangle\,. \qquad n = 0, 1, 2, \ldots \tag{2.9}$$

The spatial wavefunctions corresponding to the first eight of these states are illustrated in Fig. 1, displaying the characteristic spatial distributions, parity, and nodal structures associated with different excitation numbers.

.

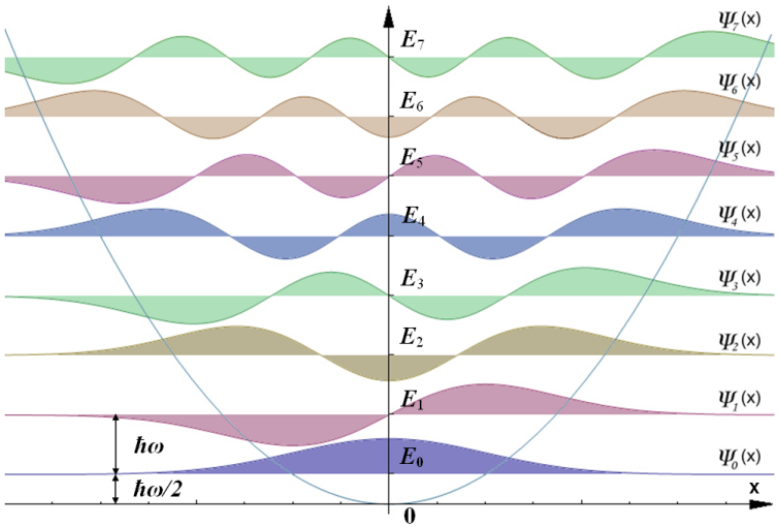

Figure 1: Wave functions of the first eight eigenstates of the quantum harmonic oscillator, corresponding to $n = 0, \ldots, 7$. The horizontal axis represents the position in units of $\sqrt{\hbar/(m\omega)}$ [6].

Furthermore, the creation and annihilation operators act on these states as

$$\hat{a}\,|n\rangle = \sqrt{n}\,|n-1\rangle\,, \qquad \hat{a}^\dagger\,|n\rangle = \sqrt{n+1}\,|n+1\rangle\,. \tag{2.10}$$

In particular, the vacuum state $|0\rangle$ is such that

$$\hat{a}\,|0\rangle = 0, \tag{2.11}$$

and, starting from the vacuum, all Fock states can be generated by repeatedly applying the creation operator,

$$|n\rangle = \frac{(\hat{a}^\dagger)^n}{\sqrt{n!}}\,|0\rangle\,. \tag{2.12}$$

This quantization gives a direct physical interpretation to the Fock states: each excitation of the cavity mode contributes an energy $\hbar\omega_c$. In this sense, the cavity mode specifies the allowed electromagnetic field configuration, while the photon number specifies the number of quantized excitations of that mode.

The Fock basis will be particularly important for the present work because photon-number parity, introduced in the following section, is directly determined by whether the photon number is even or odd.

2.2 Coherent states and phase-space representation

Although Fock states provide a natural basis for the quantized electromagnetic field, they are not the only useful description of a cavity state. In particular, coherent states provide a connection between the quantum description of the field and the classical electromagnetic field. Indeed, they are the quantum states that most closely resemble classical electromagnetic fields.

A coherent state $|\alpha\rangle$ is defined as an eigenstate of the annihilation operator [8],

$$\hat{a}\,|\alpha\rangle = \alpha\,|\alpha\rangle\,, \tag{2.13}$$

where α is a complex number.

Expanding the coherent state in the Fock basis gives

$$|\alpha\rangle = e^{-|\alpha|^2/2} \sum_{n=0}^{\infty} \frac{\alpha^n}{\sqrt{n!}}\,|n\rangle\,. \tag{2.14}$$

Consequently, the probability of finding n photons in a coherent state follows a Poisson distribution

$$P(n) = |\langle n|\alpha\rangle|^2 = e^{-|\alpha|^2}\,\frac{|\alpha|^{2n}}{n!}. \tag{2.15}$$

with mean photon number

$$\langle \hat{n}\rangle = \langle\alpha|\hat{n}|\alpha\rangle = |\alpha|^2. \tag{2.16}$$

Coherent states can be generated from the vacuum by means of the displacement operator [7],

$$\hat{D}(\alpha) = \exp\left(\alpha\hat{a}^\dagger - \alpha^*\hat{a}\right). \tag{2.17}$$

Acting on the vacuum state, it produces

$$|\alpha\rangle = \hat{D}(\alpha)\,|0\rangle\,. \tag{2.18}$$

The displacement operator changes the phase-space position of a state. In particular,

$$\hat{D}^\dagger(\alpha)\hat{a}\hat{D}(\alpha) = \hat{a} + \alpha. \tag{2.19}$$

Therefore, applying $\hat{D}(\alpha)$ to a coherent state results in

$$\hat{D}(\beta)\,|\alpha\rangle = e^{i\phi}\,|\alpha+\beta\rangle\,, \tag{2.20}$$

where the phase ϕ is physically irrelevant for the state representation. Thus, a displacement translates the state in phase space without changing its shape.

This operation is a central element of the protocol investigated in this work. In the ideal projective-measurement setting, the displacement operation is applied between successive parity measurements, producing a measurement-driven evolution of the cavity state.

It should be noted that the complex parameter α provides a natural connection between the quantum state of the cavity and the classical phase space of a harmonic oscillator. Writing

$$\alpha = X + iP, \tag{2.21}$$

the real and imaginary parts of α can be associated with two dimensionless field quadratures. Consequently, a coherent state can be represented as a localized distribution around a point (X, P) in phase space.

To represent quantum states in this phase-space picture, one can introduce the Wigner function [3], $W(\alpha)$, which is a quasiprobability distribution defined over the phase space of the cavity mode. For a density operator ρ, it is defined as

$$W(x,p) = \int_{-\infty}^{\infty} \langle x+y|\;\rho\,|x-y\rangle\, e^{2ipy}\,dy \tag{2.22}$$

where $|x\rangle$ denotes an eigenstate of the quadrature operator X. Unlike a classical probability distribution, it is not required to be positive everywhere, and therefore can contain negative regions associated with non-classical features of the quantum state.

In Fig. 2, we show some representative examples. First, the vacuum state $|0\rangle$, represented by a symmetric Gaussian centered at the origin. Then, according to Eq. (2.19), a coherent state $|\alpha\rangle$ with $\alpha = 2$ corresponds to a displaced Gaussian. Also, an even Schrödinger cat state $|\mathcal{C}_+(\alpha)\rangle$ with $\alpha = 2$, defined later in Eq. (2.29), consists of displaying classical-like lobes at $\pm\alpha$ and a central region of quantum interference. Finally, the two-photon Fock state $|2\rangle$ is characterized by a rotationally symmetric ring structure, as a consequence of Eq. (2.14).

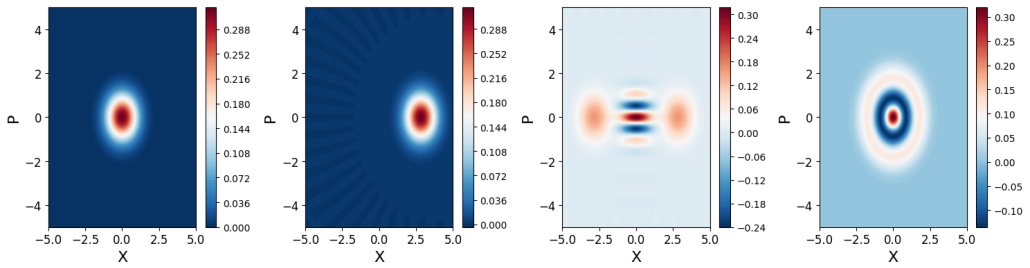

Figure 2: Wigner quasiprobability distributions in phase space for four elementary quantum states of the cavity field: (a) the vacuum state $|0\rangle$; (b) a coherent state $|\alpha = 2\rangle$; (c) an even Schrödinger cat state $|\mathcal{C}_+(\alpha = 2)\rangle$; and (d) the single-photon Fock state $|2\rangle$.

2.3 Photon-number parity

The photon-number parity is the central observable in the measurement protocol studied in this work. It distinguishes between states containing an even and an odd number of photons, so is defined as [10]

$$\hat{\Pi} = e^{i\pi\hat{n}} = (-1)^{\hat{n}}. \tag{2.23}$$

Since the Fock states are eigenstates of the photon-number operator, they are also eigenstates of the parity operator:

$$\hat{\Pi}\,|n\rangle = (-1)^n\,|n\rangle\,. \tag{2.24}$$

Thus, even-photon-number states have parity $+1$, whereas odd-photon-number states have parity -1.

The Hilbert space can therefore be decomposed into two orthogonal parity sectors,

$$\mathcal{H} = \mathcal{H}_{\text{even}} \oplus \mathcal{H}_{\text{odd}}. \tag{2.25}$$

The corresponding projectors are

$$\hat{P}_{\text{even}} = \frac{1}{2}\left(\hat{I} + \hat{\Pi}\right), \qquad \hat{P}_{\text{odd}} = \frac{1}{2}\left(\hat{I} - \hat{\Pi}\right) \tag{2.26}$$

and the probabilities of obtaining an even or odd outcome for a general state ρ in a projective parity measurement are therefore

$$p_{\text{even}} = \text{Tr}\left(\hat{P}_{\text{even}}\rho\right), \qquad p_{\text{odd}} = \text{Tr}\left(\hat{P}_{\text{odd}}\rho\right). \tag{2.27}$$

These projectors will play a central role in the following sections: they define the ideal projective measurements considered in the first part of the project and, later, provide the measurement operators used to describe continuous parity monitoring in the open quantum system.

In particular, the action of the parity operator on a coherent state follows directly from its expansion in the Fock basis (Eq. (2.14))

$$\hat{\Pi}\,|\alpha\rangle = e^{-|\alpha|^2/2}\sum_{n=0}^{\infty}(-1)^n\frac{\alpha^n}{\sqrt{n!}}\,|n\rangle\,. \tag{2.28}$$

Consequently, projecting a coherent state onto a definite parity sector selects only its even- or odd-photon-number components. The resulting states can be written as

$$|\mathcal{C}_\pm(\alpha)\rangle = \mathcal{N}_\pm\left(|\alpha\rangle \pm |-\alpha\rangle\right), \tag{2.29}$$

where $\mathcal{N}_\pm$ are normalization constants, and the signs $+$ and $-$ correspond to the even- and odd-parity sectors, respectively. The probability of obtaining each state is determined by the corresponding projective measurement probability in Eq. (2.27).

Thus, a projective parity measurement on a coherent state produces, depending on the measurement outcome, an even or odd Schrödinger cat state. These states are coherent superpositions of two states located at opposite points, α and $-\alpha$, in phase space. For sufficiently separated coherent states, their overlap becomes small, while their coherent superposition gives rise to interference features in phase space. The parity measurement therefore provides a simple mechanism through which a coherent, approximately classical-like state can be projected onto a non-classical quantum state.

An important property of the Wigner representation is its direct connection to the photon-number parity operator. In the convention used here, the Wigner function at a phase-space point α can be written as the expectation value of a displaced parity operator [2, 10], whose demonstration is developed in the appendix D

$$W(\alpha) = \frac{2}{\pi}\mathrm{Tr}\left[\rho\,\hat{D}(\alpha)\hat{\Pi}\hat{D}^{\dagger}(\alpha)\right] = \frac{2}{\pi}\left\langle \hat{D}(\alpha)\hat{\Pi}\hat{D}^{\dagger}(\alpha)\right\rangle. \tag{2.30}$$

Thus, the Wigner function can be interpreted in terms of a parity measurement performed after an appropriate displacement in phase space. This relation provides a direct connection between the main operations considered in this work and the phase-space representation of the cavity state. The sequence of displacement and parity measurements studied in the following section can therefore be interpreted simultaneously as a measurement-driven quantum dynamics and as a process that probes and modifies the phase-space structure of the cavity field.

3 Results and discussion

3.1 Projective parity measurements in a cavity QED system

The theoretical framework introduced above is now applied to an ideal measurement protocol which consists of the sequential application of a displacement in phase space and a projective measurement of photon-number parity. Starting from the vacuum state, a displacement $\hat{D}(\alpha)$ generates a coherent state (Eq. (2.18)). The parity measurement then projects the state onto either the even- or odd-parity subspace (Eq. (2.10)). The resulting state is subsequently displaced again, and the measurement is repeated. Since the outcome of each projective measurement is random, different sequences of outcomes generate different quantum trajectories. By repeating the simulation for a large number of independent realizations, ensemble-averaged quantities can also be obtained.

The protocol was simulated numerically using the `QuTiP` Python library [9] with the aim of investigating how repeated parity projections modify the state of the cavity and how the resulting dynamics can be characterized in phase space. In particular, we consider the parity probabilities, the mean field amplitude and the mean photon number, together with the Wigner function as a representation of the evolving quantum state.

Furthermore, the simulations were performed in a truncated Fock basis, as numerical calculations require a finite-dimensional Hilbert space. Since coherent states can contain contributions from large photon numbers, it is necessary to verify that the chosen cutoff is sufficiently large for the range of displacement amplitudes considered. We performed a convergence analysis by increasing N_{cut} and comparing the relevant observables, ensuring that the truncation does not introduce appreciable numerical errors in the simulations. The results bellow takes the $N_{\mathrm{cut}} = 30$.

For the first measurement, the parity expectation value can be obtained directly from the Fock-state expansion of the coherent state given in Eq. (2.14). Since parity acts on each Fock state according to Eq. (2.24), one obtains

$$\langle\hat{\Pi}\rangle_{\alpha} = \langle\alpha|\hat{\Pi}|\alpha\rangle = e^{-|\alpha|^2}\sum_{n=0}^{\infty}(-1)^n\frac{|\alpha|^{2n}}{n!} = e^{-|\alpha|^2}e^{-|\alpha|^2} = e^{-2|\alpha|^2}. \tag{3.1}$$

Thus, the parity expectation value is determined by the relative weight of the even- and odd-photon-number components of the coherent state. Using the projectors defined in Eq. (2.10), the probabilities of obtaining the two possible outcomes are

$$p_{\mathrm{even}} = \frac{1+\langle\hat{\Pi}\rangle_{\alpha}}{2} = \frac{1+e^{-2|\alpha|^2}}{2}, \qquad p_{\mathrm{odd}} = \frac{1-\langle\hat{\Pi}\rangle_{\alpha}}{2} = \frac{1-e^{-2|\alpha|^2}}{2}. \tag{3.2}$$

These expressions illustrate how the displacement amplitude controls the parity statistics. For small $|\alpha|$, the coherent state is dominated by the vacuum and low-photon-number components, with the even-photon-number sector therefore having a larger probability, as we can see in Fig. 4 (a). In contrast, for $|\alpha| \gg 1$, the exponential contribution becomes negligible and

$$p_{\mathrm{even}} \simeq p_{\mathrm{odd}} \simeq \frac{1}{2}. \tag{3.3}$$

The same behavior can be understood from the phase-space representation. As discussed in Ec. (2.29), a parity projection of $|\alpha\rangle$ produces an even or odd superposition of $|\alpha\rangle$ and $|-\alpha\rangle$. The

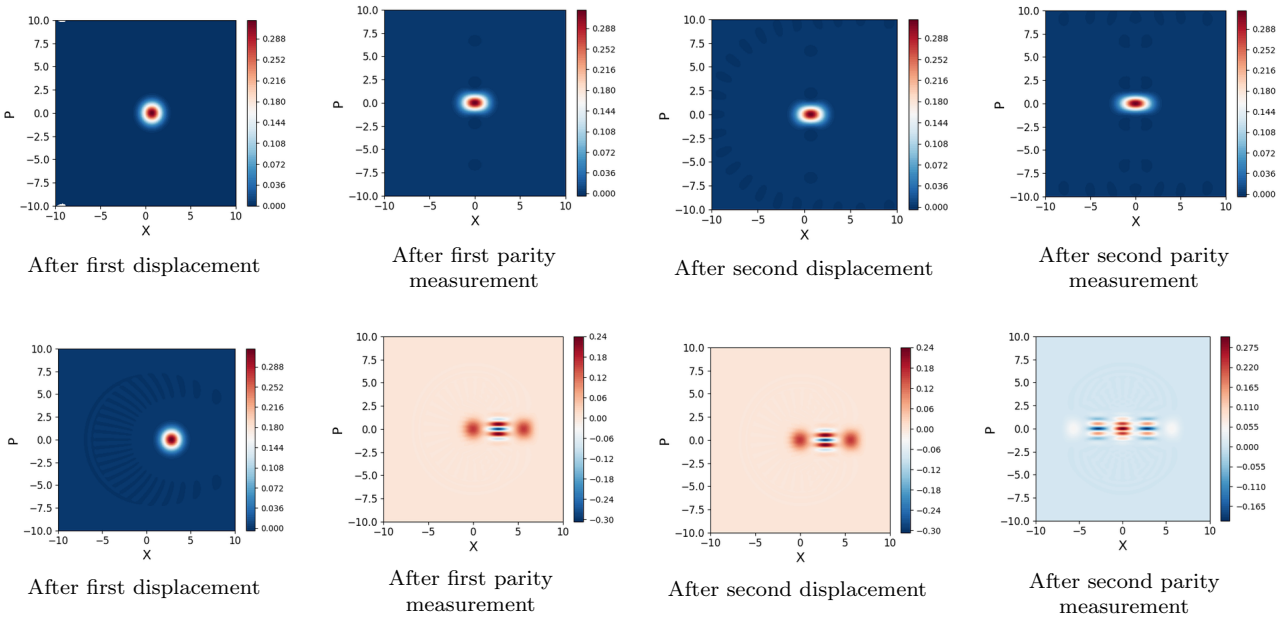

Figure 3: Wigner-function evolution under repeated displacement and projective parity measurements. The upper row corresponds to a small displacement ($\alpha = 0.5$), whereas the lower row corresponds to a larger displacement ($\alpha = 2$).

overlap between these two coherent states is

$$\langle \alpha | -\alpha \rangle = e^{-2|\alpha|^2}, \tag{3.4}$$

Therefore, for small displacements the two components strongly overlap, as can be seen in the top row of the Fig. 3, whereas for large displacements they become effectively distinguishable in phase space and the parity outcomes approach equal probabilities, as illustrated by the Wigner-function evolution in the bottom row of the Fig. 3.

After the first measurement, the situation changes because the state is no longer a coherent state but a parity-projected state. Consequently, the probabilities of the next parity outcome depends not only on the displacement amplitude but also on the result of the previous measurement.

This dependence can be illustrated analytically for a sufficiently large real displacement α, for which the overlap between $|\alpha\rangle$ and $|-\alpha\rangle$ can be neglected. If the first measurement yields the even outcome, the resulting state is approximately

$$|\psi_1\rangle \simeq \frac{1}{\sqrt{2}} \left(|\alpha\rangle + |-\alpha\rangle \right). \tag{3.5}$$

After applying the same displacement again, this state becomes

$$\hat{D}(\alpha) |\psi_1\rangle \simeq \frac{1}{\sqrt{2}} \left(|2\alpha\rangle + |0\rangle \right), \tag{3.6}$$

up to an irrelevant global phase.

The two components now have different parity content. The vacuum has purely even parity, while for sufficiently large $|\alpha|$ the coherent state $|2\alpha\rangle$ has approximately equal even and odd parity probabilities. Neglecting the small overlap between the two components, the probability of obtaining an even outcome in the second measurement is

$$p^{(2)}_{\text{even}} \simeq \frac{1}{2}(1) + \frac{1}{2}\left(\frac{1}{2}\right) = \frac{3}{4}. \tag{3.7}$$

Thus, although the first parity measurement becomes approximately unbiased for large displacements, the subsequent measurements do not. Each measurement modifies the quantum state according to its outcome, while the following displacement redistributes its phase-space components. The probability of a given parity outcome therefore depends on the previous measurement history, giving rise to different quantum trajectories even when all realizations start from the same initial state and are subjected to the same displacement sequence. However, the ensemble average

in Fig. 3.20 reveals that, despite the stochastic nature of each individual quantum trajectory, the parity probabilities converge towards well-defined deterministic values. This behavior originates from the structure of the parity projectors and the geometry of the displaced states in phase space.

To characterize how the protocol modifies the energy of the field, we computed the average photon number $\langle n \rangle = \langle a^\dagger a \rangle$, after every displacement and parity measurement, averaging over a large ensemble of independent quantum trajectories.

From Eq. (2.19) we obtain

$$D^\dagger(\alpha)\, a^\dagger a\, D(\alpha) = (a^\dagger + \alpha^*)(a + \alpha) = a^\dagger a + \alpha a^\dagger + \alpha^* a + |\alpha|^2. \tag{3.8}$$

Taking the expectation value gives

$$\langle n \rangle' = \langle n \rangle + \alpha \langle a^\dagger \rangle + \alpha^* \langle a \rangle + |\alpha|^2. \tag{3.9}$$

After every parity measurement the state is projected onto an eigenstate of the parity operator, for which $\langle a \rangle = \langle a^\dagger \rangle = 0$. Therefore,$\langle n \rangle' = \langle n \rangle + |\alpha|^2$.

For the simulations presented here, where $\alpha = 2$, every displacement injects exactly$|\alpha|^2 = 4$ photons on average, producing the sequence 4, 8, 12, 16, 20, which is in agreement with the numerical results in Fig. 4 (b).

Unlike the displacement operation, the parity measurement does not modify the average energy of the field. This follows from the fact that the photon-number operator commutes with the parity operator,

$$[a^\dagger a, \Pi] = 0 \tag{3.10}$$

In fact, the measurement only redistributes the state within either the even or odd Fock subspace, without creating or destroying photons on average.

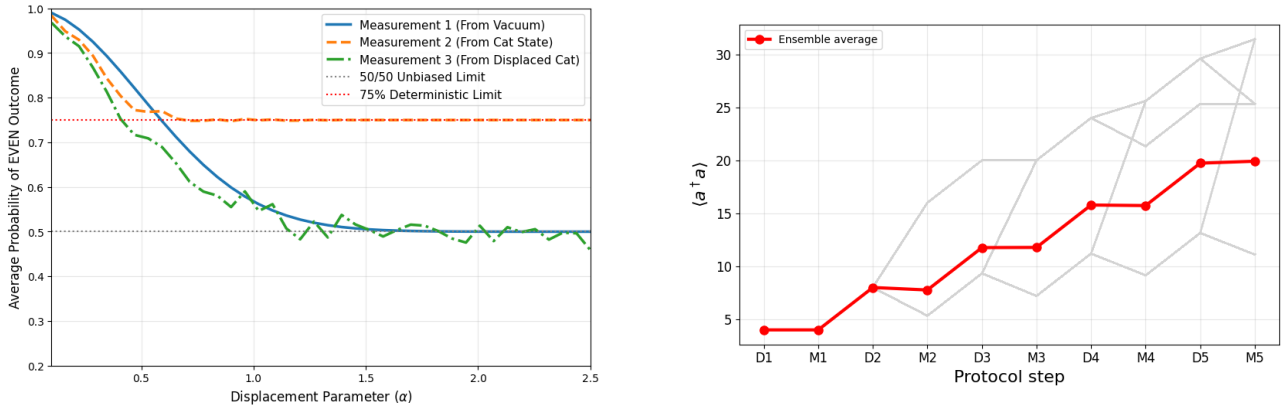

(a) (b)

Figure 4: (a) Average probability of obtaining an even parity outcome as a function of the displacement parameter α for the first three successive steps of the protocol. (b) Mean photon number $\langle \hat{n} \rangle$ after successive displacement and parity-measurement steps for $\alpha = 2$. The red curve shows the ensemble average over independent quantum trajectories, while the grey lines are trajectories illustrating individual realizations.

However, the individual quantum trajectorie shown in Fig. 4 (b) behave very differently. Each parity measurement randomly projects the system onto either the even- or odd-parity subspace, causing the photon number of a single realization to jump upward or downward depending on the measurement outcome. These stochastic jumps correspond to the quantum measurement back-action and are shown as the gray trajectories in the figure.

When averaging over the ensemble of trajectories, these positive and negative fluctuations cancel statistically, producing the deterministic staircase followed by the red curve in Fig. 4 (b). The small deviations observed after each measurement originate from the finite number of Monte Carlo trajectories used in the simulation and decrease as the ensemble size increases.

3.2 Continuous parity monitoring and open-system dynamics

While the projective-measurement scheme relies on a sequence of discrete, strong interactions, continuous monitoring of the cavity constitutes an entirely different physical setup that must be modeled within the framework of open quantum systems. Rather than describing the dynamics through individual projective measurements separated by unitary operations, the interaction with the environment is represented by a continuous weak measurement process [11].

The dynamics of an open quantum system can be described by the Lindblad master equation

$$\frac{d\rho}{dt} = -i[\hat{H}, \rho] + \sum_k \mathcal{D}[\hat{L}_k]\rho, \tag{3.11}$$

where

$$\mathcal{D}[\hat{L}]\rho = \hat{L}\rho\hat{L}^\dagger - \frac{1}{2}\left\{\hat{L}^\dagger\hat{L}, \rho\right\} \tag{3.12}$$

is the Lindblad dissipator. Here, $\hat{H}$ describes the coherent evolution of the cavity, while the operators $\hat{L}_k$ describe the coupling to the environment.

For the present system, the environment is assumed to continuously monitor the photon-number parity. The two possible measurement outcomes correspond to the even- and odd-parity subspaces introduced previously. The corresponding collapse operators are therefore chosen as

$$\hat{L}_{\text{even}} = \sqrt{\gamma}\,\hat{P}_{\text{even}}, \qquad \hat{L}_{\text{odd}} = \sqrt{\gamma}\,\hat{P}_{\text{odd}}, \tag{3.13}$$

where γ is the measurement rate, so that larger values of γ lead to more frequent measurement events, whereas smaller values approach the weak-monitoring regime. The projectors are those defined in Eq. (2.26). Because the parity operator commutes with the photon-number operator, Ec. (3.10), this continuous monitoring acts as a quantum non-demolition (QND) [14] measurement that distinguishes between the two parity sectors while strictly conserving the photon-number distribution of the cavity field.

In fact, substituting Eq. (3.13) into the Lindblad equation gives the unconditional evolution (Appendix C)

$$\frac{d\rho}{dt} = -i[\hat{H}, \rho] + \frac{\gamma}{2}\left(\hat{\Pi}\rho\hat{\Pi} - \rho\right). \tag{3.14}$$

This equation describes a purely measurement-induced decoherence process. In particular, since $\hat{\Pi}^2 = \hat{I}$, it does not systematically change the populations of the two parity subspaces or exchange energy with the cavity. Instead, the continuous interaction with the environment progressively removes coherences between elements of ρ of different parity.

Although Eq. (3.14) provides a deterministic description of the density matrix, the same evolution can be viewed as the ensemble average of stochastic quantum trajectories. This alternative description is known as a quantum-jump unraveling of the master equation.

In this regard, the state of the cavity is conditioned on a particular measurement record and is denoted by $\rho_c(t)$ or $|\psi_c(t)\rangle$. During a small time interval dt, a detection event in channel k occurs with probability

$$p_k = dt\,\langle\hat{L}_k^\dagger\hat{L}_k\rangle_c, \tag{3.15}$$

where the subscript c indicates that the expectation value is evaluated for the current trajectory. When a jump occurs, the state is updated according to the corresponding collapse operator, concretely the jumps correspond to stochastic projections onto the even- and odd-parity sectors

$$|\psi_c\rangle \longrightarrow \frac{\hat{L}_k\,|\psi_c\rangle}{\sqrt{\langle\hat{L}_k^\dagger\hat{L}_k\rangle_c}}. \tag{3.16}$$

Between detection events, the state evolves continuously according to an effective Hamiltonian,

$$\hat{H} = i\left(\alpha\hat{a}^\dagger - \alpha^*\hat{a}\right), \tag{3.17}$$

where the parameter α therefore determines the strength of the coherent driving.

In the numerical simulations, the stochastic dynamics is obtained using the Monte Carlo wavefunction method implemented in QuTiP through `mcsolve`. Each run produces one possible realization of the monitored cavity dynamics. Since the jump times and measurement outcomes are stochastic, independent runs starting from the same initial state generally produce different trajectories, as demonstrated in Fig. 5.

To characterize individual trajectories, we monitor the mean photon number, since this observable provides a direct measure of the energy stored in the cavity and makes the stochastic effects of the measurement particularly visible

$$\langle \hat{n} \rangle_c = \langle \psi_c(t) | \hat{a}^\dagger \hat{a} | \psi_c(t) \rangle. \tag{3.18}$$

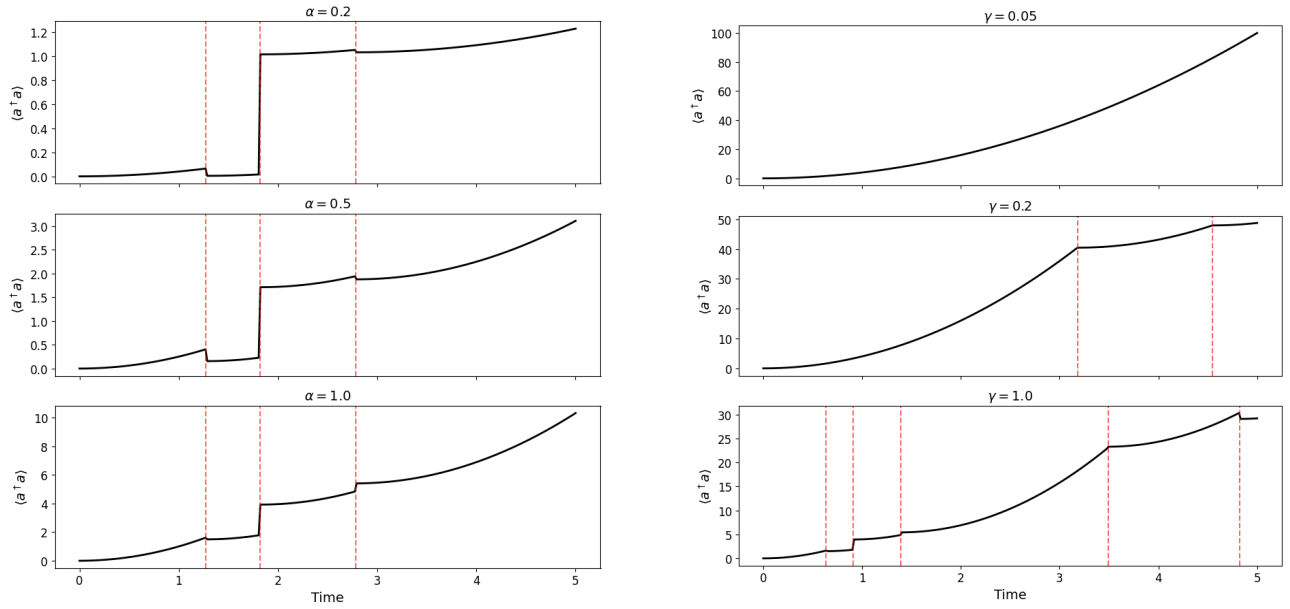

(a) Varying coherent driving α ($\gamma = 0.5$)

(b) Varying measurement rate γ ($\alpha = 2.0$)

Figure 5: Stochastic quantum trajectories of the cavity mean photon number $\langle \hat{n} \rangle_c$ under continuous parity monitoring. (a) Evolution under different coherent driving strengths α for a fixed measurement rate $\gamma = 0.5$. (b) Evolution for different measurement rates γ at a constant driving strength $\alpha = 2.0$.

The stochastic description becomes equivalent to the deterministic Lindblad description only after averaging over an ensemble of independent trajectories (Appendix A,B). If the state associated with trajectory i is

$$\rho_c^{(i)}(t) = |\psi_c^{(i)}(t)\rangle\langle\psi_c^{(i)}(t)|, \tag{3.19}$$

the unconditional density matrix is recovered as

$$\rho(t) = \mathbb{E}\left[\rho_c(t)\right] \simeq \frac{1}{N_{\text{traj}}} \sum_{i=1}^{N_{\text{traj}}} \rho_c^{(i)}(t), \tag{3.20}$$

where N_{traj} is the number of independent trajectories.

Consequently, for any observable $\hat{A}$,

$$\langle \hat{A} \rangle = \text{Tr}\left[\rho(t)\hat{A}\right] = \mathbb{E}\left[\langle \hat{A} \rangle_c\right]. \tag{3.21}$$

In particular, the photon-number dynamics obtained from the Monte Carlo simulation must converge to the solution of the Lindblad master equation when the number of trajectories is sufficiently large.

This correspondence is verified numerically in Fig. 6 by comparing the photon-number expectation value obtained from `mcsolve` with the deterministic solution obtained from `mesolve`. However, for a finite number of trajectories, the Monte Carlo result exhibits statistical fluctuations around the deterministic solution. As the number of trajectories is increased, these fluctuations become progressively smaller and the stochastic average converges to the Lindblad prediction.

The same correspondence can also be examined in phase space through the Wigner function. The numerical results in Fig. 7 show that the phase-space representation obtained from the ensemble of Monte Carlo trajectories agrees with the corresponding Lindblad evolution.

Besides, we can see that, for a single trajectory, the state is conditioned on one particular sequence of parity jumps , so different trajectories follow different random sequences, leading to slightly different final states. Nevertheless, when they are averaged, this spread produces a broader Wigner function and the elongated tail seen in Fig. 7, that reflects the statistical mixture of different conditional states rather than a broadening of a single coherent state.

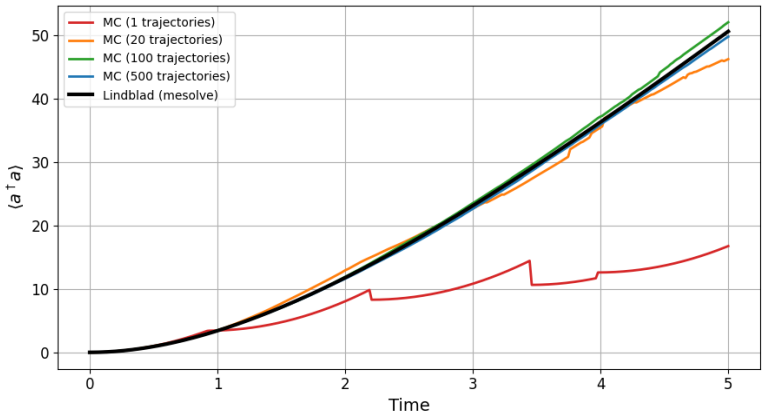

Figure 6: Convergence of the Monte Carlo wave-function ensemble towards the deterministic Lindblad master equation solution. The photon-number expectation value calculated from stochastic ensembles of increasing size ($N_{\text{traj}} = 1, 20, 100, 500$) is compared with the unconditional density matrix evolution.

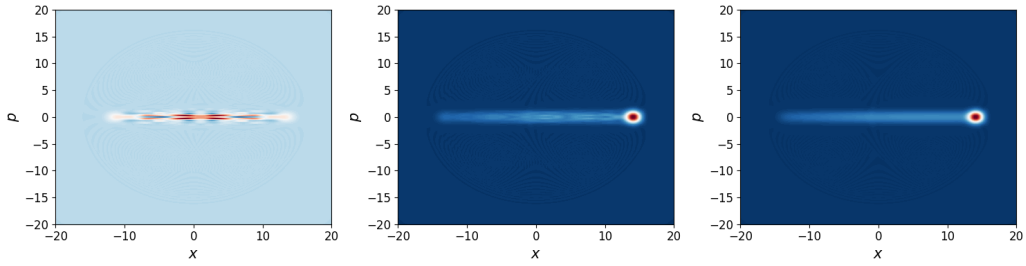

Figure 7: Wigner function of the cavity field under continuous parity monitoring. (Left) A single stochastic trajectory. (Center) The ensemble average over 500 independent trajectories. (Right) The unconditional state obtained via the Lindblad master equation.

4 Conclusion

This project has provided a first study of the dynamics of a cavity field under displacement and photon-number parity measurements, with particular emphasis on the transition from an ideal projective-measurement description to continuous monitoring in an open quantum system. Starting from the quantized description of a single cavity mode, the main concepts required to describe the system were introduced, including coherent states, phase-space representations, photon-number parity and the Wigner function.

The simulations of the projective measurement protocol showed how a parity measurement can transform an initially coherent state into an even or odd Schrödinger cat state. This provided a simple example of measurement-induced generation of non-classical states and showed how the overlap between the coherent components is directly related to the parity statistics and the appearance of interference structures in phase space. The Wigner representation was particularly useful for visualizing these effects and for connecting the displacement and parity operations with the evolution of the cavity state.

The study was then extended to continuous parity monitoring and open-system dynamics. The Lindblad master equation provides the deterministic description of the unconditional state, while the Monte Carlo wave-function method gives a stochastic description in terms of individual quantum trajectories. The numerical results confirmed that individual trajectories depend on the random sequence of measurement events, whereas their ensemble average converges to a Lindblad evolution. This correspondence was observed both in the photon-number dynamics and in the Wigner representation, providing a useful connection between the trajectory-level and ensemble descriptions of the same physical process.

Beyond the simulations presented here, the results of this study can serve as theoretical and numerical basis for a continuation of the project: the use of the cavity as a quantum reservoir [12, 13]. Quantum reservoir computing (QRC) exploits the natural dynamics of complex quantum systems to process temporal information, avoiding the need for fully programmable quantum circuits. In this framework, successive external inputs can be encoded through coherent displacements,

while the cavity dynamics, dissipation, and continuous parity monitoring provide the nonlinear and memory-dependent response required for reservoir computing. The present work therefore serves as a first characterization of the physical system and of the mechanisms that control its memory and decoherence, providing the necessary foundation for studying its computational capabilities as a quantum reservoir.

Acknowledgments

I would like to express my deepest gratitude to my supervisor, Luisa Toledo Tude, for her invaluable guidance, constant support, and encouragement throughout this project. Her mentorship have been fundamental to the completion of this work. I am also sincerely grateful to the friends I have made during the SURF fellowship, whose made this experience truly unforgettable. I would also like to thank the SURF coordinators for their dedication and support in organizing this fellowship. This work was supported by the SURF@IFISC fellowship.

Appendix

A Unconditional quantum state

The stochastic master equation describes the evolution of the *conditional* density matrix, $\rho_c(t)$, corresponding to a single realization of the continuous measurement process [11]. Since the sequence of quantum jumps is inherently random, each realization leads to a different quantum trajectory:

$$d\rho_c = dt\,\mathcal{L}\rho_c + \sum_k \Big(dN_k - dt\,\langle L_k^\dagger L_k\rangle_c\Big)\left(\frac{L_k\rho_c L_k^\dagger}{\langle L_k^\dagger L_k\rangle_c} - \rho_c\right) \tag{A.1}$$

where $\langle O\rangle_c = \mathrm{Tr}(O\rho_c)$, and the random variables dN_k describe the occurrence of quantum jumps in channel k during the infinitesimal time interval dt.

In case the individual measurement record is not accessible, or one is interested only in the average dynamics over many repetitions of the experiment, the relevant quantity is then the *unconditional* density matrix, defined as

$$\rho(t) = \mathbb{E}[\rho_c(t)]\,, \tag{A.2}$$

where $\mathbb{E}[\cdot]$ denotes the expectation value over all possible quantum trajectories. Equivalently, the unconditional density matrix corresponds to the deterministic solution of the Lindblad master equation,

$$\rho(t) = e^{\mathcal{L}t}\rho(0), \tag{A.3}$$

where $\mathcal{L}$ is the Liouvillian superoperator.

B Average jump probabilities

The probability that a quantum jump occurs in channel k during an infinitesimal time interval dt depends on the conditional state of the system and is given by

$$p_k^{(c)} = dt\,\mathrm{Tr}\Big(L_k^\dagger L_k\,\rho_c\Big)\,. \tag{B.1}$$

Since each quantum trajectory evolves according to a different sequence of measurement outcomes, the conditional density matrix ρ_c is generally different for every realization. The average jump probability obtained by averaging over all possible trajectories,

$$p_k = \mathbb{E}\Big[p_k^{(c)}\Big]\,. \tag{B.2}$$

Substituting the definition of the conditional probability:

$$p_k = \mathbb{E}\Big[dt\,\mathrm{Tr}\Big(L_k^\dagger L_k\,\rho_c\Big)\Big] \tag{B.3}$$

Since dt is a constant, it can be taken outside the expectation value, and the operator $L_k^\dagger L_k$ is fixed by the physical model and does not depend on the stochastic trajectory. Moreover, both the trace and the expectation value are linear operations. Therefore,

$$\mathbb{E}\Big[\mathrm{Tr}\Big(L_k^\dagger L_k\,\rho_c\Big)\Big] = \mathrm{Tr}\Big(L_k^\dagger L_k\,\mathbb{E}[\rho_c]\Big)\,. \tag{B.4}$$

Using the definition of the unconditional density matrix, $\mathbb{E}[\rho_c] = \rho$ one finally obtains

$$p_k = dt\,\mathrm{Tr}\Big(L_k^\dagger L_k\,\rho\Big)\,, \tag{B.5}$$

Overall, although every individual trajectory is characterized by a different sequence of quantum jumps, the average over infinitely many realizations defines a deterministic jump probability that depends only on the unconditional density matrix.

C Lindblad master equation for parity measurements

Starting from the stochastic equation,

$$\rho_c(t+dt) = \left(1 - \sum_k dN_k(t)\right)\frac{M_0\rho_c(t)M_0^\dagger}{1-\sum_k p_k^{(c)}(t)} + \sum_k dN_k(t)\frac{M_k\rho_c(t)M_k^\dagger}{p_k^{(c)}(t)} \tag{C.1}$$

one expects that averaging over all realizations of the stochastic variables $dN_k(t)$ should recover the unconditional quantum operation:

$$\rho(t+dt) = M_0\rho(t)M_0^\dagger + \sum_k M_k\rho(t)M_k^\dagger \tag{C.2}$$

However, this average cannot be performed by treating $dN_k(t)$ and $\rho_c(t)$ as statistically independent random variables. Indeed, the probability that a jump occurs is itself determined by the conditional state,

$$P(dN_k(t) = 1\,|\,\rho_c(t)) = p_k^{(c)}(t) \tag{C.3}$$

We make use of the law of total expectation,

$$\mathbb{E}[X] = \mathbb{E}_Y[\mathbb{E}(X|Y)] \tag{C.4}$$

Let $g(\rho_c)$ be an arbitrary function, then,

$$\mathbb{E}[dN_k\,g(\rho_c)] = \mathbb{E}[\mathbb{E}\left(dN_k\,g(\rho_c)\,|\,\rho_c\right)]\,. \tag{C.5}$$

Since the function $g(\rho_c)$ is completely determined once the conditional state is fixed, it behaves as a constant inside the conditional expectation,

$$\mathbb{E}[dN_k\,g(\rho_c)] = \mathbb{E}[g(\rho_c)\,\mathbb{E}\left(dN_k\,|\,\rho_c\right)]\,. \tag{C.6}$$

The stochastic variable dN_k is a Bernoulli random variable that takes the values

$$dN_k = \begin{cases} 1, & \text{if a jump occurs in channel } k,\\ 0, & \text{otherwise.}\end{cases}$$

For a Bernoulli variable, the conditional expectation is equal to the probability of obtaining the value one.

$$\mathbb{E}\left(dN_k\,|\,\rho_c\right) = p_k^{(c)} \tag{C.7}$$

Replacing this result into the previous expression immediately yields the identity

$$\boxed{\mathbb{E}[dN_k(t)\,g(\rho_c(t))] = \mathbb{E}\Big[p_k^{(c)}(t)\,g(\rho_c(t))\Big]\,,} \tag{C.8}$$

This identity has a clear physical interpretation: although the occurrence of a quantum jump is random for each individual trajectory, once the conditional state is specified the jump probability is completely determined. Consequently, averaging over all trajectories replaces the stochastic indicator dN_k by its conditional mean value $p_k^{(c)}$.

The identity can now be applied to the jump contribution appearing in the stochastic update equation by choosing $g(\rho_c) = \frac{M_k \rho_c M_k^\dagger}{p_k^{(c)}}$.

Since the Kraus operators are fixed they can be taken outside the expectation value and using the definition of the unconditional density matrix,

$$\mathbb{E}\left[dN_k \frac{M_k \rho_c M_k^\dagger}{p_k^{(c)}}\right] = \mathbb{E}\left[p_k^{(c)} \frac{M_k \rho_c M_k^\dagger}{p_k^{(c)}}\right] = \mathbb{E}\left[M_k \rho_c M_k^\dagger\right] = M_k\, \mathbb{E}[\rho_c]\, M_k^\dagger = M_k \rho M_k^\dagger. \tag{C.9}$$

Therefore, averaging the stochastic evolution over all trajectories gives

$$\rho(t+dt) = M_0 \rho M_0^\dagger + \sum_k M_k \rho M_k^\dagger \tag{C.10}$$

which coincides with the unconditional quantum operation introduced previously. Expanding the Kraus operators,

$$M_0 = I - iH_{\text{eff}}dt, \qquad M_k = \sqrt{dt}\, L_k \tag{C.11}$$

to first order in dt finally recovers the Lindblad master equation,

$$\boxed{\frac{d\rho}{dt} = -i[H,\rho] + \sum_k \left(L_k \rho L_k^\dagger - \frac{1}{2}\left\{L_k^\dagger L_k, \rho\right\}\right).} \tag{C.12}$$

In the present work, the environment continuously monitors the parity of the cavity field. Instead of considering dissipative processes associated with energy loss, the interaction with the environment is described through two measurement channels corresponding to the even- and odd-parity subspaces, defined in Ec.(3.13). Substituting these collapse operators into the general Lindblad master equation gives

$$\begin{aligned}\frac{d\rho}{dt} =& -i[H,\rho] + \gamma\left(P_{\text{even}}\rho P_{\text{even}} - \frac{1}{2}\{P_{\text{even}},\rho\}\right) \\ &+ \gamma\left(P_{\text{odd}}\rho P_{\text{odd}} - \frac{1}{2}\{P_{\text{odd}},\rho\}\right).\end{aligned} \tag{C.13}$$

Using the completeness relation

$$P_{\text{even}} + P_{\text{odd}} = I, \tag{C.14}$$

the anticommutator terms simplify according to

$$-\frac{\gamma}{2}\left(\{P_{\text{even}},\rho\} + \{P_{\text{odd}},\rho\}\right) = -\gamma\rho. \tag{C.15}$$

The master equation can therefore be written in the compact form

$$\boxed{\frac{d\rho}{dt} = -i[H,\rho] + \gamma\left(P_{\text{even}}\rho P_{\text{even}} + P_{\text{odd}}\rho P_{\text{odd}} - \rho\right).} \tag{C.16}$$

Introducing the definitions of the parity projectors, Ec.(2.26), the two projector terms become

$$\begin{aligned}P_{\text{even}}\rho P_{\text{even}} &= \frac{1}{4}(I+\Pi)\rho(I+\Pi) \\ &= \frac{1}{4}\left(\rho + \rho\Pi + \Pi\rho + \Pi\rho\Pi\right),\end{aligned} \tag{C.17}$$

and

$$\begin{aligned}P_{\text{odd}}\rho P_{\text{odd}} &= \frac{1}{4}(I-\Pi)\rho(I-\Pi) \\ &= \frac{1}{4}\left(\rho - \rho\Pi - \Pi\rho + \Pi\rho\Pi\right).\end{aligned} \tag{C.18}$$

Adding both contributions, the cross terms cancel exactly,

$$P_{\text{even}}\rho P_{\text{even}} + P_{\text{odd}}\rho P_{\text{odd}} = \frac{1}{2}\left(\rho + \Pi\rho\Pi\right). \tag{C.19}$$

Substituting this result into the master equation yields

$$\begin{aligned}\frac{d\rho}{dt} &= -i[H,\rho] + \gamma\left[\frac{1}{2}(\rho + \Pi\rho\Pi) - \rho\right] \\ &= -i[H,\rho] + \frac{\gamma}{2}\left(\Pi\rho\Pi - \rho\right).\end{aligned} \tag{C.20}$$

Therefore, the unconditional dynamics can be written in the compact form

$$\boxed{\frac{d\rho}{dt} = -i[H,\rho] + \frac{\gamma}{2}\left(\Pi\rho\Pi - \rho\right).} \tag{C.21}$$

D Derivation of the Wigner Function as a Displaced Parity Expectation Value

In this appendix, we provide a detailed mathematical demonstration of the equivalence between the Wigner function at an arbitrary point α in phase space and the expectation value of the displaced photon-number parity operator, as stated in Eq. (2.30), following [10].

First, we evaluate the Wigner function at the origin of the phase space, $x = 0$ and $p = 0$. Substituting these values into Eq. (2.22)

$$W(0,0) = \frac{2}{\pi}\int_{-\infty}^{\infty} dy\, \langle -y|\rho|y\rangle. \tag{D.1}$$

By taking the trace of the product of the density operator ρ and the parity operator $\hat{\Pi}$, we obtain:

$$\begin{aligned}\text{Tr}[\rho\hat{\Pi}] &= \int_{-\infty}^{\infty} dx\, \langle x|\rho\hat{\Pi}|x\rangle \\ &= \int_{-\infty}^{\infty} dx\, \langle x|\rho|-x\rangle.\end{aligned} \tag{D.2}$$

Applying the change of variable $y = -x$ in the integral above, we can write:

$$\text{Tr}[\rho\hat{\Pi}] = \int_{-\infty}^{\infty} dy\, \langle -y|\rho|y\rangle. \tag{D.3}$$

Comparing Eq. (D.3) with Eq. (D.1), we establish the identity for zero displacement:

$$W(0) = \frac{2}{\pi}\text{Tr}[\rho\hat{\Pi}]. \tag{D.4}$$

To generalize this result for any point $\alpha = X_0 + iP_0$ in phase space, we consider the unitary displacement operator defined in Eq. (2.17). The action of the displacement $D(-\alpha)$ on the original field produces the translated state

$$\rho' = \hat{D}(-\alpha)\rho\hat{D}(\alpha). \tag{D.5}$$

We can understand the translation of the Wigner function by analyzing how the displacement operator acts on the quadrature eigenbasis $|x\rangle$. Since $\hat{P}$ acts as the translation generator for $\hat{X}$ under our commutation relation $[\hat{X},\hat{P}] = i/2$, the displacement operator can be shown to act as $\hat{D}(\alpha)|x\rangle = e^{2iP_0x + iX_0P_0}|x + X_0\rangle$. Applying this relation to the matrix elements of the translated state ρ', we obtain:

$$\langle X - y|\rho'|X + y\rangle = e^{4iP_0y}\langle (X + X_0) - y|\rho|(X + X_0) + y\rangle. \tag{D.6}$$

Inserting this expression into the definition of the Wigner function in Eq. (2.22), the phase factors combine to shift the arguments of the original Wigner function:

$$W_{\rho'}(X,P) = W_\rho(X + X_0, P + P_0). \tag{D.7}$$

Evaluating this translated Wigner function at the origin ($X = 0, P = 0$) directly yields the original Wigner function evaluated at the point (X_0, P_0), which corresponds to the complex amplitude α:

$$W_{\rho'}(0,0) = W_\rho(X_0, P_0) \equiv W(\alpha). \tag{D.8}$$

Using the relation derived in Eq. (D.4) for zero displacement, we can express the value of the shifted Wigner function at the origin as

$$W_{\rho'}(0,0) = \frac{2}{\pi}\mathrm{Tr}[\rho'\hat{\Pi}]. \tag{D.9}$$

Substituting the definition of the translated state ρ' from Eq. (D.5) into Eq. (D.9), we find:

$$W(\alpha) = \frac{2}{\pi}\mathrm{Tr}\left[\hat{D}^\dagger(\alpha)\rho\hat{D}(\alpha)\hat{\Pi}\right]. \tag{D.10}$$

Finally, we can rearrange the operators inside the trace and applying $\langle\hat{O}\rangle = \mathrm{Tr}[\rho\hat{O}]$

$$W(\alpha) = \frac{2}{\pi}\mathrm{Tr}\left[\rho\hat{D}(\alpha)\hat{\Pi}\hat{D}^\dagger(\alpha)\right] = \frac{2}{\pi}\left\langle\hat{D}(\alpha)\hat{\Pi}\hat{D}^\dagger(\alpha)\right\rangle, \tag{D.11}$$

which concludes the derivation of Eq. (2.30).

References

[1] D. Browne, S. Bose, F. Mintert, and M. S. Kim, *From quantum optics to quantum technologies*, Progress in Quantum Electronics (2017).

[2] P. Meystre, *Quantum Optics: Taming the Quantum*, Graduate Texts in Physics, Springer Nature Switzerland AG (2021).

[3] C. Navarrete-Benlloch, *Introduction to Quantum Optics*, arXiv:2203.13206 [quant-ph] (2022).

[4] K. Hammerer, C. Genes, D. Vitali, P. Tombesi, G. Milburn, C. Simon, and D. Bouwmeester, *Nonclassical States of Light and Mechanics*, Cavity Optomechanics, edited by M. Aspelmeyer, T. J. Kippenberg, and F. Marquardt, Springer (2014), pp. 25–52.

[5] M. Brune, S. Haroche, J.-M. Raimond, L. Davidovich, and N. Zagury, *Manipulation of photons in a cavity by dispersive atom-field coupling: Quantum-nondemolition measurements and generation of "Schrödinger cat" states*, Phys. Rev. A 45, 5193 (1992).

[6] AllenMcC., *Wavefunctions of a quantum harmonic oscillator*, Wikimedia Commons (2010), CC BY-SA 3.0.

[7] A. C. Vutha, E. A. Bohr, A. Ransford, W. C. Campbell, and P. Hamilton, *Displacement operators: the classical face of their quantum phase*, European Journal of Physics 39, 025405 (2018).

[8] J. C. Garrison and R. Y. Chiao, *Quantum Optics*, Oxford University Press (2008).

[9] J. R. Johansson, P. D. Nation, and F. Nori, *QuTiP: An open-source Python framework for the dynamics of open quantum systems*, Computer Physics Communications 183, 1760–1772 (2012).

[10] S. Haroche, M. Brune, and J.-M. Raimond, *Measuring the photon number parity in a cavity: from light quantum jumps to the tomography of non-classical field states*, Journal of Modern Optics 54, 2101–2114 (2007).

[11] G. T. Landi, M. J. Kewming, M. T. Mitchison, and P. P. Potts, *Current Fluctuations in Open Quantum Systems: Bridging the Gap Between Quantum Continuous Measurements and Full Counting Statistics*, PRX Quantum 5, 020201 (2024).

[12] S. Das, G. L. Giorgi, and R. Zambrini, *Quantum reservoir computing in Jaynes-Cummings models: Nonlinear memory and time-series prediction*, Physical Review Research 8, 023148 (2026).

[13] K. Fujii and K. Nakajima, *Harnessing disordered ensemble quantum dynamics for machine learning*, arXiv:1602.08159v2 [quant-ph] (2016).

[14] C. S. Unnikrishnan, *Quantum non-demolition measurements: Concepts, theory and practice*, arXiv:1811.09613 [quant-ph] (2018).

Exploring Echo State Networks: Dynamical Regimes, Forecasting, Control and Biological Reservoirs

David Vicent García
Supervisor: Miguel C. Soriano

Instituto de Física Interdisciplinar y Sistemas Complejos, IFISC (CSIC-UIB)
Campus Universitat de les Illes Balears, E-07122 Palma de Mallorca, Spain

Abstract

Reservoir Computing exploits the intrinsic dynamics of a recurrent neural network by training only a simple readout layer. In this work, we study Echo State Networks (ESNs) from theoretical foundations to practical applications. We first analyze how the spectral radius of the reservoir's weight matrix governs its autonomous dynamical regimes. We then apply ESNs to the forecasting of the chaotic Lorenz system and the control of an inverted cart-pole system with limited observability. Finally, we evaluate the *C. elegans* connectome as a biological reservoir, investigating its short-term memory capacity and how hyperparameter tuning influences its performance.

1. Introduction

Recurrent Neural Networks (RNNs) are a type of neural architecture designed to process sequential data and model dynamical systems [1]. An RNN maintains an internal state $\boldsymbol{r}(k) \in \mathbb{R}^N$ that evolves recursively over discrete time steps k. The current internal state depends both on the immediate external input $\boldsymbol{u}(k) \in \mathbb{R}^{D_{\text{in}}}$ and on the state attained at the previous time step $\boldsymbol{r}(k-1)$:

$$\boldsymbol{r}(k) = f(\boldsymbol{r}(k-1), \boldsymbol{u}(k)), \tag{1}$$

where f is a nonlinear activation mapping.

Because the internal state $\boldsymbol{r}(k)$ encodes the history of the inputs, it holds memory of the sequence, allowing RNNs to process temporal information. In supervised training (used throughout this work), the network is driven by an input sequence (time series) and trained on a specific task so that its output matches a desired target sequence (teacher data). The goal is that when given a novel input sequence (not seen during training), the network successfully performs the learned task [2].

Let us consider a time-discrete RNN consisting of N neurons (units), where the connection strength from unit i to unit j is defined by a fixed, randomly assigned weight $W_{\text{ij}}^{\text{res}}$. We will call this network a *reservoir* [2]. The reservoir is driven by an input sequence $\boldsymbol{u}(k) \in \mathbb{R}^{D_{\text{in}}}$ and its internal state (i.e. activation values of all units) evolves according to:

$$\boldsymbol{r}(k) = f(\boldsymbol{W}^{\text{res}}\boldsymbol{r}(k-1) + \boldsymbol{W}^{\text{in}}\boldsymbol{u}(k)), \tag{2}$$

where $f(\cdot) = \tanh(\cdot)$ is applied component-wise, $\boldsymbol{W}^{\text{in}} \in \mathbb{R}^{N \times D_{\text{in}}}$ is the input weight matrix, and $\boldsymbol{W}^{\text{res}} \in \mathbb{R}^{N \times N}$ is the internal (recurrent) weight matrix. Both matrices are randomly initialized and then held fixed. Only a simple linear readout layer $\boldsymbol{W}^{\text{out}} \in \mathbb{R}^{D_{\text{out}} \times (N+1)}$ is trained to map the internal states to the desired task sequence. The reservoir dynamics are schematized in Figure 1.

The output is generated by applying the linear readout to the state vector augmented with a constant bias term $\hat{\boldsymbol{r}}(k) = \begin{pmatrix} \boldsymbol{r}(k) \\ 1 \end{pmatrix} \in \mathbb{R}^{N+1}$:

$$\boldsymbol{y}(k) = \boldsymbol{W}^{\text{out}} \hat{\boldsymbol{r}}(k). \tag{3}$$

The idea of restricting training to the output readout while relying on the reservoir's fixed internal dynamics is the framework known as **Reservoir Computing** (RC) [3].

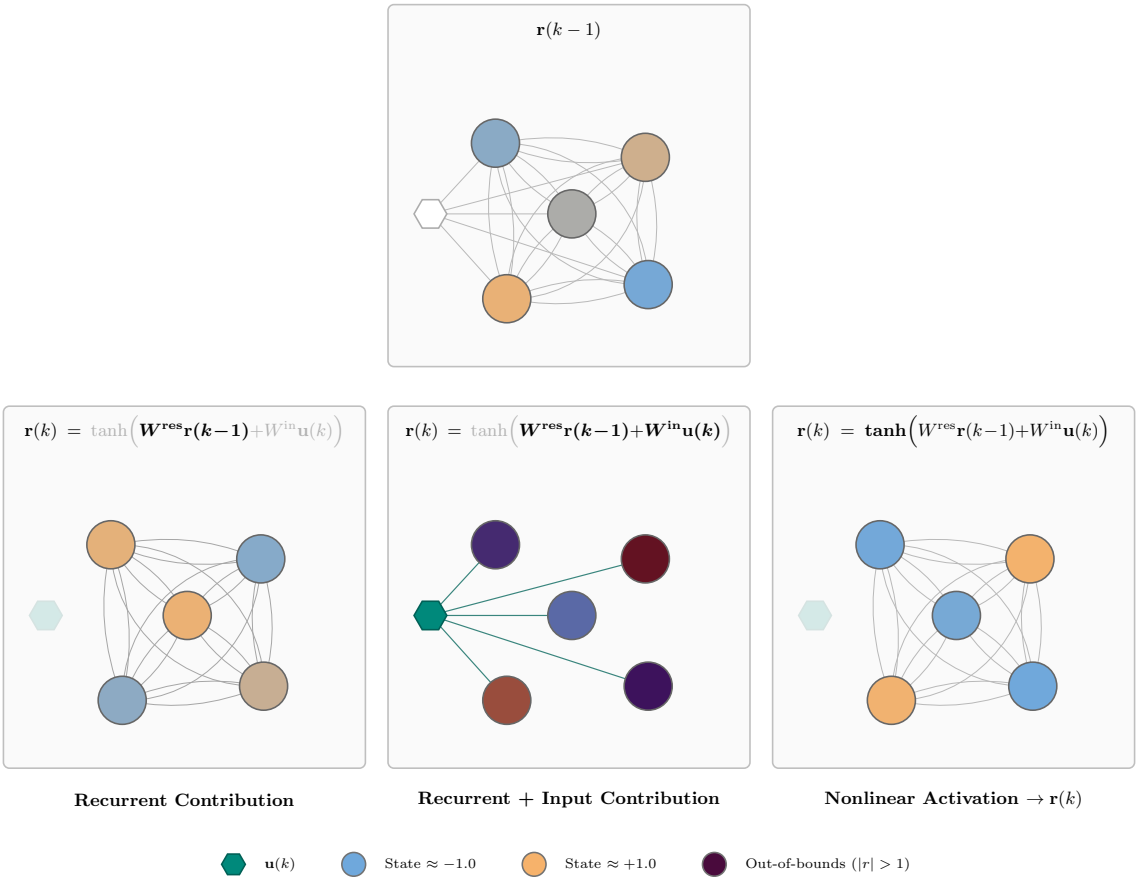

Figure 1: Schematic architecture of an RNN. At each time step, the internal state $\boldsymbol{r}(k)$ is updated by the past state $\boldsymbol{r}(k-1)$ and the current input $\boldsymbol{u}(k)$ (here $D_{\text{in}} = 1$, i.e., one input unit). The activation function $\tanh(\cdot)$ adds non-linearity to the operation and ensures activations are bounded between -1 and 1.

As highlighted by Nakajima [3], Reservoir Computing offers three advantages over traditional RNN frameworks:

1. **Computational Efficiency:** Because the reservoir's weights remain untrained, training simplifies to optimizing the readout layer. Classical approaches require training the entire network, which is computationally expensive.
2. **Multi-Task Capability:** The same fixed reservoir can support multiple tasks on the same input sequence simply by training separate, independent readout layers.
3. **Reservoir Flexibility & Physical RC:** Based on the given definition of RC, the reservoir does not actually need to be an RNN — it can be generalized to any dynamical system, giving rise to the field of Physical Reservoir Computing.

2. Theoretical Model

For RC to perform reproducible computations, the reservoir's internal state trajectory must be uniquely determined by the driving input sequence and the initial condition ($\boldsymbol{r}(0)$). If we were able to find a reservoir whose initial state did not ultimately affect its reproducibility, we would avoid the headache of inferring and fixing $\boldsymbol{r}(0)$ for each computation. We call this property the **Echo State Property** (ESP) [4].

Mathematically, a reservoir possesses the ESP with respect to a compact input domain $U \subset \mathbb{R}^{D_{\text{in}}}$ if there exists an *input echo function* $\boldsymbol{E}$ such that the present state depends uniquely on the left-infinite input history [4]:

$$\boldsymbol{r}(k) = \boldsymbol{E}(\cdots, \boldsymbol{u}(k-1), \boldsymbol{u}(k)) \tag{4}$$

A direct consequence of (4) is that if two identical reservoirs start from different initial states $\boldsymbol{r}(0)$ and $\boldsymbol{r}'(0)$ and are driven by the exact same input sequence, then the influence of the initial condition gradually fades and their internal states eventually converge[1]:

$$\lim_{k\to\infty} |\boldsymbol{r}(k) - \boldsymbol{r}'(k)| = 0 \tag{5}$$

Another closely related property is the **Fading Memory Property** (FMP), which ensures that the reservoir forgets distant past inputs as time progresses. More formally, for a network satisfying the ESP and operating under standard bounded conditions[2], the FMP guarantees that for every $\varepsilon > 0$, there exists a finite time window $h \in \mathbb{N}$ and a threshold $\delta > 0$ such that for any two infinite input histories $\boldsymbol{u}$ and $\boldsymbol{v}$ which are nearly identical over the recent window h,

$$|\boldsymbol{u}(k-j) - \boldsymbol{v}(k-j)| < \delta, \quad 0 \le j \le h, \tag{6}$$

the resulting reservoir states satisfy:

$$|\boldsymbol{r}_{\boldsymbol{u}}(k) - \boldsymbol{r}_{\boldsymbol{v}}(k)| \le \varepsilon \tag{7}$$

Together, the Echo State Property and the Fading Memory Property ensure that the state of the reservoir is uniquely determined by the most recent input history, making sequence processing possible.

2.1. Echo State Networks and Training Procedure

Let us go back to the network described by $\boldsymbol{W}^{\text{in}}$, $\boldsymbol{W}^{\text{res}}$, and $\boldsymbol{W}^{\text{out}}$. If such a network satisfies the ESP for any input from any compact set U, we call it an **Echo State Network** (ESN) [2].

It is an empirical finding that if the spectral radius[3] of $\boldsymbol{W}^{\text{res}}$ is strictly smaller than unity ($\rho < 1$), the network has the ESP, and it is thus an ESN, with freedom in the choice of $\boldsymbol{W}^{\text{in}}$ [2].

To construct and train an Echo State Network, we follow the procedure [2], [5]:

[1] Here $|\cdot|$ is the Euclidean distance in $\mathbb{R}^N$.

[2] Inputs are drawn from a compact (closed and bounded) set $U \subset \mathbb{R}^{D_{\text{in}}}$, and reservoir states are confined to a compact set $A \subset \mathbb{R}^N$ that is invariant under the update map, that is, once $\boldsymbol{r}(k) \in A$, every subsequent state also lies in A.

[3] The spectral radius is defined as $\rho(\boldsymbol{W}) = \max_i |\lambda_i|$, representing the largest eigenvalue magnitude of the recurrent weight matrix.

1. Generate a random internal connectivity matrix $\boldsymbol{W}_0 \in \mathbb{R}^{N\times N}$ with N neurons and connection sparsity[4] s, where the non-zero entries are typically drawn from a uniform distribution $W_{0,ij} \in \mathcal{U}(-1,1)$ or a standard normal distribution $\mathcal{N}(0,1)$.

2. Normalize $\boldsymbol{W}_0$ by its largest absolute eigenvalue and scale it to enforce the desired spectral radius ρ:

$$\boldsymbol{W}^{\text{res}} = \rho \frac{\boldsymbol{W}_0}{|\lambda_{\max}(\boldsymbol{W}_0)|} \tag{8}$$

3. Define the training input sequence $\boldsymbol{u}(k) \in \mathbb{R}^{D_{\text{in}}}$ and target sequence $\boldsymbol{d}(k) \in \mathbb{R}^{D_{\text{out}}}$.

4. Generate a random input matrix $\boldsymbol{W}^{\text{in}} \in \mathbb{R}^{N\times D_{\text{in}}}$ with entries chosen from a uniform distribution on $[-\zeta, \zeta]$, where ζ is the input scaling factor.

5. Drive the reservoir with the training sequence $\boldsymbol{u}(k)$ for $k = 1, ..., T$ according to (2), starting from $\boldsymbol{r}(0) = \boldsymbol{0}$. To eliminate transient effects caused by the arbitrary zero initial condition, the first T_w states are discarded (washout period). The remaining $M = T - T_w$ augmented state vectors are collected into the extended state matrix[5]:

$$\boldsymbol{R}_w = \begin{pmatrix} \boldsymbol{r}(T_w+1) & \boldsymbol{r}(T_w+2) & \cdots & \boldsymbol{r}(T) \\ 1 & 1 & \cdots & 1 \end{pmatrix} \in \mathbb{R}^{(N+1)\times M} \tag{9}$$

   We collect the target as well into $\boldsymbol{D}_w = (\boldsymbol{d}(T_w+1) \cdots \boldsymbol{d}(T)) \in \mathbb{R}^{D_{\text{out}}\times M}$.

6. If we applied equation (3) at each training time step k to get $\boldsymbol{y}_{\text{train}}(k)$, we would wish that $\boldsymbol{y}_{\text{train}}(k) \approx \boldsymbol{d}(k)$. For that, we optimize $\boldsymbol{W}^{\text{out}}$ so that it minimizes the Mean Squared Error (MSE):

$$\text{MSE}_{\text{train}} = \frac{1}{M} \sum_{k=T_w+1}^{T} \|\boldsymbol{d}(k) - \boldsymbol{y}_{\text{train}}(k)\|^2. \tag{10}$$

   The optimal readout weights can be obtained via ridge regression to penalize large weights ($\beta > 0$):

$$\boldsymbol{W}^{\text{out}} = \boldsymbol{D}_w \boldsymbol{R}_w^\top (\boldsymbol{R}_w \boldsymbol{R}_w^\top + \beta \boldsymbol{I}_{N+1})^{-1}. \tag{11}$$

7. Finally, starting again from $\boldsymbol{r}(0) = \boldsymbol{0}$, we apply the trained readout to the novel test sequence $\boldsymbol{u}_{\text{test}}(k)$ for $k = 1, ..., T_{\text{test}}$ to obtain $\boldsymbol{y}_{\text{test}}(k)$. As before, we discard the first T_w states.

   To assess the goodness of fit, we use (10) with $\boldsymbol{d}_{\text{test}}(k)$ and $\boldsymbol{y}_{\text{test}}(k)$ to get MSE_{test}. We can also use the coefficient of determination R^2 to get a scale-independent value, where $R^2 = 1$ indicates perfect fit:

$$R^2 = 1 - \frac{\text{MSE}_{\text{test}}}{\text{Var}(\boldsymbol{d}_{\text{test}})}. \tag{12}$$

Note. We call the reservoir size (N), the spectral radius (ρ), the input scaling factor (ζ), the sparsity (s), and the regularization parameter (β) the **hyperparameters** of the network.

[4] The connection sparsity s represents the fraction of zero-valued elements in $\boldsymbol{W}_0$, so that $(1-s)$ is the density of active connections.

[5] Appending a constant row of ones to the state vector allows the linear readout $\boldsymbol{W}^{\text{out}}$ to optimize an offset term (bias) for the output.

2.2. Spectral Radius and Autonomous Reservoir Dynamics

In this section, we analyze the influence of the spectral radius on the autonomous dynamics of the reservoir, that is, without external drive ($\boldsymbol{u}(k) = \mathbf{0}$). Under these conditions, the state update equation (2) simplifies to:

$$\boldsymbol{r}(k) = \tanh(\boldsymbol{W}^{\text{res}}\boldsymbol{r}(k-1)), \tag{13}$$

where the internal matrix $\boldsymbol{W}^{\text{res}}$ is parameterized directly by its spectral radius ρ. We simulate an autonomous network of $N = 100$ units ($s = 0.8$, $W_{0,ij} \in \mathcal{N}(0,1)$), initialized from a uniform random initial state $\boldsymbol{r}(0) \in [-1,1]^N$ across four different spectral radii: $\rho \in \{0.7, 0.99, 1.2, 2.2\}$.

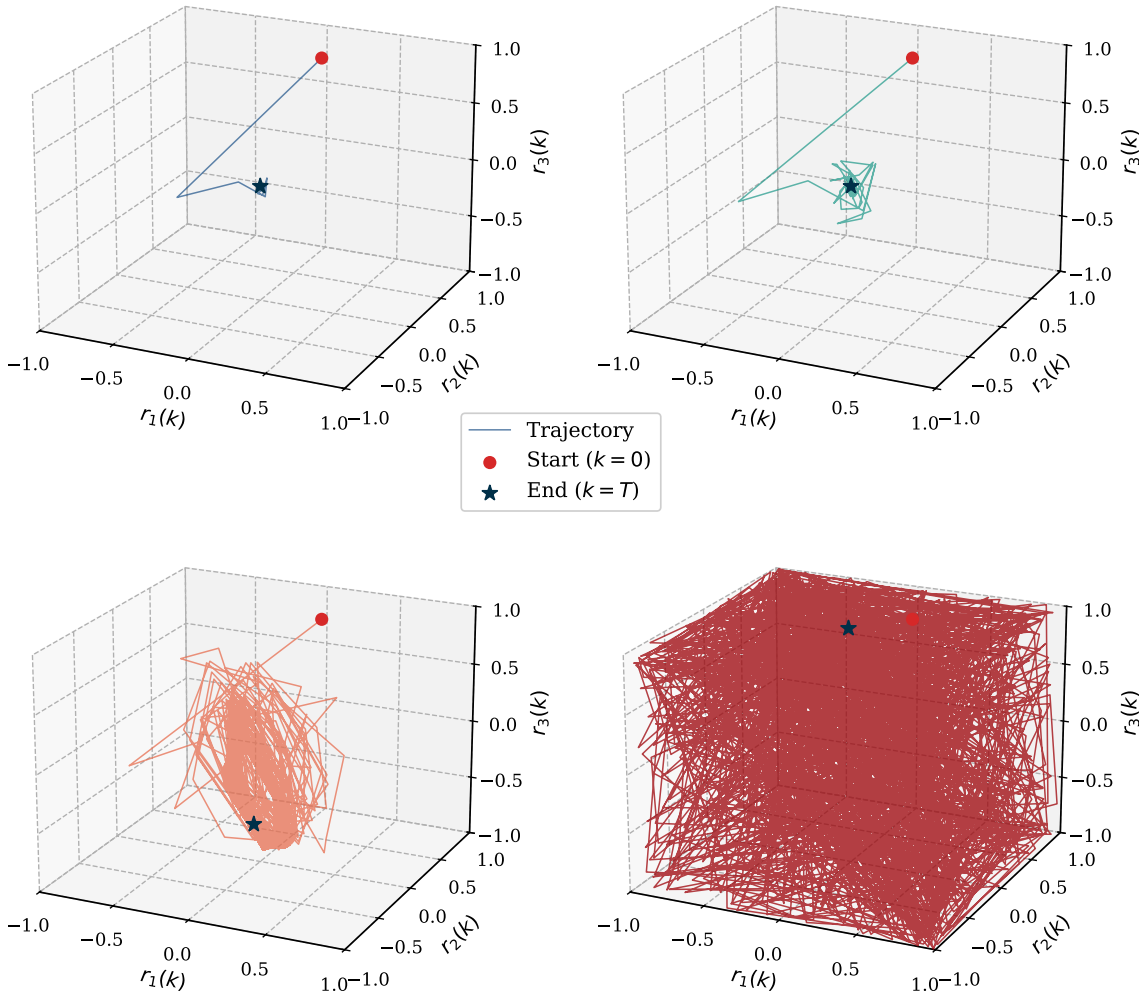

Figure 2: Three-dimensional phase portraits of three representative reservoir neurons (r_1, r_2, r_3) in autonomous mode (1500 time steps) across four characteristic spectral radius regimes: top-left ($\rho = 0.7$), top-right ($\rho = 0.99$), bottom-left ($\rho = 1.2$), and bottom-right ($\rho = 2.2$). Red circles mark the initial state ($k = 0$) and dark stars denote the final state ($k = 1500$).

As illustrated in the phase portraits (Figure 2), single-neuron time series (Figure 3), and spatiotemporal activation heatmaps (Figure 4), varying ρ drives the network through distinct dynamical regimes:

1. **Contracting Regime ($\rho = 0.7 < 1$):** The origin $\boldsymbol{r}^* = \mathbf{0}$ is an asymptotically stable fixed point. All trajectories rapidly decay to zero, demonstrating a "strong" ESP.
2. **Critical Regime ($\rho = 0.99 \approx 1$):** As the spectral radius approaches unity, the decay toward zero slows down drastically. The reservoir retains memory of its initial state for a long time, operating at the edge of stability.
3. **Periodic Regime ($\rho = 1.2 > 1$):** The zero fixed point loses stability. The autonomous dynamics settle into periodic cycles, visible as regular oscillations in Figure 3 and alternating spatiotemporal bands in Figure 4.
4. **Chaotic Regime ($\rho = 2.2 \gg 1$):** As ρ substantially surpasses unity, the periodic regime destabilizes into deterministic chaos.

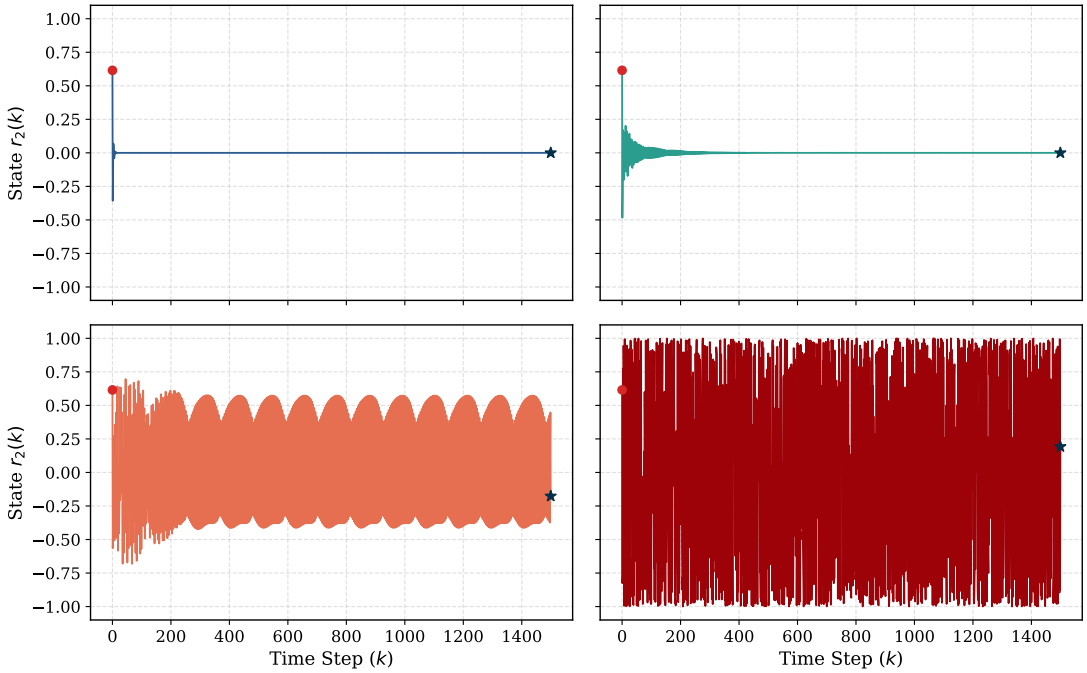

Figure 3: Temporal activation profiles of a monitored reservoir neuron (r_2) over 1500 discrete time steps across the four spectral radius regimes: top-left ($\rho = 0.7$), top-right ($\rho = 0.99$), bottom-left ($\rho = 1.2$), and bottom-right ($\rho = 2.2$).

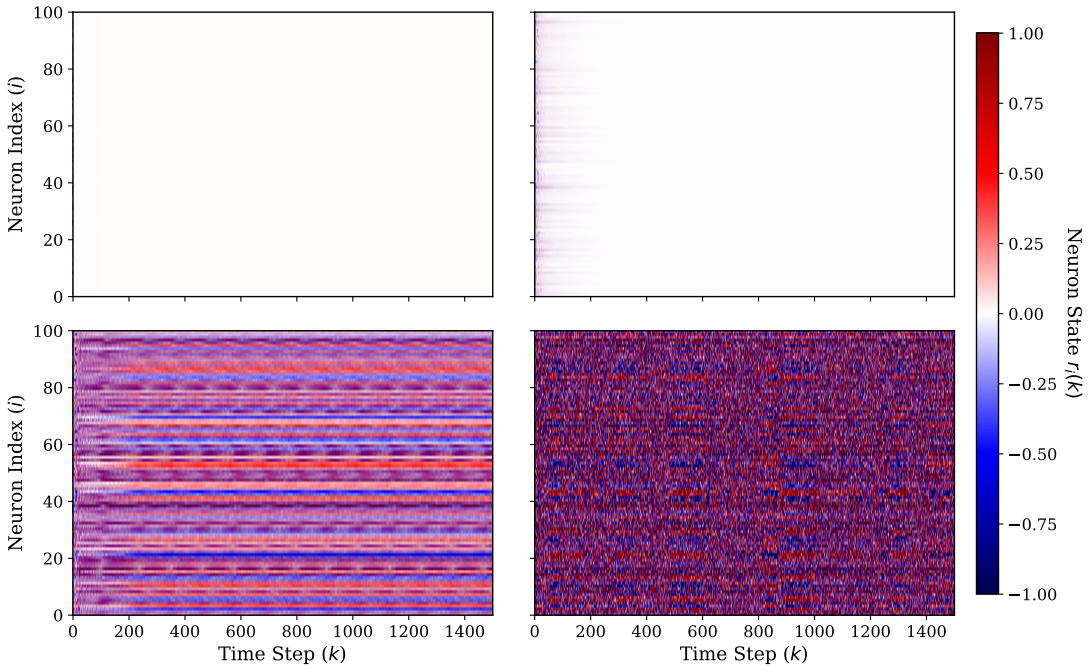

Figure 4: Spatiotemporal state heatmaps across all $N = 100$ neurons for $k \in [0, 1500]$: top-left ($\rho = 0.7$), top-right ($\rho = 0.99$), bottom-left ($\rho = 1.2$), and bottom-right ($\rho = 2.2$). White corresponds to zero activation ($r_i = 0$).

To map the continuous transition between these dynamical phases, we construct a bifurcation diagram (Figure 5). For each spectral radius $\rho \in [0.5, 2.5]$, we simulate the autonomous network for 1500 steps, discard the initial transient ($T_w = 1000$ steps), and plot all the asymptotic states that unit r_2 visits.

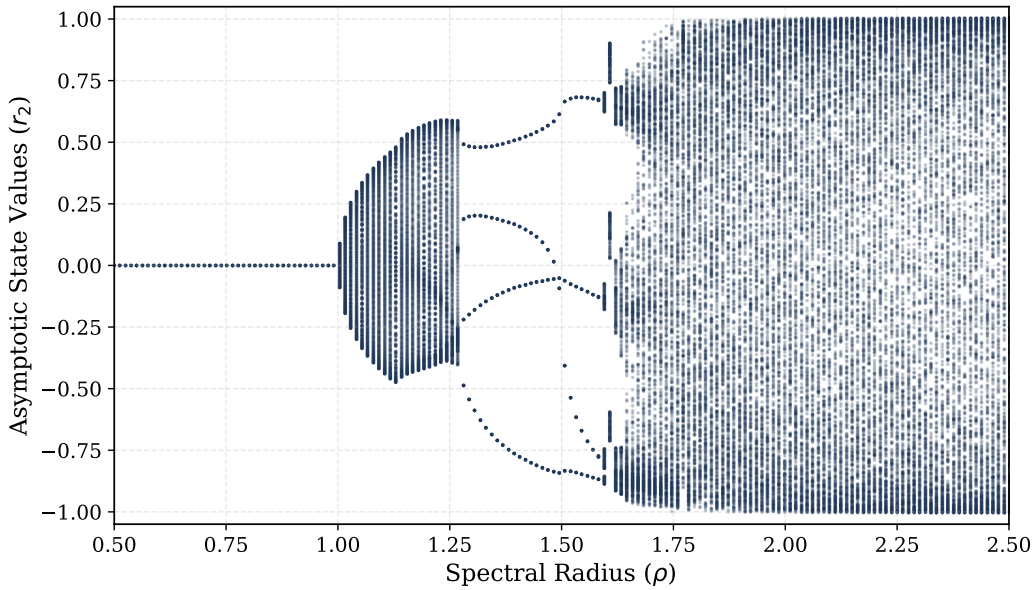

Figure 5: Bifurcation diagram of reservoir neuron r_2 as a function of the spectral radius $\rho \in [0.5, 2.5]$.

As shown in Figure 5, for $\rho < 1.0$ the system's asymptotic state is zero. Right around $\rho \approx 1.0$, the zero fixed point becomes unstable and oscillations emerge (as seen in Figure 3, bottom-left). As ρ increases past $\rho \approx 1.7$, the network transitions into deterministic chaos.

3. Applications

3.1. Closed-Loop Forecasting of Chaotic Systems

In this section, we work with a closed-loop setting, where the output of the network is fed back into the reservoir at the following time step [5]. This configuration allows us to study the time-series forecasting of a chaotic system, specifically the Lorenz system.

We use a teacher-forcing protocol. During training, the reservoir is driven at every step by the true external signal $\boldsymbol{u}(k)$, following (2), and the readout is optimized to predict the one-step-ahead target $\boldsymbol{d}(k) = \boldsymbol{u}(k+1)$. For the testing phase, the external drive is removed, and the network is switched to closed-loop autonomous operation. The predicted output $\boldsymbol{v}(k) = \boldsymbol{W}^{\text{out}}\hat{\boldsymbol{r}}(k)$ is recursively fed back as the input for the next time step[6]:

$$\begin{aligned} \boldsymbol{v}(k) &= \boldsymbol{W}^{\text{out}}\hat{\boldsymbol{r}}(k), \\ \boldsymbol{r}(k+1) &= \tanh(\boldsymbol{W}^{\text{res}}\boldsymbol{r}(k) + \boldsymbol{W}^{\text{in}}\boldsymbol{v}(k)). \end{aligned} \tag{14}$$

Because small prediction errors are recursively re-injected into the reservoir, we expect that the point-by-point tracking accuracy will eventually drop due to error accumulation.

3.1.1. Lorenz System Forecasting

We evaluate autonomous prediction on the classical three-dimensional Lorenz (1963) system [6]:

$$\begin{aligned} \dot{x} &= \sigma(y - x), \\ \dot{y} &= x(\rho_{\text{L}} - z) - y, \\ \dot{z} &= xy - \beta_{\text{L}} z, \end{aligned} \tag{15}$$

with standard chaotic parameters $\sigma = 10$, $\rho_{\text{L}} = 28$, and $\beta_{\text{L}} = 8/3$, starting from the initial condition $(x_0, y_0, z_0) = (1, 1, 1)$[7].

We employ a reservoir of $N = 1000$ neurons ($W_{0,ij} \in \mathcal{U}(-1, 1)$), with hyperparameters $s = 0.90$, $\rho = 0.99$, $\zeta = 0.50$, $\beta = 10^{-2}$, and an initial washout of $T_w = 100$ steps. Driven by the full state $\boldsymbol{u}(k) = (x(k), y(k), z(k))^\top$, the readout learns to predict $\boldsymbol{d}(k) = (x(k+1), y(k+1), z(k+1))^\top$.

As shown in Figure 6, the training fit matches the true trajectory across all three coordinates with high precision: $\text{MSE}_x = 3.24 \times 10^{-4}$, $\text{MSE}_y = 2.98 \times 10^{-3}$, and $\text{MSE}_z = 2.05 \times 10^{-3}$.

For testing, the reservoir first undergoes a brief warm-up phase where it is still driven by the true external signal[8]. At $t_{\text{switch}} = 637$, the loop is closed and the ESN evolves autonomously according to (14) (Figure 7).

[6] We denote the autonomous feedback signal by $\boldsymbol{v}(k)$ to avoid notational conflict with the spatial coordinates (x, y, z) of the chaotic system.

[7] Trajectories are generated using forward Euler integration ($\Delta t_{\text{sim}} = 0.02$, $T = 790$) and subsampled by a factor of 5 to an effective step $\Delta t_{\text{eff}} = 0.1$ (7,900 samples total). The dataset is split into 80% training ($n_{\text{train}} = 6,320$ steps, $t \in [0, 632]$) and 20% testing ($n_{\text{test}} = 1,580$ steps, $t \in [632, 790]$).

[8] The warm-up spans 50 steps ($t \in [632, 637]$).

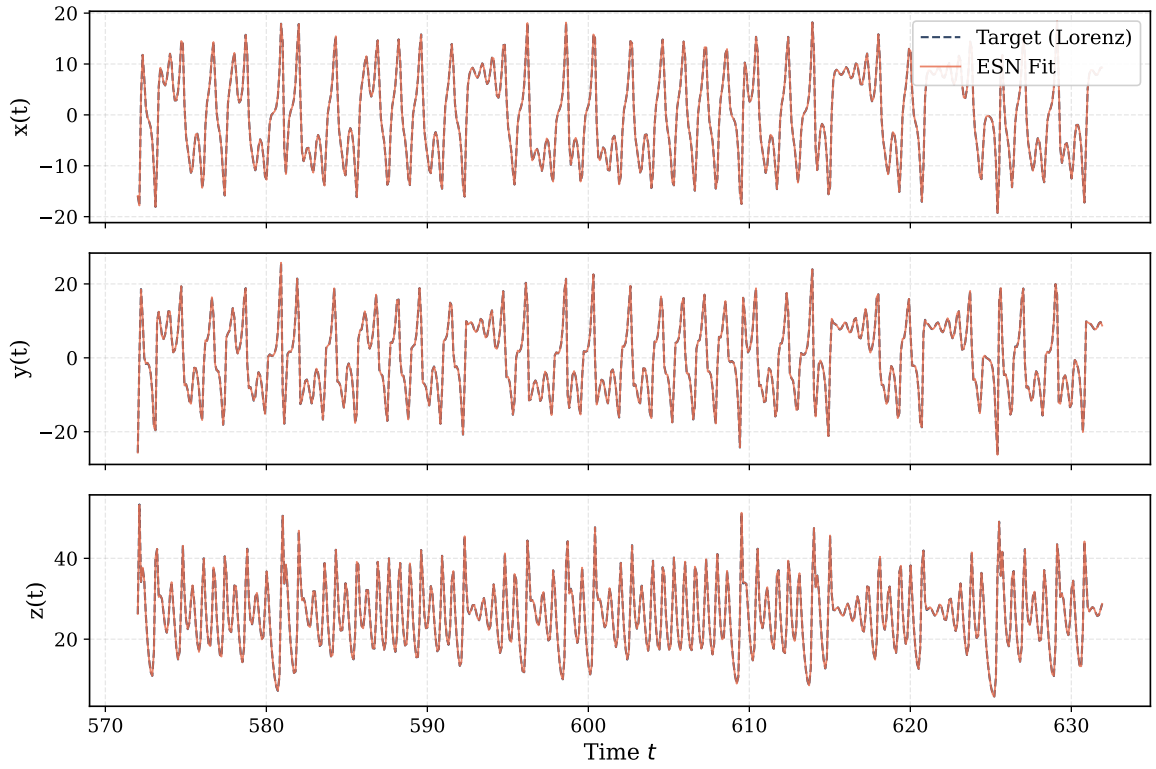

Figure 6: Lorenz system training phase fit over a representative post-washout window (teacher-driven mode, not autonomous operation). Ground-truth Lorenz coordinates versus one-step ESN training fit for $x(t)$, $y(t)$, and $z(t)$, achieving an overall training error of $\mathrm{MSE} = 1.78 \times 10^{-3}$.

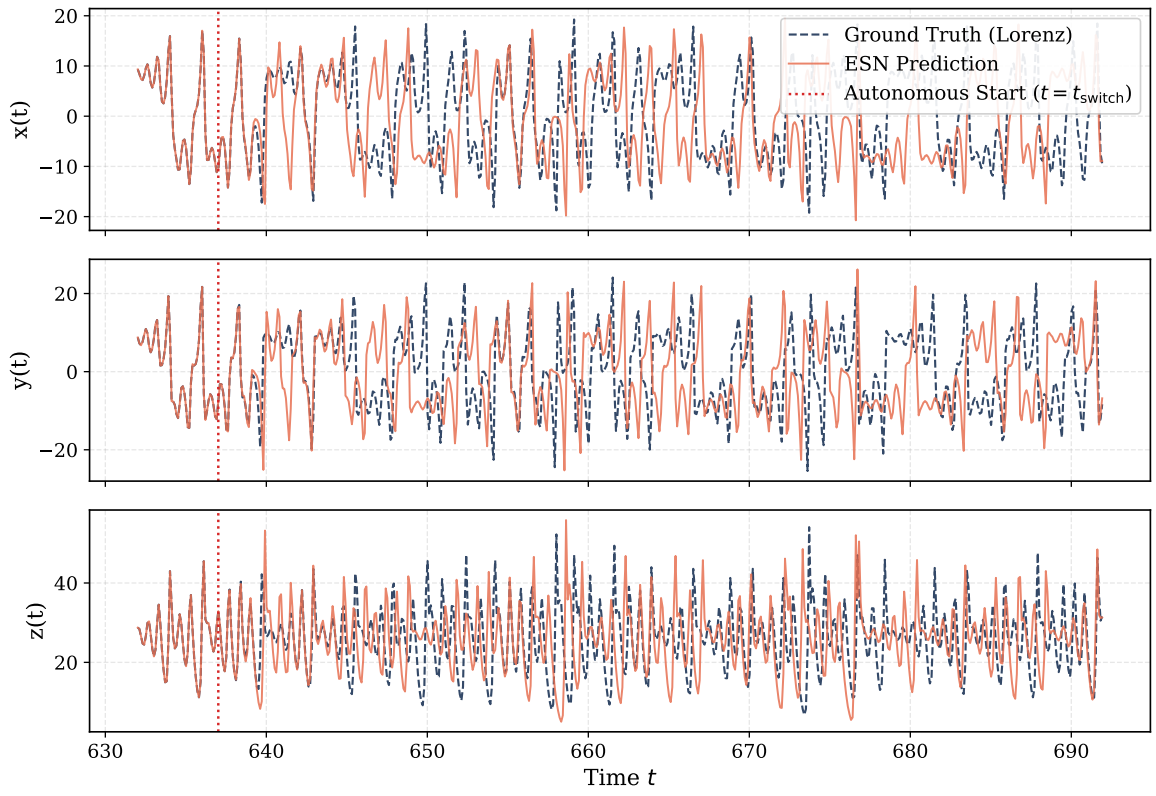

Figure 7: Lorenz system autonomous closed-loop test ($t \in [632, 692]$). The vertical dotted red line marks the transition at $t_{\mathrm{switch}} = 637$ from driven warm-up to autonomous prediction.

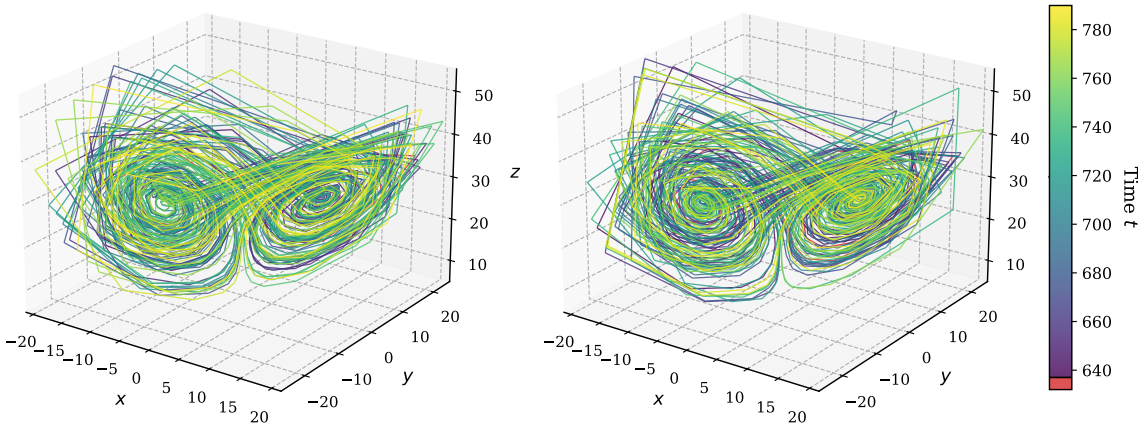

Figure 8: Three-dimensional phase space reconstruction of the Lorenz system ($t \in [632, 790]$). Left: Ground-truth Lorenz attractor. Right: Autonomous ESN reconstruction. The initial driven warm-up segment ($t \leq 637$) is highlighted in red on both trajectories and the colorbar, while the autonomous trajectory is colored continuously by time t.

As shown in Figure 7, the autonomous ESN achieves good short-term tracking over the first $3.0 - 8.0$ time units, but quickly diverges due to error accumulation. However, Figure 8 shows that the autonomous network faithfully reconstructs the full two-lobed butterfly geometry and spatial boundaries of the Lorenz attractor. Thus, while point-by-point tracking ("weather") degrades quickly over time, the long-term attractor geometry ("climate") is preserved by the autonomous ESN.

3.2. Inverted Pendulum Control

We consider balancing an inverted pendulum pivoted on a moving cart (cart mass $M = 1.0$ kg, rod length $l = 0.5$ m, tip mass $m = 0.1$ kg) along a horizontal track by applying a control force F (Figure 9).

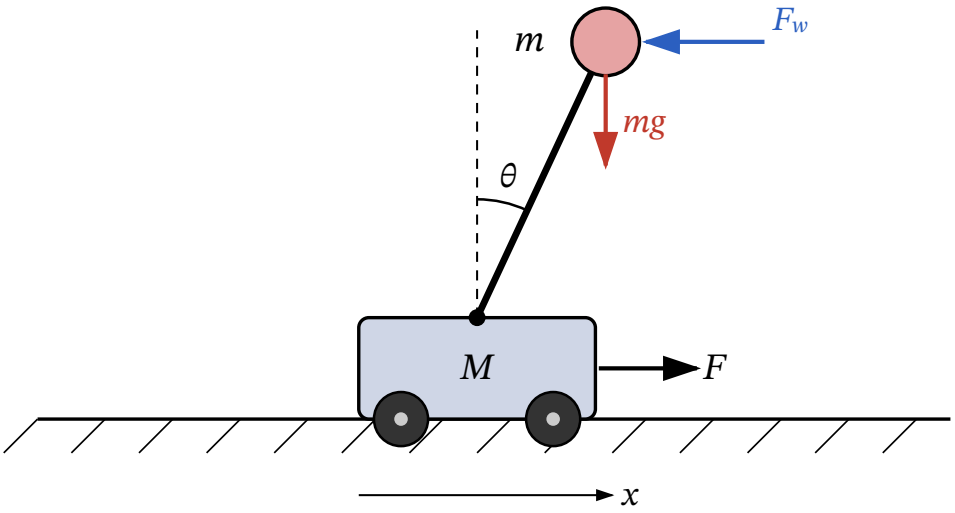

Figure 9: Cart-pole schematic: cart mass M, pole length l, tip mass m, tilt angle θ, horizontal control force F, wind disturbance $F_w(x,t)$, and gravitational acceleration $g = 9.81$ m/s^2.

Under the point-mass approximation, the equations of motion are:

$$\ddot{x} = \frac{F + F_w(x,t) + ml\sin(\theta)\,\dot{\theta}^2 - [F_w(x,t)\cos(\theta) + mg\sin(\theta)]\cos(\theta)}{M + m\sin^2(\theta)} \tag{16}$$

$$\ddot{\theta} = \frac{(M+m)[F_w(x,t)\cos(\theta) + mg\sin(\theta)] - m\cos(\theta)\left[F + F_w(x,t) + ml\sin(\theta)\,\dot{\theta}^2\right]}{ml(M + m\sin^2(\theta))} \tag{17}$$

The cart is subjected to a spatial wind field with random high-frequency turbulence $\nu(t) \in [-0.03, +0.03]$ N:

$$F_w(x,t) = -F_0 \tanh\left(\frac{x}{L}\right) + \nu(t), \tag{18}$$

with $F_0 = 0.8$ N and $L = 2.0$ m.

A simple linear controller is chosen to stabilize the cart-pole system:

$$F(k) = k_x x(k) + k_{\dot{x}}\dot{x}(k) + k_\theta \theta(k) + k_{\dot{\theta}}\dot{\theta}(k), \tag{19}$$

with gains $k_x = 4.0$ N/m, $k_{\dot{x}} = 4.0$ N $\cdot$ s/m, $k_\theta = 55.0$ N/rad, and $k_{\dot{\theta}} = 9.0$ N $\cdot$ s/rad.

3.2.1. Partial Observability Problem & Reservoir Training

While the teacher controller (19) requires the complete four-dimensional state $\boldsymbol{q} = \left(x, \dot{x}, \theta, \dot{\theta}\right)^\top$, our goal is to train an ESN using **only** the scalar tilt angle $u(k) = \theta(k)$ without direct sensor access to cart position or velocities.

Training data is collected over a $T_{\text{train}} = 200$ s simulation ($\Delta t = 0.01$ s) excited by an external force $F_{\text{exc}}(t)$ applied directly to the cart. This excitation force combines a two-tone sinusoidal signal (0.015 Hz and $0.015\sqrt{2}$ Hz), random impulsive kicks (5–25 N), and quiet settling periods (Figure 11, top). A trial terminates if $|x| > x_{\text{limit}} = 6.0$ m or $|\theta| > \theta_{\text{limit}} = \frac{\pi}{2}$.

We employ a reservoir of $N = 500$ neurons ($W_{0,ij} \in \mathcal{U}(-1, 1)$), with hyperparameters $s = 0.80$, $\rho = 0.95$, $\zeta = 1.0$, $\beta = 10^{-3}$, and an initial washout of $T_w = 2.0$ s. The state updates via:

$$\boldsymbol{r}(k+1) = (1-\alpha)\boldsymbol{r}(k) + \alpha \tanh(\boldsymbol{W}^{\text{res}}\boldsymbol{r}(k) + \boldsymbol{W}^{\text{in}}\theta(k+1)), \tag{20}$$

where $\alpha = 0.18$ is called the *leaky rate* [5]. Readout weights $\boldsymbol{W}^{\text{out}}$ are optimized to reproduce the teacher force $d(k) = F(k)$.

As shown in Figure 10 and Figure 11, the training protocol covers a large part of the state space while the reservoir accurately learns the control dynamics.

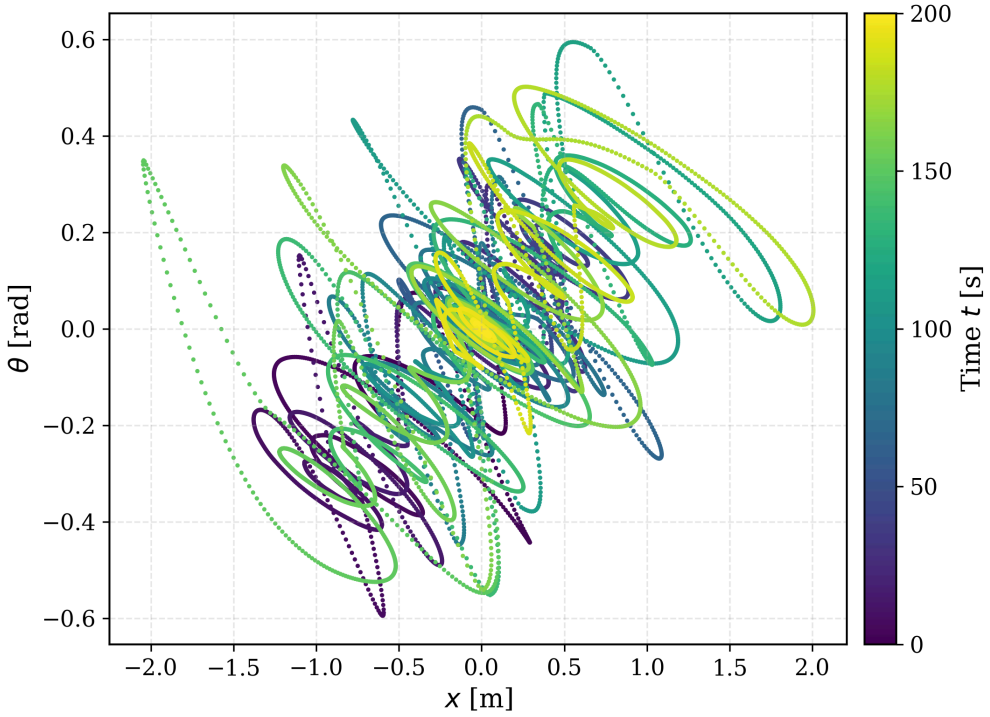

Figure 10: Phase space (x, θ) explored during the 200 s cart-pole training run, with the colorbar indicating simulation time t.

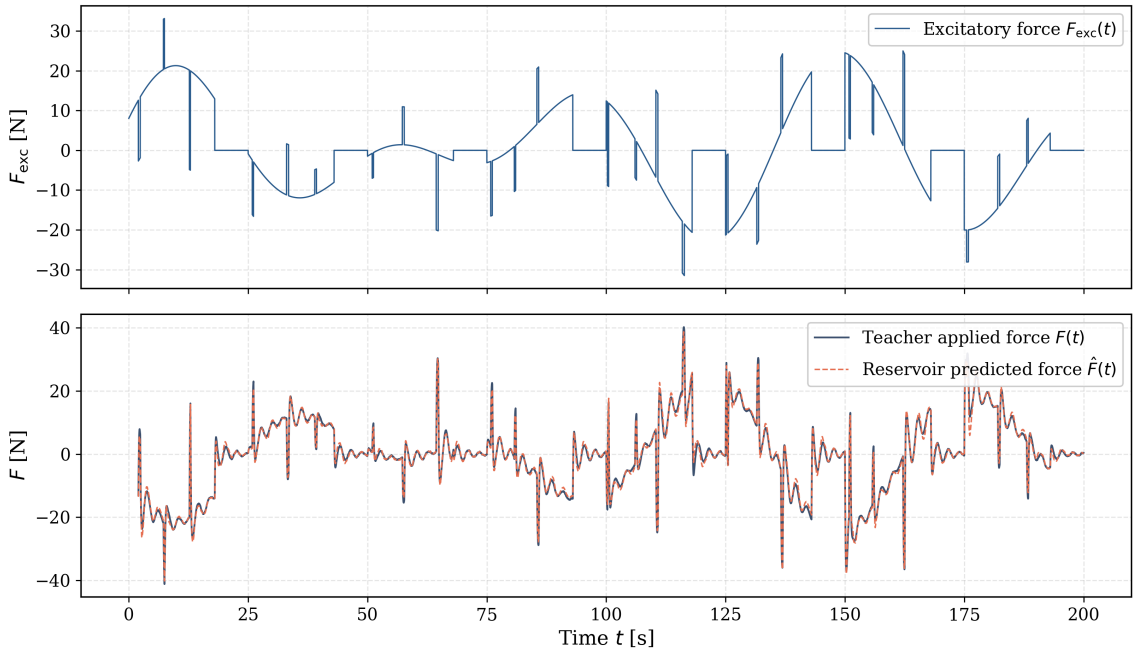

Figure 11: Cart-pole training forces: (top) composite excitation force $F_{\text{exc}}(t)$ applied to the cart during training; (bottom) applied teacher force $F(t)$ versus reservoir-predicted force $\hat{F}(t)$ after the initial 2.0 s washout period, achieving a low error of $\text{MSE}_{\text{train}} = 1.0471$ ($R^2 = 0.9915$).

3.2.2. Closed-Loop Autonomous Testing

Autonomous performance is tested over a 120 s closed-loop run under novel wind turbulence ($\nu_{\max} = 0.03$ N). Following a 5.0 s teacher warm-up, control switches entirely to the autonomous reservoir readout $F(k) = \boldsymbol{W}^{\text{out}}\hat{\boldsymbol{r}}(k)$. Four disturbance kicks are injected: +25 N ($t = 20.00$ – 20.40 s), −18 N ($t = 45.00$ – 45.35 s), +12 N ($t = 70.00$ – 70.30 s), and −28 N ($t = 95.00$ – 95.40 s).

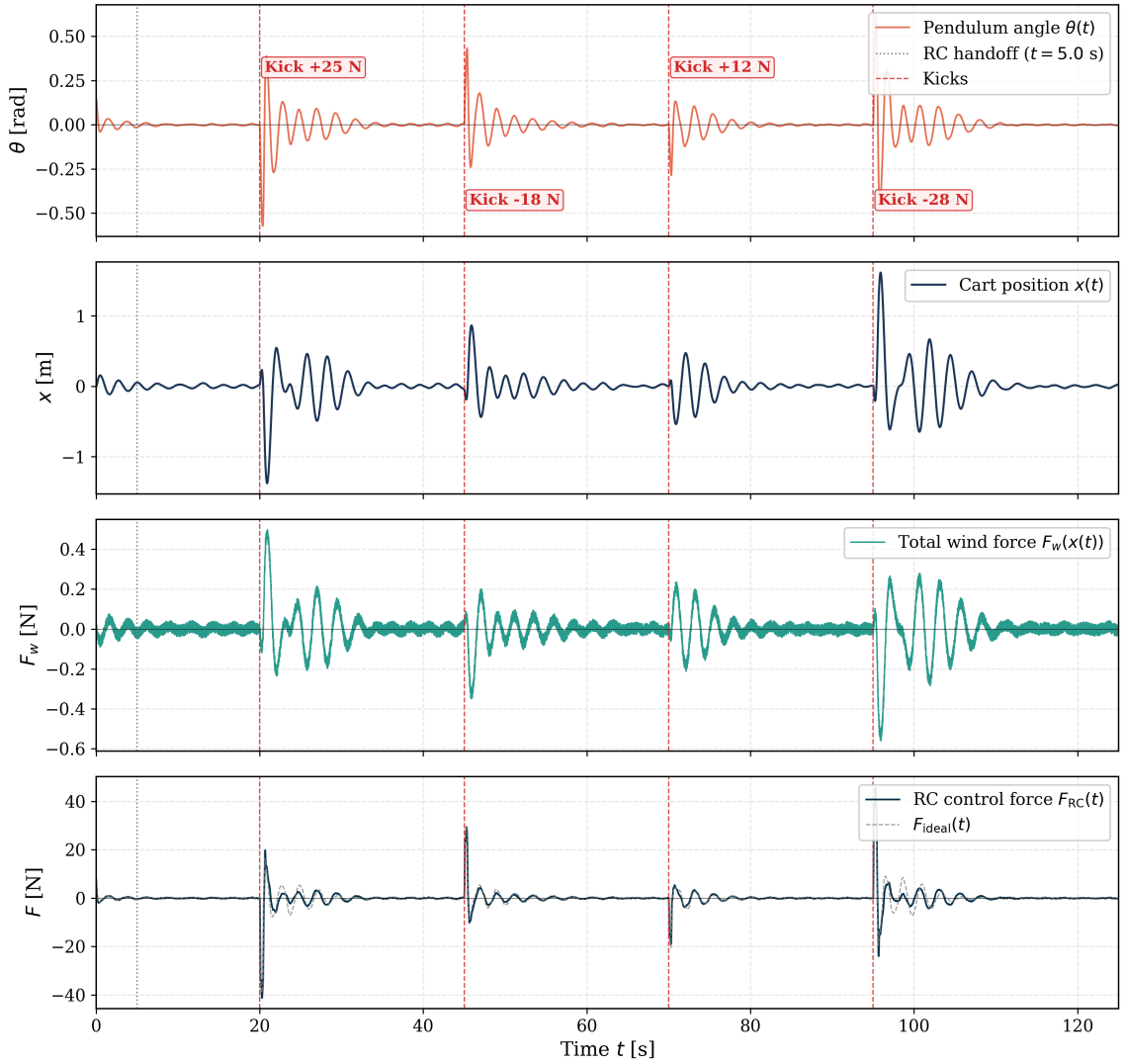

Figure 12: Autonomous closed-loop dynamic test over $T_{\text{test}} = 120$ s under novel turbulence and four external disturbance kicks. From top to bottom: pendulum angle $\theta(t)$, cart position $x(t)$, wind force $F_w(x(t))$, and autonomous control force $F_{\text{RC}}(t)$ versus ideal full-state controller force $F_{\text{ideal}}(t)$. Dashed red lines mark disturbance kicks.

As shown in Figure 12, the autonomous control force closely tracks the full-state controller ($\text{MSE}_{\text{test}} = 1.7767$, $R^2 = 0.8889$), successfully maintaining balance across all kicks, dampening oscillations, and steering the cart back to $x = 0$.

3.2.3. Why Does This Work?

This section aims to provide an intuition into how the ESN can compute the full-state control force $F\left(x, \dot{x}, \theta, \dot{\theta}\right)$ knowing only the scalar angle $\theta(t)$ and its past history.

Combining equations (16) to (19), the equations of motion can be written as $\ddot{x} = f(\boldsymbol{q})$ and $\ddot{\theta} = g(\boldsymbol{q})$. Differentiating $\ddot{\theta}$ with respect to time and substituting $\ddot{x}$ yields:

$$\dddot{\theta} = \frac{\partial g}{\partial x}\dot{x} + \frac{\partial g}{\partial \dot{x}} f(\boldsymbol{q}) + \frac{\partial g}{\partial \theta}\dot{\theta} + \frac{\partial g}{\partial \dot{\theta}}\ddot{\theta} \equiv h(\boldsymbol{q}). \tag{21}$$

Because time derivatives of θ can be inferred from θ's history[9], the system provides two equations for the unmeasured pair $(x, \dot{x})$:

$$\begin{cases} g\left(x, \dot{x}, \theta, \dot{\theta}\right) = \ddot{\theta} \\ h\left(x, \dot{x}, \theta, \dot{\theta}\right) = \dddot{\theta}. \end{cases} \tag{22}$$

Whenever the Jacobian:

$$\boldsymbol{J}_{x,\dot{x}} = \begin{pmatrix} \frac{\partial g}{\partial x} & \frac{\partial g}{\partial \dot{x}} \\ \frac{\partial h}{\partial x} & \frac{\partial h}{\partial \dot{x}} \end{pmatrix} \tag{23}$$

is non-singular ($\det\left(\boldsymbol{J}_{x,\dot{x}}\right) \neq 0$), equations (22) locally determine $(x, \dot{x})$. This does not mean that the ESN solves for x and $\dot{x}$ analytically, but rather that there exists a mapping from $\theta(t)$ and its history to the control force $F(t)$, and that the readout learns to approximate it as accurately as possible.

[9] For instance, discrete finite differences such as $\dot{\theta}(k) \approx \frac{\theta(k)-\theta(k-1)}{\Delta t}$.

4. Biological Reservoir: *C. elegans* Connectome

In this section, we investigate a biological RNN using the synaptic connectome of the nematode *Caenorhabditis elegans* as a reservoir.

The connectivity data is obtained from the *EleganSign* database[10] [7], which provides both the synapse number and the predicted sign of each neural connection (excitatory + or inhibitory −).

A connectome matrix $\boldsymbol{W}^c$ is constructed by assigning the (i, j) entry the value of the synapse number between source neuron i and target neuron j with its respective sign. Ambiguous signs ("complex" or "no pred") are assigned an excitatory sign with probability p_+ and an inhibitory sign with probability $1 - p_+$. Throughout this section, we set $p_+ = 0.5$ unless stated otherwise. The resulting connectome matrix is depicted in Figure 13.

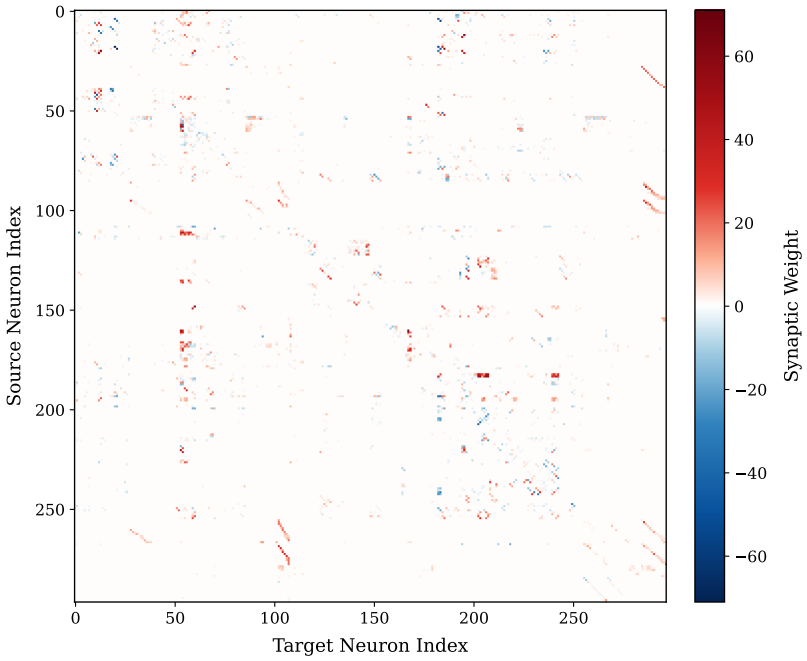

Figure 13: Colormap of the signed *C. elegans* connectome matrix $\boldsymbol{W}^c$ ($N = 297$ neurons, 2548 active connections, sparsity $s = 0.97$). Red indicates excitatory connections (+), blue indicates inhibitory connections (−), and white indicates no connection (0). Ambiguous connections are assigned a positive sign with probability $p_+ = 0.5$.

4.1. Short-Term Memory Capacity

We evaluate the memory retention of this biological reservoir by using the Short-Term Memory capacity task [5]. The reservoir is driven by a standardized ($\mu = 0$, $\sigma = 1$) random input signal $u(k)$, and its readout $\boldsymbol{W}^{\text{out}}$ is trained to reconstruct delayed versions of the input $d(k) = u(k - \tau)$ for increasing delays $\tau \in [0, 50]$.

The internal state evolves according to (2) under input scaling ζ and spectral radius ρ. We quantify memory retention at delay τ via the memory function:

$$\text{MF}(\tau) = r^2[y(k), u(k - \tau)] \in [0, 1], \tag{24}$$

[10]More specifically, the *PNS deleted* database, which does not include the pharyngeal nervous system neurons.

where $y(k)$ is the trained readout output and $r[\cdot,\cdot]$ is the Pearson correlation coefficient. A value of $\mathrm{MF}(\tau) = 1$ denotes perfect recall, whereas $\mathrm{MF}(\tau) = 0$ indicates complete memory loss. The total memory capacity is defined as:

$$\mathrm{MC} = \sum_{\tau=0}^{\tau_{\max}} \mathrm{MF}(\tau). \tag{25}$$

Figure 14 shows the memory function curve of the biological connectome for $\rho = 0.9$ and $\zeta = 0.5$. For comparison, we also show the memory function of five random reservoirs with the same number of neurons ($N = 297$, $W_{0,ij} \in \mathcal{U}(-1, 1)$) but with a much lower sparsity $s = 0.2$.

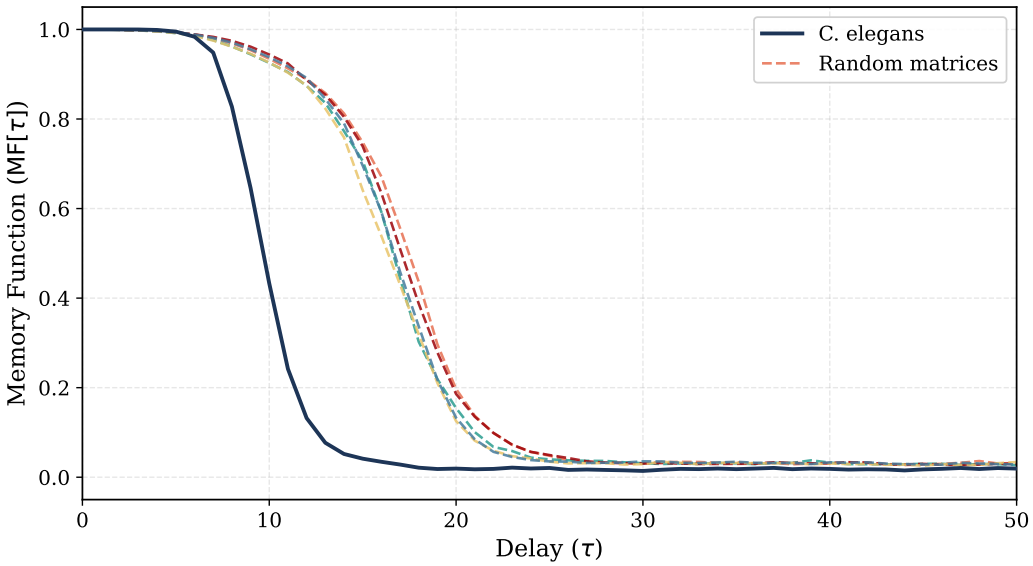

Figure 14: Memory function $\mathrm{MF}(\tau)$ across delay horizon $\tau \in [0, 50]$ for the *C. elegans* connectome ($N = 297$, $p_+ = 0.5$, $\mathrm{MC} = 11.04$) compared against five random reservoirs ($N = 297$, $s = 0.2$, average $\mathrm{MC} = 17.90$), all evaluated at $\rho = 0.9$ and $\zeta = 0.5$.

As shown in Figure 14, for delays $\tau < 7$, the connectome's memory function remains close to 1, indicating accurate recall of recent inputs. However, as τ increases, the memory function decays rapidly towards zero (dropping to approximately 0.4 at $\tau = 10$). Notably, the biological *C. elegans* connectome achieves a total memory capacity of $\mathrm{MC} = 11.04$, whereas the five random reservoirs ($N = 297$, $s = 0.2$) achieve on average a higher total memory capacity of $\mathrm{MC} = 17.90$. This shows that the biological connectome is particularly inefficient in the short-term memory test.

We can also investigate the influence of the spectral radius ρ and input scaling ζ on the total memory capacity of the connectome by performing a two-dimensional parametric sweep (Figure 15).

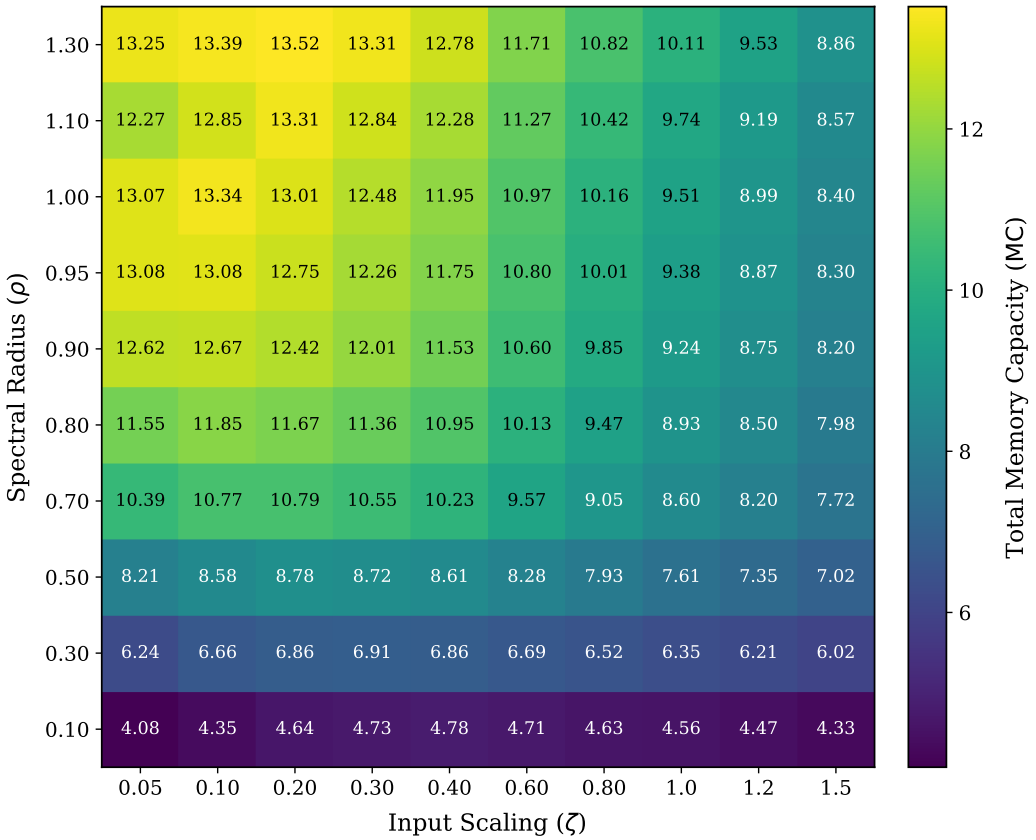

Figure 15: Total memory capacity of the *C. elegans* connectome reservoir across a discrete grid of spectral radius $\rho \in [0.10, 1.30]$ and input scaling $\zeta \in [0.05, 1.50]$, evaluated with $p_+ = 0.5$ and delay horizon $\tau_{\max} = 50$.

As observed in Figure 15, the memory capacity is maximized when ρ is close to unity and ζ is small ($\zeta < 0.30$). This is consistent with results from Section 2.2, where operating near $\rho \approx 1$ slows down internal state decay, allowing past inputs to persist longer in the network[11]. To explain the advantage of a low input scaling ζ, we use a result from [2] which states that a network equipped with a linear activation function possesses maximal memory capacity[12]. By choosing a low input scaling ζ, we keep neuron activations confined to the linear region of the $\tanh(\cdot)$ activation function, thereby enhancing linear memory retention.

Finally, we analyze how the excitatory/inhibitory sign balance of ambiguous synapses (p_+) affects the connectome's memory capacity. Fixing the operating point at $(\rho, \zeta) = (0.95, 0.10)$, we sweep p_+ from 0% to 100% in increments of 5%, evaluating five independent random realizations per percentage (Figure 16). We observe that the memory capacity peaks at the 0% and 100% extremes. Across the entire $\boldsymbol{W}^c$ matrix, these extremes correspond to global non-zero synaptic balances of 38.50% positive (61.50% negative) at $p_+ = 0\%$ and 88.74% positive (11.26% negative) at $p_+ = 100\%$.

[11] For $\rho > 1.0$, the internal state does not decay over time, which explains why larger spectral radii can also reach higher memory capacities, although dynamic instabilities may arise.

[12] Actually, this maximum memory capacity is demonstrated to be $\mathrm{MC} = N$, where N is the number of units [2].

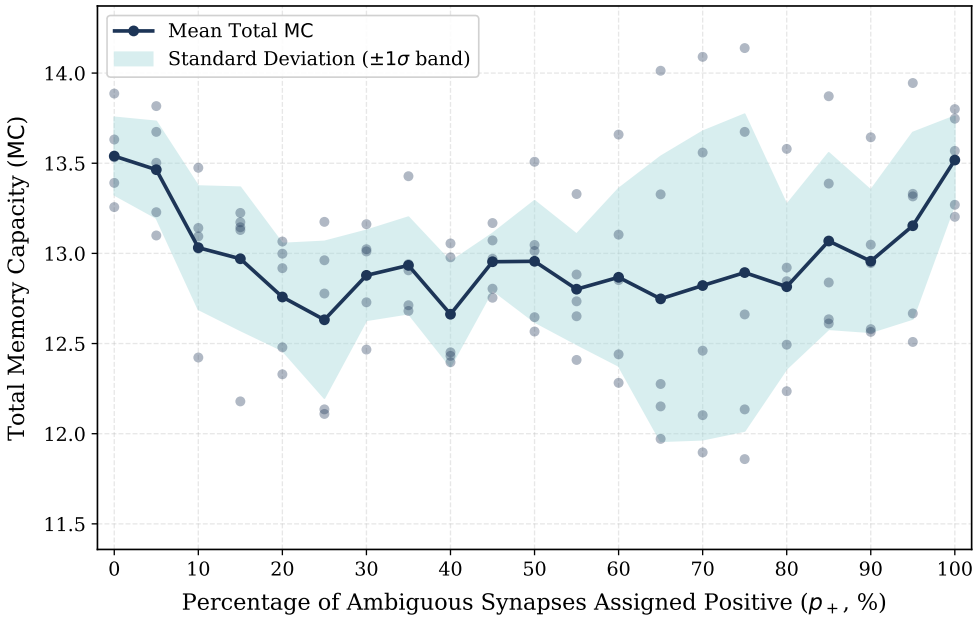

Figure 16: Total memory capacity as a function of the percentage of ambiguous synapses assigned a positive sign ($p_+ \in [0\%, 100\%]$) at fixed operating point $(\rho, \zeta) = (0.95, 0.10)$. The dark blue line shows the mean across five independent random realizations of the signed connectome, the shaded ribbon indicates the $\pm 1\sigma$ standard deviation band, and individual trial runs are plotted as scatter points.

5. Conclusion

In this work, we explored Echo State Networks from theoretical foundations to practical applications in chaotic forecasting, partial-observability control, and biological neural architectures.

First, by analyzing autonomous ESNs, we verified that the spectral radius ρ controls the reservoir's dynamical regimes, governing the transition from a contracting regime ($\rho < 1$), where the reservoir possesses the Echo State Property, to non-contracting regimes exhibiting periodic or chaotic dynamics as the spectral radius increases beyond unity.

In closed-loop forecasting of the chaotic Lorenz system, we observed that while small errors inevitably accumulate, causing the point-by-point trajectory ("weather") to diverge, the autonomous reservoir accurately preserves the global geometry of the attractor ("climate").

In control applications, we demonstrated that an ESN can stabilize an inverted cart-pole system relying solely on pole angle measurements, showing that the network implicitly reconstructs unobserved state variables, such as cart position and velocity, directly from temporal history.

Finally, we studied the *C. elegans* connectome as a biological reservoir. While it exhibited limited performance in the short-term memory test, it allowed us to show that memory capacity heavily depends on the spectral radius and input scaling hyperparameters. Additionally, we found that the balance of excitatory and inhibitory synaptic signs also influences the network's retention capacity.

Overall, these results highlight how Reservoir Computing's core principle of training simple readouts over nonlinear recurrent networks provides a robust framework for addressing a wide variety of complex dynamical challenges.

Bibliography

[1] G. Chen, "A Gentle Tutorial of Recurrent Neural Network with Error Backpropagation." [Online]. Available: https://arxiv.org/abs/1610.02583

[2] H. Jaeger, "Tutorial on training recurrent neural networks, covering BPPT, RTRL, EKF and the echo state network approach," *GMD-Forschungszentrum Informationstechnik, 2002.*, vol. 5, p. , Jan. 2002.

[3] K. Nakajima, "Physical reservoir computing—an introductory perspective," *Japanese Journal of Applied Physics*, vol. 59, no. 6, p. 60501, May 2020, doi: 10.35848/1347-4065/ab8d4f.

[4] H. Jaeger, "The" echo state" approach to analysing and training recurrent neural networks-with an erratum note'," *Bonn, Germany: German National Research Center for Information Technology GMD Technical Report*, vol. 148, p. , Jan. 2001.

[5] K. Inoue *et al.*, "Reservoir Computing Bootcamp—From Python/NumPy Tutorial for the Complete Beginners to Cutting-Edge Research Topics of Reservoir Computing," *Chaos: An Interdisciplinary Journal of Nonlinear Science*, vol. 36, no. 2, p. 23109, 2026, doi: 10.1063/5.0283386.

[6] E. N. Lorenz, "Deterministic Nonperiodic Flow," *Journal of the Atmospheric Sciences*, vol. 20, no. 2, pp. 130–141, 1963, doi: 10.1175/1520-0469(1963)020<0130:DNF>2.0.CO;2.

[7] B. G. Fenyves, G. S. Szilágyi, Z. Vassy, C. Sőti, and P. Csermely, "Synaptic polarity and sign-balance prediction using gene expression data in the Caenorhabditis elegans chemical synapse neuronal connectome network," *PLoS Computational Biology*, vol. 16, no. 12, p. e1007974, 2020, doi: 10.1371/journal.pcbi.1007974.

A simple model of active reproducing matter

Javier Rodríguez-Escalona Sánchez, Emilio Hernández-García
Instituto de Física Interdisciplinar y Sistemas Complejos, IFISC (CSIC-UIB)
Campus Universitat de les Illes Balears, E-07122 Palma de Mallorca, Spain

Abstract

Motility and reproduction coexist in many biological systems, from bacterial colonies to migrating tissues, yet most models of collective motion rely on an explicit rule that makes neighbours align. We ask whether orientational order can instead emerge purely from the demographic fluctuations of a reproducing population, with no interaction between agents at all. Starting from the passive Brownian bug model of Young, Roberts and Stuhne, where critical branching and diffusion alone already generate transient spatial clustering, we let every agent inherit a self-propulsion direction from its parent and ask how much of the population actually needs to share a common ancestor for global alignment to appear. We then follow Takamura and Saito in adding a density-dependent reproduction rate representing competition for resources, and ask whether this competition is a genuinely separate route to alignment or simply a faster way of reaching the same underlying state.

1 Introduction

Many biological systems involve populations that reproduce and move at the same time, from bacterial colonies spreading across a surface to migrating tissues, swimming microorganisms, and dispersing plant seeds [1]. In most of these systems reproduction and motion are inseparable, since offspring appear close to their parents and only move away from them as time passes. Understanding how spatial and orientational patterns emerge from this coupling is therefore relevant well beyond any particular species or system.

Classical models of collective motion, such as the Vicsek model [2], reproduce ordered, flock-like behaviour by imposing an explicit rule that makes neighbouring agents align their direction of motion. This approach has been very successful at reproducing the kind of coherent motion seen in bird flocks, fish schools, and bacterial swarms, but it also raises a more basic question. Real organisms do not compute the average direction of their neighbours and steer towards it, so whatever mechanism produces collective order in a biological population has to emerge from simpler, local rules, and reproduction is one of the most universal of these rules that standard active matter models tend to leave out.

The starting point for addressing this question is the Brownian bug model of Young, Roberts and Stuhne [3], in which a population of otherwise non-interacting agents undergoes stochastic birth, death and diffusion. Despite the complete absence of any interaction, this model already produces persistent spatial clustering, simply because offspring are placed on top of their parents and only slowly diffuse away. Later extensions of this model introduced competition for resources between nearby agents, leading to more structured, crystal-like spatial patterns [4], but none of these extensions considered agents with their own direction of motion.

In this work we ask whether orientational order can emerge purely from the demographic fluctuations of a proliferating population, without any interaction between agents at all. We build up to this question in stages. We first revisit the passive Brownian bug model and show that its spatial clustering has a genealogical counterpart, a coalescent process in which the whole population eventually descends from a single ancestor. We then give every agent a self-propulsion direction inherited at birth and ask how much of this genealogical coalescence is actually needed for the population to align. Finally, we follow Takamura and Saito [4] in adding a density-dependent reproduction rate representing competition for resources, and ask whether this competition provides a genuinely different route to alignment or simply accelerates the same underlying process already present in the passive model.

2 Young Model

2.1 Model definition

Our work starts with the Brownian bug model introduced by Young [3]. This is a minimal, individual based model that shows how spatial clustering emerges naturally from local, uncorrelated rules, without any interaction between the agents themselves. Each agent i is tracked purely by its position $\mathbf{r}_i(t) = (x_i, y_i)$ on a square domain of size $L \times L$ with periodic boundary conditions. The dynamics rely on two independent stochastic processes that take place at every time step dt.

The first of these processes concerns reproduction and death. Agents reproduce with a probability $p\,dt$ and die with a probability $q\,dt$, both completely independent of other agents and of their current position. When a new agent is born, it is placed exactly where its parent stands, so that $\mathbf{r}_{i'}(t) = \mathbf{r}_i(t)$. Throughout this study we work at the critical point of the branching process, that is $p = q$, so the population does not systematically grow or shrink, but instead its size undergoes an unbounded random walk over time. Additionally, we choose a starting population N_0 that is much larger than the number of generations we intend to simulate, simply to avoid premature extinction.

The second process is random motion. Between reproduction events, agents perform independent Brownian motion,

$$\frac{d\mathbf{r}_i}{dt} = \boldsymbol{\xi}_i(t), \qquad \langle \xi_i^\alpha(t)\, \xi_j^\beta(t') \rangle = 2D\, \delta_{ij}\, \delta^{\alpha\beta}\, \delta(t - t'), \tag{2.1}$$

where D is the diffusion coefficient and $\alpha, \beta \in \{x, y\}$. Discretizing Eq. (2.1) with a time step dt gives the update rule actually used in our simulations,

$$\mathbf{r}_i(t + dt) = \mathbf{r}_i(t) + \sqrt{2D\,dt}\; \mathbf{g}_i(t), \tag{2.2}$$

where $\mathbf{g}_i(t)$ is a two dimensional vector of independent standard Gaussian random numbers, resampled at every step.

What matters most here is that agents never interact directly. There are no forces, no alignment rules, and no competition between them. For this reason, any spatial structure that we observe emerging is due entirely to the interplay between reproduction and diffusion.

2.2 Emergence of clustering

Even though birth, death, and motion are all local and do not depend on one another, the model does not remain spatially uniform. Since newborn agents appear exactly on top of their parents, every reproduction event creates a pair of perfectly correlated agents separated by zero distance. This correlation only fades away as the two descendants random walk apart from each other. When D is small, they drift apart much more slowly than the typical time between reproduction events. As a consequence, descendants of the same ancestor remain close together in space for many generations, and their numbers grow rapidly through the critical branching process itself.

The whole population therefore ends up organized into patchy, transient clusters separated by empty regions, despite the complete absence of any attractive force in the underlying rules. This can be seen in Fig. 1, where particles are coloured according to their initial y coordinate.

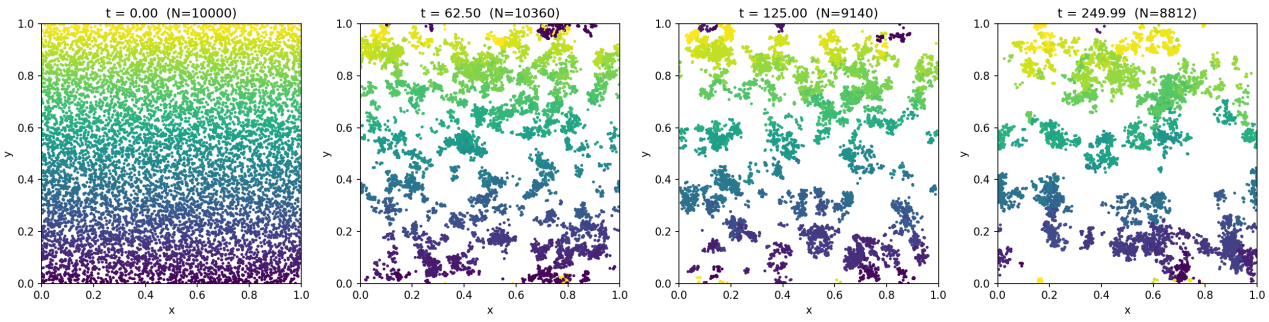

Figure 1: Snapshots of the Young model at $D = 5 \times 10^{-6}$ and $N_0 = 10^4$. Agents are coloured according to their starting y coordinate.

This clustering can be measured through the pair correlation function,

$$g(r) = \frac{1}{C_{\text{pair}}} \left\langle \frac{(L/2)^2}{(r+\Delta r)^2 - r^2} \, h(r) \right\rangle , \tag{2.3}$$

where $h(r)$ is the histogram of distances between pairs with bin width Δr, C_{pair} is the total number of sampled pairs, and the brackets $\langle \cdot \rangle$ represent a time average once the system has reached a stationary state. By definition, a completely uniform, or Poisson, distribution gives $g(r) = 1$, so any deviation from this value indicates the presence of correlation. As shown in Fig. 2, $g(r)$ rises sharply at small distances r and then falls back towards 1 at larger distances. This confirms that agents tend to be tightly packed at short range, consistent with the clustering already visible in Fig. 1. Meanwhile, the overall population size simply fluctuates around N_0 without showing any clear trend, which is exactly what we would expect once $p = q$ is imposed.

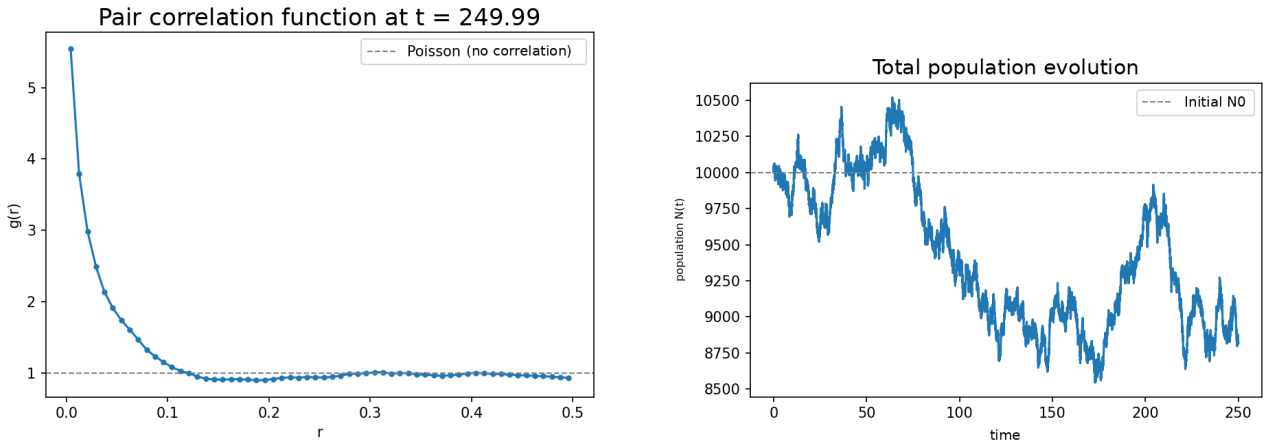

(a) (b)

Figure 2: (a) Pair correlation function $g(r)$ for the Young model, computed using Eq. (2.3) at $t = 250$. The dashed line at $g(r) = 1$ shows the value expected if agents were scattered randomly with no correlation at all, following a Poisson distribution. (b) Total population size $N(t)$ for the Young model at the critical point $p = q$.

2.3 Genealogical coalescence: family fixation

This clustering mechanism also carries an interesting genealogical dimension. Suppose we assign every initial agent a unique family label, which is then passed on directly to its offspring. Naturally, the total number of distinct families can only decrease over time, since an agent that dies without leaving offspring causes its family line to be lost forever. This process is essentially the classic genetic drift familiar from population genetics [5]. Starting with $N_0 = 1000$ distinct families, we observe that the number of surviving families drops quickly until only one remains. This means the entire population ends up descending from a single common ancestor well before the whole population collapses, as illustrated in Fig. 3.

When this experiment is repeated for different diffusion coefficients D, keeping the same random seed for the sequence of births and deaths so that the comparison is fair, we find that the demographic and genealogical dynamics do not depend on D at all. The population size $N(t)$ and the family count evolve in exactly the same way across every value of D we tested. This is expected, since D only affects how agents move through Eq. (2.2), while birth, death, and the inheritance of a family label do not depend on where an agent happens to be.

What does depend strongly on D, however, is the spatial footprint left by this coalescence process. We measure this through $g(r \to 0)$, the pair correlation function evaluated at very short distances. As expected, a smaller D produces a much higher $g(r \to 0)$, as shown in Fig. 4, because descendants take longer to drift away from their ancestors and therefore remain tightly clustered. This is clearly

visible in Fig. 3. For all three values of D, the population converges to a single family by $t = 700$, yet the spatial spread of that final family is noticeably more compact when D is low.

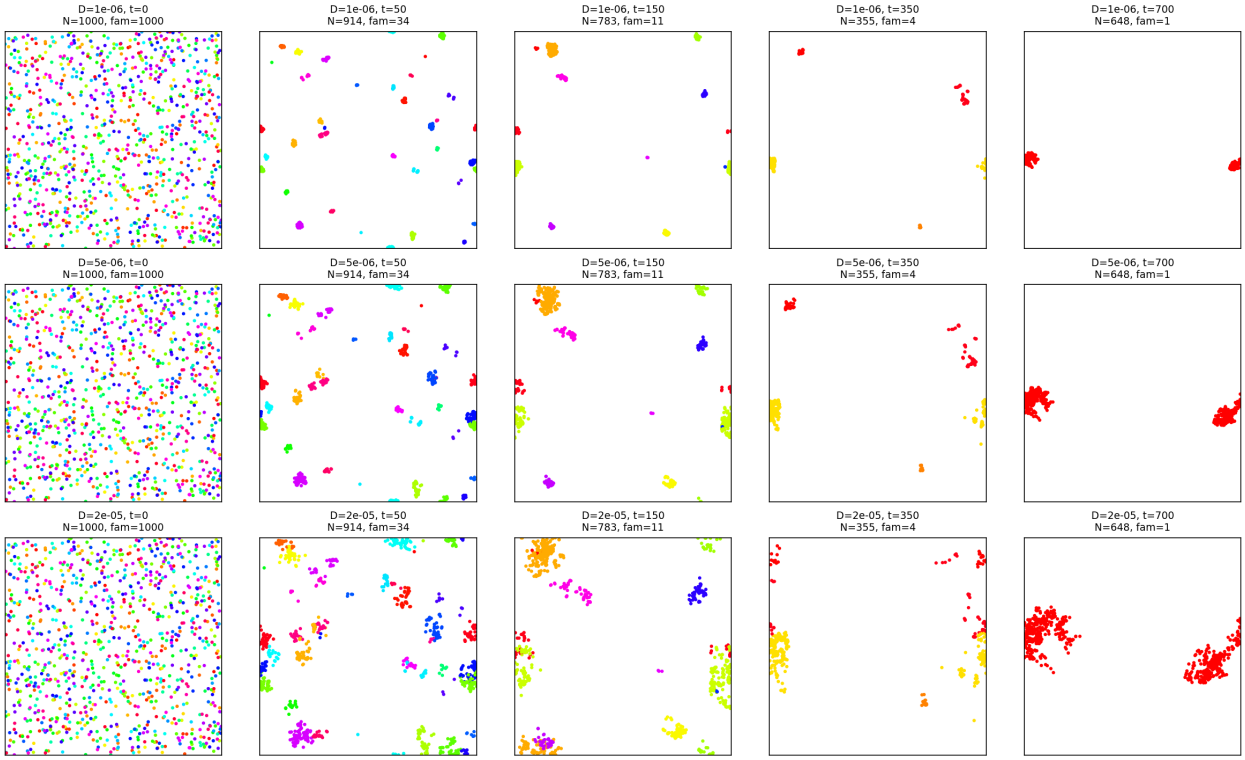

Figure 3: Family coalescence in the Young model for three different diffusion coefficients D, shown by rows, at fixed points in time, shown by columns. Colours represent the initial family label of each agent. The number of families decreases steadily until only one remains, that is fixation, by $t = 700$ for every value of D. The demographics driving this fixation are unaffected by D, while only the spatial spread of the surviving family changes, becoming noticeably tighter for lower values of D.

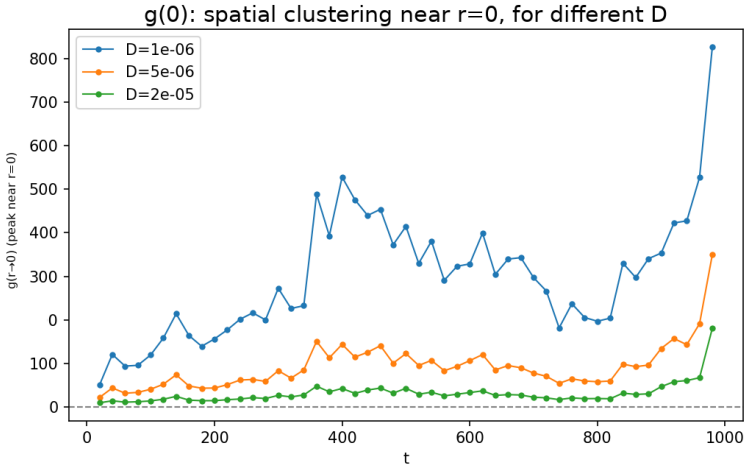

Figure 4: Pair correlation function evaluated at very short separation, $g(r \to 0)$, plotted over time for three diffusion coefficients. Lower values of D produce noticeably stronger clustering, reflected in a higher $g(r \to 0)$ peak, since descendants spread out more slowly.

2.4 Adding self-propulsion

The Young model discussed so far treats agents as passive Brownian particles, since their only property is a position $\mathbf{r}_i$, and clustering emerges purely from the coupling between critical branching and

diffusion. We now extend this model by giving every agent a self-propulsion direction θ_i, following the active Brownian bug formulation of Takamura and Saito [4]. At this stage we keep the reproduction rate constant, exactly as in the original Young model, and we do not yet include the density dependent competition term that Takamura and Saito introduce through Eq. (4) of their paper. This choice is intentional and allows us to isolate the effect of self-propulsion and polarity inheritance on their own, before any competitive interaction is added in a later section.

The equations of motion then become

$$\frac{dx_i}{dt} = \xi_{x_i} + v_0 \cos\theta_i, \tag{2.4}$$

$$\frac{dy_i}{dt} = \xi_{y_i} + v_0 \sin\theta_i, \tag{2.5}$$

$$\frac{d\theta_i}{dt} = \xi_{\theta_i}, \tag{2.6}$$

where v_0 is the self-propulsion speed, ξ_{x_i} and ξ_{y_i} are the same translational noise terms defined in Eq. (2.1), and ξ_{θ_i} is an independent white Gaussian noise satisfying $\langle \xi_{\theta_i}(t) \rangle = 0$ and $\langle \xi_{\theta_i}(t)\xi_{\theta_i}(t') \rangle = 2D_\theta\,\delta(t-t')$, with D_θ the rotational diffusion coefficient. Reproduction and death still follow the same critical rule described above, with $p = q$, with the one addition that a newborn agent now also inherits its parent's propulsion direction, $\theta_{i'} = \theta_i$, in addition to inheriting its position and, when tracked, its family label.

To quantify orientational order we use the same order parameter as Takamura and Saito,

$$S(t) = \frac{1}{N(t)} \left| \sum_{j=1}^{N(t)} \exp(i\theta_j) \right|, \tag{2.7}$$

where $N(t)$ is the population size at time t. $S(t)$ equals 1 when every agent points in exactly the same direction, and it drops towards 0 when the directions are spread uniformly around the circle. We also define an angular correlation function, analogous to $g(r)$ but built from orientations rather than positions,

$$C(r) = \langle \cos(\theta_i - \theta_j) \rangle_{r_{ij} \approx r}\,, \tag{2.8}$$

where the average is taken over every pair (i, j) whose separation r_{ij} falls within the bin centred at r, again combined with a time average over the stationary regime. A value of $C(r) = 1$ means that agents separated by that distance always share the same direction, while $C(r) = 0$ means their directions are statistically independent of each other.

In order to see how family inheritance interacts with this angular dynamics, we repeated the coalescence experiment from the previous subsection, now with self-propulsion switched on, comparing different rotational diffusions. Because the population size needed to remain small enough for family fixation to occur within a reasonable simulated time, we used $N_0 = 2000$ here instead of the larger populations used elsewhere. Since the birth, death, and family inheritance rules do not depend on θ_i or on D_θ, the demographic and genealogical trajectories are once again identical between the two runs, just as they were identical across different values of D in the previous subsection, as shown in Fig. 6. What differs completely is the orientational behaviour. Figure 7 shows $S(t)$ together with the number of surviving families for both values of D_θ. For $D_\theta = 10^{-5}$, $S(t)$ climbs steadily and saturates close to 1 well before the population reaches family fixation, and it remains high afterwards. Once nearly every agent descends from the same recent ancestor, and mutation is weak enough not to erase the inherited direction, the whole population ends up pointing the same way. For $D_\theta = 2 \times 10^{-3}$, by contrast, $S(t)$ keeps fluctuating with no clear trend even at the exact moment the population fixes to a single family, reaching only $S = 0.131$ at $t = 1683$, compared with $S = 0.989$ for the low D_θ run at that same instant. Rotational diffusion is strong enough to randomize the inherited direction over the many generations it takes for a single family to take over the whole population, so common ancestry alone does not guarantee alignment. This is confirmed directly by $C(r)$, shown together with $g(r)$ in Fig. 5. For the low D_θ run, $C(r)$ stays close to 1 across the whole range of r, while for the high D_θ run it decays from about 0.9 at short range down to nearly 0 by $r \approx 0.5$, showing that orientation only remains correlated over short genealogical and spatial distances.

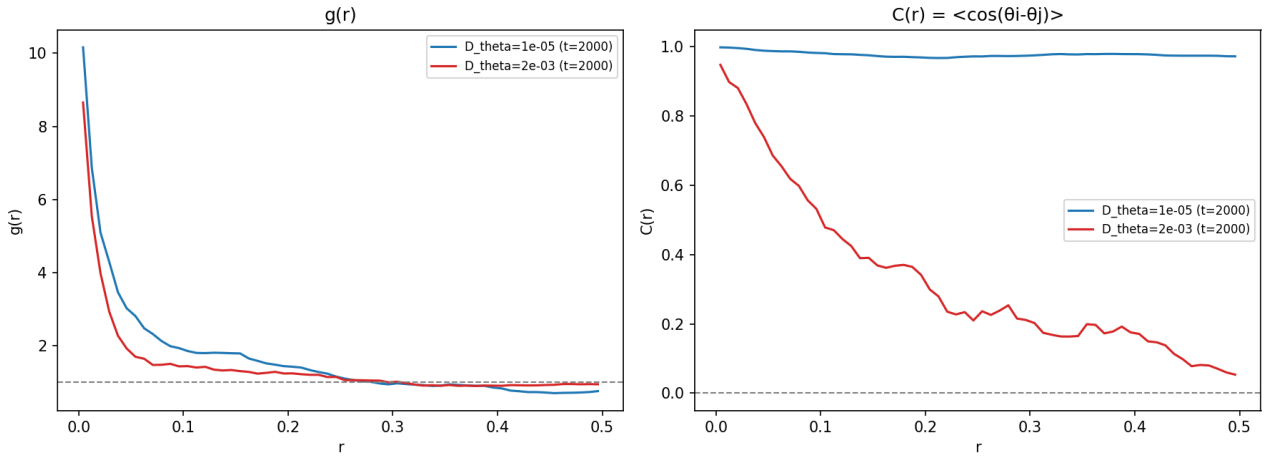

Figure 5: Pair correlation function $g(r)$, left, and angular correlation function $C(r)$, right, for the self-propulsed Young model without competition, compared between a small and a large rotational diffusion coefficient D_θ. Both curves are evaluated at the last simulated snapshot for each run.

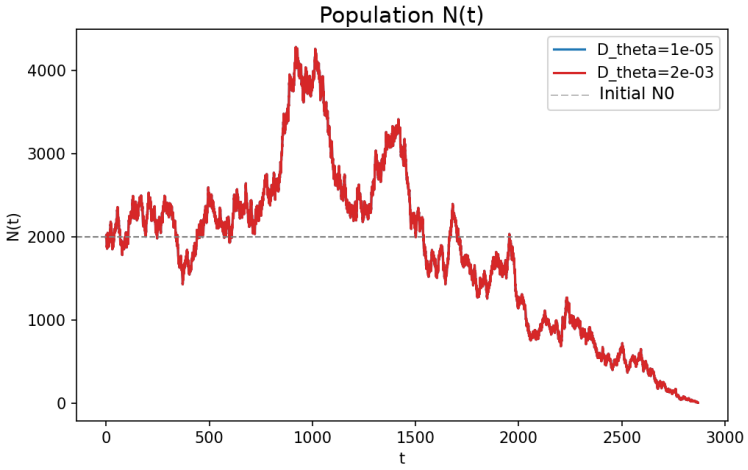

Figure 6: Total population $N(t)$ for the self-propulsed Young model without competition, for the two values of D_θ tested. The two curves overlap exactly, confirming that the demographic dynamics does not depend on D_θ.

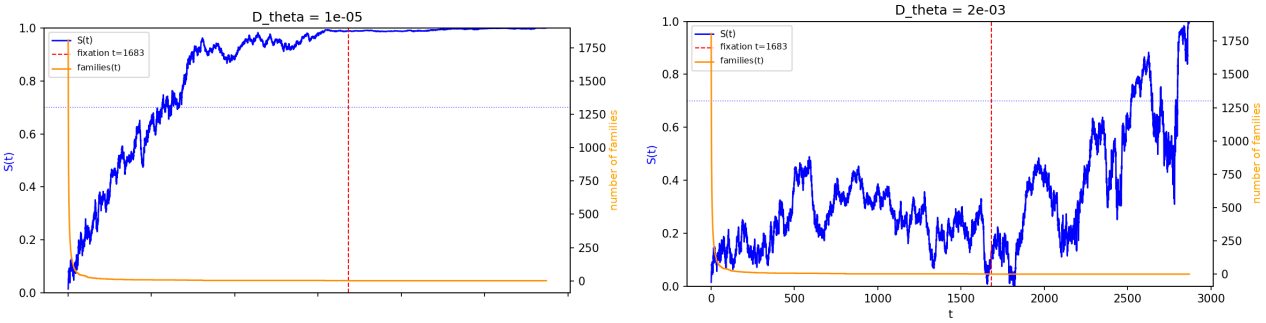

Figure 7: Orientational order parameter $S(t)$, in blue on the left axis, and number of surviving families, in orange on the right axis, for the self-propelled Young model without competition, for a small rotational diffusion $D_\theta = 10^{-5}$, left panel, and a large one $D_\theta = 2 \times 10^{-3}$, right panel. The vertical dashed line marks the moment the population fixes to a single family.

Figures 8 and 9 show the same sequence of snapshots for each value of D_θ, once coloured by initial family label and once by instantaneous direction θ, allowing the two panels for a given D_θ to be compared directly. For $D_\theta = 10^{-5}$, the two colourings become visually equivalent by the time fixation is reached. Once the population is dominated by a single family, it is also dominated by a single, narrow range of directions. For $D_\theta = 2 \times 10^{-3}$, the family panel still shows a single colour at $t = 1683$ and beyond, confirming fixation, while the direction panel remains a mixture of many colours throughout, with no visible correlation between spatial clusters and orientation. This offers perhaps the clearest illustration that, within this model, common ancestry and orientational order are related only when the rotational mutation rate is low enough for the inherited signal to survive the many generations that fixation requires.



(a) Coloured by initial family label.

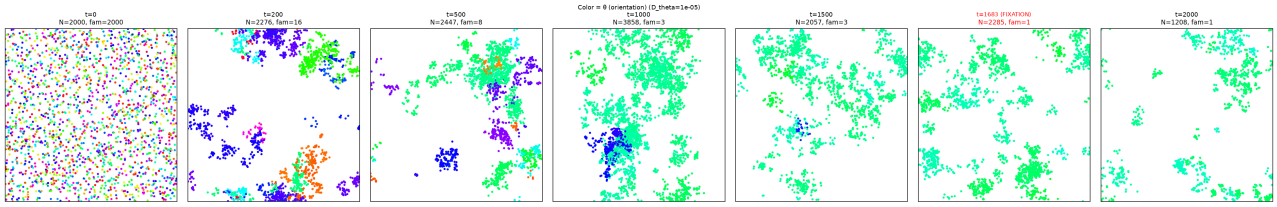

(b) Coloured by instantaneous direction θ.

Figure 8: Snapshots of the self-propelled Young model without competition, at $D_\theta = 10^{-5}$, coloured by family label, top, and by direction θ, bottom. The panel marked in red corresponds to the moment of family fixation.

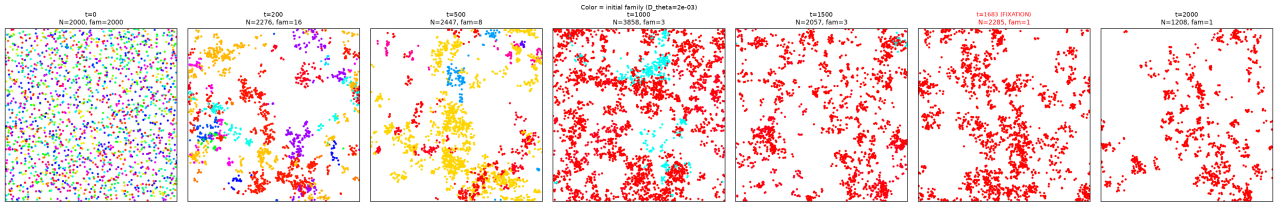

(a) Coloured by initial family label.

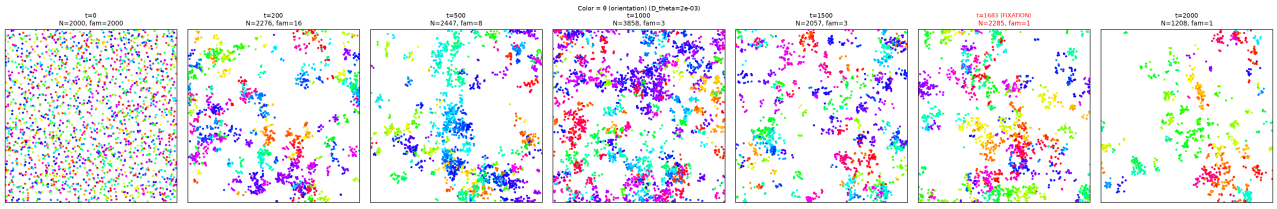

(b) Coloured by instantaneous direction θ.

Figure 9: Snapshots of the self-propelled Young model without competition, at $D_\theta = 2\times10^{-3}$, coloured by family label, top, and by direction θ, bottom. The panel marked in red corresponds to the moment of family fixation.

2.5 Order from genealogical drift across independent realizations

The results above come from a single random realization for each value of D_θ, so a natural concern is whether the outcome depends heavily on the particular sequence of births and deaths that happened to occur. To address this we repeated the self-propelled experiment, still without competition, for three independent seeds at each of the two rotational diffusion values, and recorded both $S(t)$ and the number of surviving families throughout each run.

Figure 10 shows the outcome for all six realizations. For $D_\theta = 10^{-5}$, every seed reaches $S = 0.7$ comparatively early, at values of the surviving family count ranging from 2 up to 7, well before any of the three runs reaches strict fixation to a single lineage. For $D_\theta = 2 \times 10^{-3}$, the picture is more varied. Two of the three seeds still cross the 0.7 threshold, though generally later and at a lower family count than in the low D_θ case, while the third seed never reaches it within the simulated window. This confirms that a single common ancestor is not a strict requirement for global order to appear. What seems to matter instead is that the number of independently evolving lineages has already dropped low enough for their average directions to align by chance, an effect that becomes more likely, and more stable once reached, the weaker the rotational mutation is.

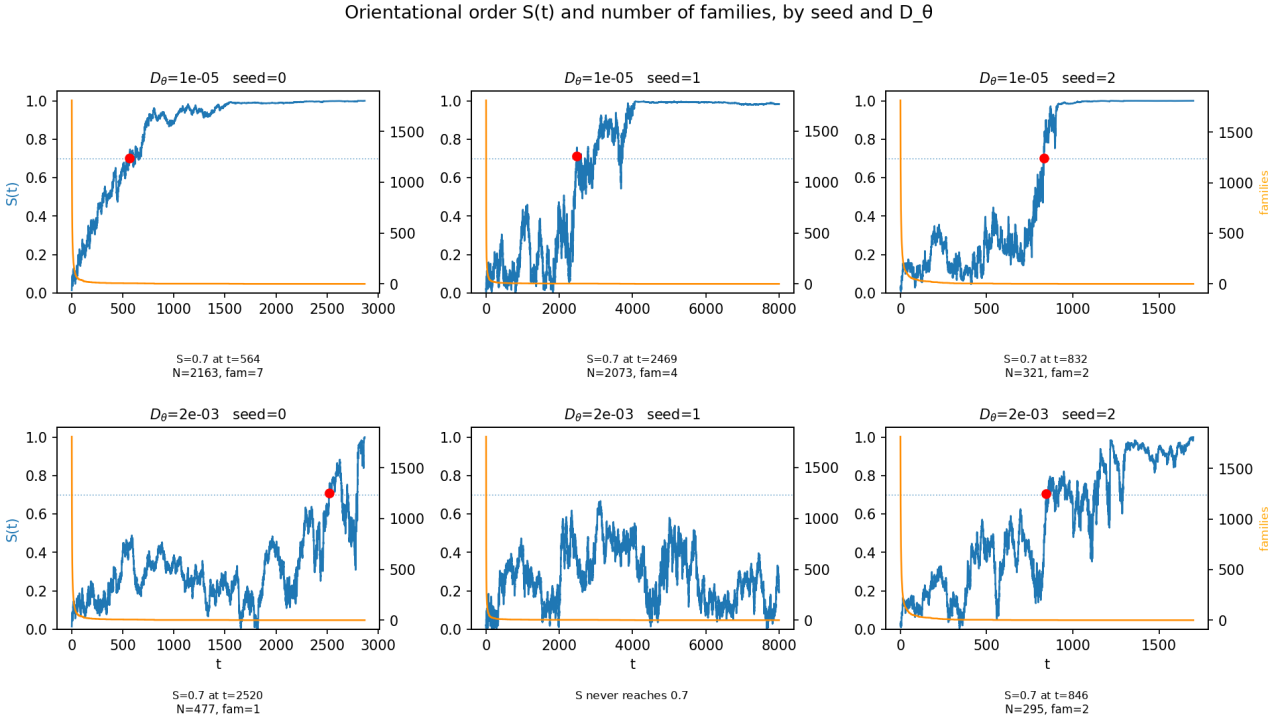

Figure 10: Orientational order parameter $S(t)$, blue, and number of surviving families, orange, for three independent seeds at each of two rotational diffusion values, $D_\theta = 10^{-5}$ top row and $D_\theta = 2 \times 10^{-3}$ bottom row. The red marker indicates the instant, if any, at which $S(t)$ first crosses the 0.7 threshold, together with the population size and family count reached at that instant.

The spatial signature of this effect is shown in Fig. 11, where each panel is taken at the exact instant $S(t)$ first crosses 0.7 for that realization, coloured by initial family label. Rather than a single dominant colour, most panels still show two or three surviving lineages, each occupying a distinct cluster, yet already sharing a common average direction. This is a useful complement to Figs. 8 and 9, which focused on the long time limit of a single realization. Taken together, both sets of results indicate that orientational order in this model is fundamentally a genealogical phenomenon, but one that does not need the genealogy to have fully resolved into a single family before becoming visible at the population level.

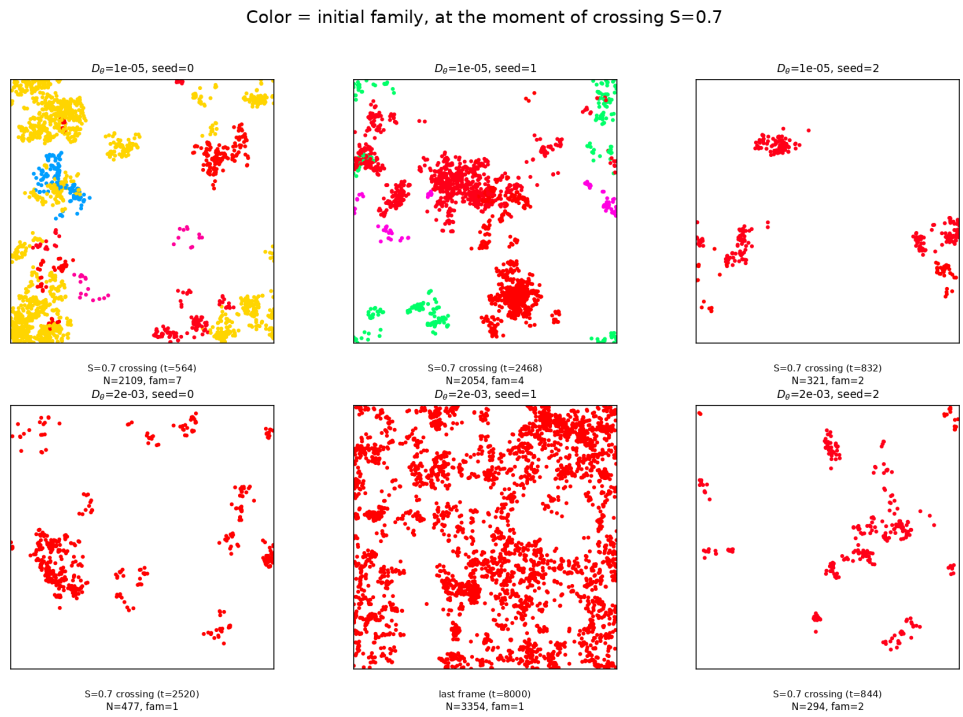

Figure 11: Snapshots coloured by initial family label, taken at the instant global order first crosses $S = 0.7$ for each of the six realizations shown in Fig. 10.

2.6 Adding the neighborhood-dependent reproduction rate

The self-propelled model discussed above still uses a constant reproduction rate, so any orientational order it develops comes only from genealogical drift. A single family eventually takes over the population, and that family only carries a common direction when D_θ is small enough for the inherited signal to survive. We now add the second ingredient of the active Brownian bug model, following Takamura and Saito [4], namely a reproduction rate that depends on local density and is meant to represent competition for a shared, limited resource such as nutrients.

Each agent i now carries its own reproduction rate $p_i(t)$, which decreases with the number of neighbours $N_i(t)$ found within a distance R of its position,

$$p_i(t) = \max\left(p_0\left(1 - \frac{N_i(t)}{N_s}\right),\ 0\right), \tag{2.9}$$

where p_0 is the maximum reproduction rate, reached when an agent has no neighbours at all, and N_s is a saturation parameter. Once an agent has N_s or more neighbours within R, its reproduction rate drops to zero. The death rate q remains constant and independent of position, exactly as before. Reproduction and death are then governed by

$$A \xrightarrow{p_i} A + A, \qquad A \xrightarrow{q} \varnothing, \tag{2.10}$$

so that, at every time step dt, agent i reproduces with probability $p_i(t)\,dt$, dies with probability $q\,dt$, and otherwise remains unchanged with probability $1 - p_i(t)\,dt - q\,dt$. As in the previous sections, a newborn agent inherits both the position and the propulsion direction of its parent.

Computing $N_i(t)$ for every agent at every time step is the most expensive part of the simulation, since in principle it requires comparing every pair of agents against each other. We use a k-d tree, specifically `cKDTree` from `scipy.spatial`, to find, for each agent, every neighbour within radius R without having to check all other agents explicitly. This is efficient here because $R = 0.1$ is small compared with the size of the box, so the tree can discard the vast majority of far away agents very quickly. To reduce the computational cost further, the neighbour count is only recomputed every 25 time steps rather than at every single step, since an agent's position changes very little compared with

R over that interval. This introduces a negligible approximation while making the long simulations required here, up to $t = 1000$ per phase, computationally feasible.

Following Takamura and Saito, we fix $p_0 = 0.85$, $q = 0.15$, $R = 0.1$, $N_s = 50$, $D_\theta = 2 \times 10^{-3}$, $L = 1$, and an initial population $M_0 = 1500$, and we explore four combinations of D, called D_r in their notation, and v_0 that they identify as representative of four distinct phases, namely periodic clustered (PC), spatially structured flocking (SSF), flocking (F), and disordered (D). To characterize each phase we use the same three quantities as before, now averaged over the second half of each run, from $t = 500$ to $t = 1000$, once the system has reached a statistically stationary state. These are the pair correlation function $g(r)$, its second peak value $g(r_2)$, used as a heuristic indicator of hexagonal spatial order since $g(r_2) > 1.2$ signals a clear hexagonal pattern, and the orientational order parameter $S(t)$, with $S > 0.7$ taken as the threshold for orientational order.

Figure 12 shows the resulting snapshots, $g(r)$ curves, and $S(t)$ time series for the four phases side by side. The PC phase shows a clearly oscillating $g(r)$ with a strong second peak, $g(r_2) = 1.74$, confirming a hexagonal spatial arrangement of clusters, while $S(t)$ stays consistently low, below 0.4 throughout the run. Clusters form and separate from one another because of the competition term, but since v_0 is small here, the resulting selection pressure on misaligned agents is too weak to produce global alignment. The SSF phase keeps a similarly strong hexagonal signature, $g(r_2) = 1.36$, while also reaching high orientational order, with $S(t)$ climbing steadily and crossing the 0.7 threshold at around $t = 750$. This is precisely the coexistence of spatial and orientational order that defines the SSF phase. The F phase shows the opposite combination, with $g(r_2) = 1.09$, close to the uncorrelated value of 1, so no hexagonal pattern is present, while $S(t)$ still reaches high values, above 0.8 by the end of the run. Finally, the D phase shows neither signature, with $g(r_2) = 1.05$ and $S(t)$ fluctuating below 0.4 throughout, since the large value of D_r used here disrupts any spatial or orientational structure before it has a chance to stabilize.

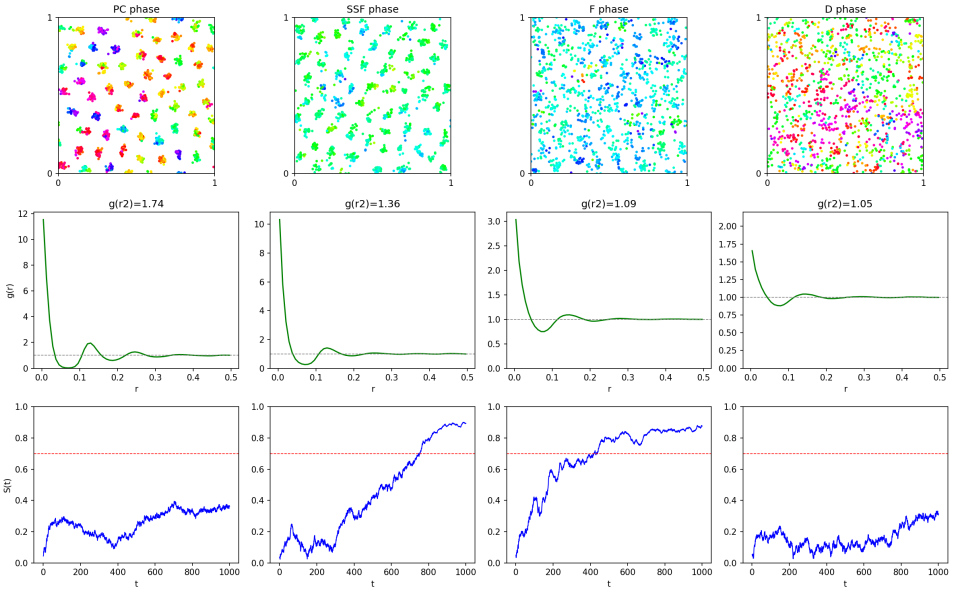

Figure 12: Snapshots, top row, coloured by propulsion direction θ, pair correlation functions $g(r)$, middle row, and orientational order parameter $S(t)$, bottom row, for the four phases of the active Brownian bug model with competition, namely periodic clustered (PC), spatially structured flocking (SSF), flocking (F), and disordered (D). Each column uses the values of D_r and v_0 reported by Takamura and Saito for the corresponding phase. The dashed line in the middle row marks $g(r) = 1$, the value expected without spatial correlation. The dashed line in the bottom row marks the $S = 0.7$ threshold used to identify orientational order.

It is worth comparing this result directly with the self-propelled model without competition discussed in the previous subsections. There, orientational order could appear through genealogical drift alone, but this generally required waiting for the number of surviving families to drop substantially, and reliable alignment after that point was only guaranteed for a very small rotational diffusion D_θ.

Here, in the SSF and F phases, $S(t)$ already exceeds 0.7 by $t \approx 750$ and $t \approx 550$ respectively, using the much larger $D_\theta = 2 \times 10^{-3}$ that previously prevented any lasting alignment except through drift. Competition therefore provides a considerably faster route to alignment. As Takamura and Saito explain, agents whose direction deviates from that of their neighbours tend to drift out of their cluster and into the low density regions between clusters, where the reproduction rate given by Eq. (2.9) is close to zero. Misaligned agents are therefore reproductively disadvantaged and are removed from the population more quickly than they would be through drift alone.

2.7 The role of competition and genealogical drift in the flocking phase

The comparison above shows that competition accelerates the emergence of orientational order, but it does not by itself establish that competition is the mechanism responsible for that order once it appears. Given the results of the previous subsections, an equally plausible explanation is that competition simply speeds up the same coalescence process already identified in the passive drift experiments, since local extinction due to crowding removes entire lineages from the population in the same way that ordinary death does, only at a higher effective rate wherever agents are densely packed.

To test this, we extended the family tracking used earlier to the competitive simulations of Fig. 12, assigning each of the $M_0 = 1500$ initial agents a unique label and following it through the run. Figure 13 shows the state of each phase at the end of the simulation, coloured once by instantaneous direction θ and once by initial family. The number of surviving families differs sharply between phases. The PC phase, which showed essentially no orientational order, still retains a large number of independent lineages, whereas the SSF and F phases, both of which reach high S, have collapsed to a much smaller number of surviving families, comparable in magnitude to the family counts already found sufficient to produce alignment through drift alone in Fig. 11. The D phase falls in between, with an intermediate family count despite showing no order, indicating that a reduced number of lineages is not on its own sufficient for alignment when the rotational and translational noise are too strong for any inherited signal to survive.

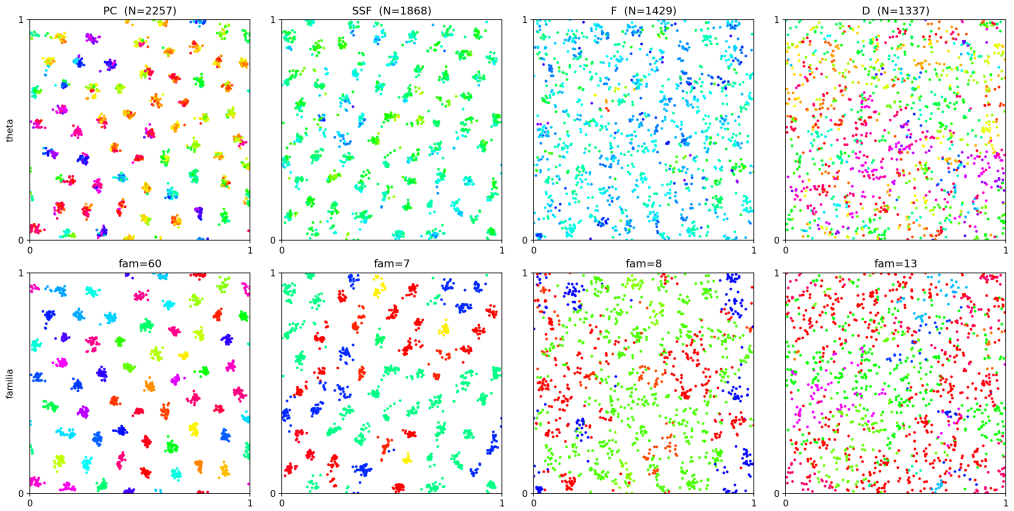

Figure 13: Final state, $t = 1000$, of the four competitive phases from Fig. 12, coloured by instantaneous direction θ, top row, and by initial family label, bottom row. The population size and surviving family count are given below each column.

This result suggests a reading of the flocking phase that differs somewhat from a purely selection based account. Rather than treating competition as the origin of orientational order, our results are more consistent with competition acting mainly as an accelerant of a coalescence process that can, and does, produce alignment on its own, given enough time and a sufficiently weak rotational mutation rate. Under competition, local crowding raises the effective rate at which lineages go extinct, so the population reaches a low family count, and with it the conditions for alignment, far sooner than it would through demographic fluctuations alone. Whether the density dependent selection mechanism

described by Takamura and Saito contributes anything beyond this accelerated coalescence, or whether it is itself best understood as a particular way of implementing faster genealogical drift, remains an open question that would benefit from a more detailed comparison between the family structure of the competitive and non-competitive models at matched values of S.

3 Conclusions

We set out to ask whether a proliferating population of self-propelled agents can develop orientational order without any explicit rule that makes neighbours align, and the answer that emerges from this work is yes, provided the population shares enough genealogical history. The passive Brownian bug model already showed that the same birth-death process responsible for the transient spatial clustering measured through $g(r)$ also drives a coalescent process, in which a single lineage eventually accounts for the whole population regardless of how fast agents diffuse. Once every agent inherits a self-propulsion direction from its parent, this same coalescence is enough to align the population on its own. For a small rotational diffusion, $S(t)$ reached 0.989 at the exact moment of family fixation, against only 0.131 for a rotational diffusion two orders of magnitude larger, so the rotational mutation rate is what decides whether the inherited direction survives long enough to matter.

Repeating this experiment across independent realizations showed that fixation to a single family is not actually required for order to appear. In most of the seeds we tested, $S(t)$ crossed 0.7 while anywhere between two and seven distinct lineages were still coexisting, each occupying its own cluster but already sharing a common average direction. Adding the density-dependent competition of Takamura and Saito reproduced their four phases and confirmed that competition offers a considerably faster route to the same kind of order, reaching high S under a rotational mutation rate that drift alone could not overcome within a comparable time. Tracking family lineages inside the competitive model showed that the two phases with high orientational order, SSF and F, had also collapsed to a family count comparable to the handful of lineages already found sufficient for alignment through drift alone, while the phases without order retained noticeably more.

In conclusion, orientational order in a proliferating self-propelled population is fundamentally a genealogical phenomenon, rooted in the same coalescence that produces spatial clustering in the passive model, and does not require a specific competitive interaction to appear.

Acknowledgments

This work was supported by the SURF@IFISC fellowship.

References

[1] M. C. Marchetti, J. F. Joanny, S. Ramaswamy, T. B. Liverpool, J. Prost, M. Rao, and R. A. Simha, *Hydrodynamics of soft active matter*, Rev. Mod. Phys. **85**, 1143 (2013).

[2] T. Vicsek, A. Czirók, E. Ben-Jacob, I. Cohen, and O. Shochet, *Novel type of phase transition in a system of self-driven particles*, Phys. Rev. Lett. **75**, 1226 (1995).

[3] W. R. Young, A. J. Roberts, and G. Stuhne, *Reproductive pair correlations and the clustering of organisms*, Nature **412**, 328 (2001).

[4] S. Takamura and N. Saito, *Spatially structured flocking in a proliferating population of self-propelled organisms without explicit alignment interactions*, Phys. Rev. Research **7**, 033299 (2025).

[5] J. F. C. Kingman, *The coalescent*, Stochastic Process. Appl. **13**, 235 (1982).

Quantum Synchronization and Associative Memories in a System of Coupled Squeezed Quantum van der Pol Oscillators

Andrea Stafferi, Advisor: Dr. Albert Cabot
Instituto de Física Interdisciplinar y Sistemas Complejos, IFISC (CSIC-UIB)
Campus Universitat de les Illes Balears, E-07122 Palma de Mallorca, Spain

Abstract

We investigate the nonequilibrium dynamics of a bipartite continuous-variable system consisting of coupled quantum van der Pol (QvdP) oscillators subject to a two-photon drive. In the single-oscillator limit, the parametric drive explicitly breaks the continuous $U(1)$ phase symmetry, generating a metastable manifold spanned by localized $\mathbb{Z}_2$ states. We analytically and numerically characterize the synchronization boundaries under coherent and dissipative coupling mechanisms. Analyzing the exact Gorini-Kossakowski-Sudarshan-Lindblad master equation, we demonstrate that continuous-variable quantum associative memories require collective dissipation to suppress anti-symmetric quantum fluctuations. This active subspace cooling stabilizes macroscopic memory patterns, whereas unitary Hamiltonian exchange is shown to be strictly limited by quantum phase diffusion.

1 Introduction

The study of nonequilibrium dynamics in open quantum systems provides a framework for extending classical synchronization phenomena into the quantum regime. A paradigmatic model for this extension is the quantum van der Pol (QvdP) oscillator, which consists of a single bosonic mode subjected to competing linear amplification and nonlinear multiphoton dissipation. The interplay of these dissipative channels generates a stable limit cycle in the quantum phase space.

When subjected to a degenerate parametric (two-photon) drive, the continuous $U(1)$ rotational symmetry of the unperturbed limit cycle is explicitly broken into a discrete $\mathbb{Z}_2$ parity symmetry. From an open quantum systems perspective, this symmetry breaking manifests dynamically as a separation of timescales within the eigenspectrum of the Liouvillian superoperator. The resulting spectral gap isolates a metastable manifold wherein the system relaxes into localized, macroscopically distinguishable pseudo-coherent states.

Recently, driven-dissipative systems exhibiting such bistability have been proposed as candidates for implementing continuous-variable Quantum Associative Memories (QAM). In this paradigm, the localized metastable states serve as classical memory patterns. Information retrieval corresponds to the dissipative relaxation of a noisy input state toward the target macroscopic attractor.

In this work, we investigate a bipartite network of coupled squeezed QvdP oscillators to evaluate the resilience and scalability of this continuous-variable encoding. In Section 2, we formulate the theoretical model governed by the Gorini-Kossakowski-Sudarshan-Lindblad (GKSL) master equation. In Section 3, we contrast the system's synchronization capabilities under coherent (Hamiltonian) and dissipative (Lindbladian) interaction topologies. We extract the semiclassical Arnold tongues and subsequently evaluate the exact quantum dynamics. We show that while unitary exchange induces level repulsion and phase diffusion, engineered collective dissipation acts as a thermodynamic sink, actively cooling the relative-phase subspace and stabilizing the macroscopic associative memory.

2 Theoretical Model and Symmetries

We consider a bipartite continuous-variable system operating in the tensor product Hilbert space $\mathcal{H} = \mathcal{H}_1 \otimes \mathcal{H}_2$. Each subsystem is modeled as a bosonic mode characterized by the annihilation

and creation operators $\hat{a}_j$ and $\hat{a}_j^\dagger$, satisfying the canonical commutation relation $[\hat{a}_i, \hat{a}_j^\dagger] = \delta_{ij}$ for $i, j \in \{1, 2\}$.

2.1 Single Oscillator Dynamics

In a frame rotating at half the external driving frequency, the coherent unitary dynamics of the j-th oscillator is governed by the Hamiltonian

$$\hat{H}_j = \Delta \hat{a}_j^\dagger \hat{a}_j + i\frac{\eta}{2}\left(\hat{a}_j^{\dagger 2} - \hat{a}_j^2\right), \tag{2.1}$$

where Δ is the detuning and $\eta \in \mathbb{R}$ defines the strength of the two-photon parametric drive. The non-unitary energy exchanges are formulated under the Born-Markov and secular approximations via standard Lindblad dissipators, defined for a generic jump operator $\hat{L}$ as $\mathcal{D}[\hat{L}]\hat{\rho} = \hat{L}\hat{\rho}\hat{L}^\dagger - \frac{1}{2}\{\hat{L}^\dagger\hat{L}, \hat{\rho}\}$.

The local dissipative dynamics are driven by a linear single-photon pumping rate $\gamma_1 > 0$ and a nonlinear two-photon absorption rate $\gamma_2 > 0$. The resulting local Liouvillian superoperator is

$$\mathcal{L}_{local}^{(j)}\hat{\rho} = -i[\hat{H}_j, \hat{\rho}] + \frac{\gamma_1}{2}\mathcal{D}[\hat{a}_j^\dagger]\hat{\rho} + \frac{\gamma_2}{2}\mathcal{D}[\hat{a}_j^2]\hat{\rho}. \tag{2.2}$$

The competition between γ_1 and γ_2 induces a dissipative limit-cycle structure, which becomes bistable under the influence of the symmetry-breaking term η.

2.2 Bipartite Network and Coupling Topologies

The global non-unitary dynamics of the composite density matrix $\hat{\rho}$ is governed by the full master equation

$$\partial_t\hat{\rho} = \mathcal{L}\hat{\rho} = \sum_{j=1,2}\mathcal{L}_{local}^{(j)}\hat{\rho} + \mathcal{L}_{couple}\hat{\rho}. \tag{2.3}$$

To evaluate the stability of quantum entrainment, we define two distinct interaction topologies. The first is a coherent interaction modeled by a tight-binding Hamiltonian

$$\hat{H}_{int} = J\left(\hat{a}_1^\dagger\hat{a}_2 + \hat{a}_1\hat{a}_2^\dagger\right), \tag{2.4}$$

where J is the coherent exchange strength. This mechanism enforces $\mathcal{L}_{couple}\hat{\rho} = -i[\hat{H}_{int}, \hat{\rho}]$. Alternatively, we implement an irreversible dissipative coupling channel via the collective jump operator

$$\mathcal{L}_{couple}\hat{\rho} = \frac{\kappa}{2}\mathcal{D}[\hat{a}_1 - \hat{a}_2]\hat{\rho}, \tag{2.5}$$

where $\kappa \geq 0$ quantifies the strength of collective dissipation.

2.3 Analytical Normal-Mode Decomposition

The physical mechanism differentiating these interaction topologies is analytically isolated by transforming the local basis into collective bosonic normal modes. We define the symmetric ($\hat{b}_+$) and anti-symmetric ($\hat{b}_-$) supermodes as

$$\hat{b}_+ = \frac{\hat{a}_1 + \hat{a}_2}{\sqrt{2}}, \quad \hat{b}_- = \frac{\hat{a}_1 - \hat{a}_2}{\sqrt{2}}, \tag{2.6}$$

which strictly preserve the canonical bosonic algebra $[\hat{b}_\mu, \hat{b}_\nu^\dagger] = \delta_{\mu\nu}$.

Applying this transformation to the collective dissipative jump operator yields $\hat{a}_1 - \hat{a}_2 = \sqrt{2}\hat{b}_-$. Utilizing the homogeneity property of the dissipator, $\mathcal{D}[c\hat{L}] = |c|^2\mathcal{D}[\hat{L}]$, the environmental coupling takes the strictly diagonal form:

$$\mathcal{L}_{couple}\hat{\rho} = \kappa\mathcal{D}[\hat{b}_-]\hat{\rho}. \tag{2.7}$$

Equation (2.7) proves that the original non-local environmental coupling acts as an irreversible local damping channel applied exclusively to the anti-symmetric collective mode. The symmetric mode $\hat{b}_+$ is completely absent from the dissipator and is therefore decoupled from the collective reservoir. By evaluating the Heisenberg equation of motion generated by this dissipator, the expectation value of the relative coordinate obeys $\partial_t\langle\hat{b}_-\rangle = -(\kappa/2)\langle\hat{b}_-\rangle$, demonstrating that synchronization ($\langle\hat{a}_1\rangle = \langle\hat{a}_2\rangle$) occurs via the active, exponential extraction of anti-symmetric fluctuations.

2.4 Spectral Theory of the Liouvillian Superoperator

To analyze both the asymptotic stationary configurations and the transient relaxation pathways of the bipartite driven-dissipative network, we utilize the spectral decomposition of the Liouvillian superoperator $\mathcal{L}$. Since $\mathcal{L}$ is a non-Hermitian operator mapping density matrices to density matrices, its right eigenmatrices $\hat{\rho}_k$ and left eigenmatrices $\hat{\sigma}_k$ are distinct and satisfy the respective eigenvalue equations:

$$\mathcal{L}\hat{\rho}_k = \lambda_k \hat{\rho}_k, \tag{2.8}$$

$$\mathcal{L}^\dagger \hat{\sigma}_k = \lambda_k^* \hat{\sigma}_k, \tag{2.9}$$

where $\lambda_k = -\Gamma_k + i\nu_k$ denote the complex eigenvalues. The real parameter $\Gamma_k \geq 0$ corresponds to the irreversible decay rate of the k-th mode, while $\nu_k \in \mathbb{R}$ represents its coherent coherent oscillation frequency. The completely positive and trace-preserving (CPTP) structure of the Lindblad map guarantees that $\mathrm{Re}(\lambda_k) \leq 0$.

Assuming a diagonalizable supermatrix structure away from exceptional singularities, the sets of left and right eigenmatrices satisfy the biorthogonality relation with respect to the Hilbert-Schmidt inner product:

$$\mathrm{Tr}\left[\hat{\sigma}_j^\dagger \hat{\rho}_k\right] = \delta_{jk}. \tag{2.10}$$

The existence of at least one stationary steady state $\hat{\rho}_{ss}$ associated with the zero eigenvalue $\lambda_0 = 0$ is mathematically guaranteed for any finite-dimensional truncation. Trace preservation implies that the corresponding left eigenmatrix is identical to the identity operator, $\hat{\sigma}_0 = \mathbb{I}$. Consequently, the exact time evolution of the composite system from an arbitrary initial state $\hat{\rho}(0)$ is given by the spectral expansion:

$$\hat{\rho}(t) = \hat{\rho}_{ss} + \sum_{k\geq 1} c_k \hat{\rho}_k e^{-\Gamma_k t} e^{i\nu_k t}, \tag{2.11}$$

where the projection coefficients are strictly defined as $c_k = \mathrm{Tr}[\hat{\sigma}_k^\dagger \hat{\rho}(0)]$. As $t \to \infty$, all excited modes characterized by $\Gamma_k > 0$ decay exponentially, forcing the system into the unique steady state $\hat{\rho}_{ss}$.

2.5 Metastability and Parity Superselection Rules

Symmetry breaking and long-lived transient states are formalized by the concept of quantum metastability. This regime occurs when a pronounced spectral gap isolates the first excited decay rate Γ_1 from the remaining bulk relaxation spectrum:

$$\frac{\Gamma_1}{\Gamma_2} \ll 1. \tag{2.12}$$

For intermediate timescales within the window $\Gamma_2^{-1} \ll t \ll \Gamma_1^{-1}$, all higher-order modes ($k \geq 2$) vanish, restricting the state evolution to the effective low-dimensional metastable manifold:

$$\hat{\rho}(t) \approx \hat{\rho}_{ss} + c_1 \hat{\rho}_1 e^{-\Gamma_1 t}. \tag{2.13}$$

The underlying physical structure of the slow mode $\hat{\rho}_1$ is constrained by the discrete symmetries of the global Liouvillian. We introduce the unitary parity operator $\hat{\Pi} = \exp\left[i\pi(\hat{a}_1^\dagger \hat{a}_1 + \hat{a}_2^\dagger \hat{a}_2)\right]$, which performs a π-phase space rotation across both bosonic modes. The corresponding parity superoperator $\mathcal{Z}_2$ is defined by its action on an operator $\hat{A}$ as $\mathcal{Z}_2\hat{A} = \hat{\Pi}\hat{A}\hat{\Pi}^\dagger$. Because the global generator commutes with this transformation, $[\mathcal{L}, \mathcal{Z}_2] = 0$, the Liouvillian supermatrix block-diagonalizes into symmetric ($\mathcal{Z}_2 = +1$) and anti-symmetric ($\mathcal{Z}_2 = -1$) sectors.

The steady state $\hat{\rho}_{ss}$ resides within the symmetric sector, satisfying $\mathcal{Z}_2\hat{\rho}_{ss} = \hat{\rho}_{ss}$. Conversely, the dominant excited mode $\hat{\rho}_1$ belongs to the anti-symmetric sector, such that $\mathcal{Z}_2\hat{\rho}_1 = -\hat{\rho}_1$. By evaluating the cyclic properties of the trace, we obtain:

$$\mathrm{Tr}[\hat{\rho}_1] = \mathrm{Tr}[\hat{\Pi}^\dagger\hat{\Pi}\hat{\rho}_1] = \mathrm{Tr}[\hat{\Pi}\hat{\rho}_1\hat{\Pi}^\dagger] = \mathrm{Tr}[\mathcal{Z}_2\hat{\rho}_1] = -\mathrm{Tr}[\hat{\rho}_1], \tag{2.14}$$

which enforces $\mathrm{Tr}[\hat{\rho}_1] = 0$. The traceless nature of the slow mode ensures that the Extreme Metastable States (EMS), defined as $\hat{\mu}_{1,2} = \hat{\rho}_{ss} \pm \hat{\rho}_1$, are normalized physical density matrices. These states

explicitly break the discrete $\mathbb{Z}_2$ parity symmetry, localizing in opposite phase-space quadrants to act as the macroscopically distinguishable attractors of the network.

2.6 Phase-Space Formalism and the Exact Wigner-Moyal Expansion

To evaluate the quantum-to-classical crossover, the abstract master equation is projected onto a continuous phase space via the Wigner quasi-probability distribution $W(\alpha_1, \alpha_1^*, \alpha_2, \alpha_2^*)$. For a generic single-mode density operator, the projection is given by the partial Fourier transform of the symmetrically ordered characteristic function:

$$\chi_W(\lambda, \lambda^*) = \mathrm{Tr}\left[\hat{\rho}\exp\left(\lambda\hat{a}^\dagger - \lambda^*\hat{a}\right)\right], \tag{2.15}$$

$$W(\alpha, \alpha^*) = \frac{1}{\pi^2}\int\int d^2\lambda \exp(\alpha\lambda^* - \alpha^*\lambda)\chi_W(\lambda, \lambda^*). \tag{2.16}$$

The mapping of operator multiplication onto phase-space differential operators is governed by the Weyl correspondence rules:

$$\hat{a}\hat{\rho} \leftrightarrow \left(\alpha + \frac{1}{2}\frac{\partial}{\partial\alpha^*}\right)W(\alpha, \alpha^*), \quad \hat{\rho}\hat{a} \leftrightarrow \left(\alpha - \frac{1}{2}\frac{\partial}{\partial\alpha^*}\right)W(\alpha, \alpha^*), \tag{2.17}$$

$$\hat{a}^\dagger\hat{\rho} \leftrightarrow \left(\alpha^* - \frac{1}{2}\frac{\partial}{\partial\alpha}\right)W(\alpha, \alpha^*), \quad \hat{\rho}\hat{a}^\dagger \leftrightarrow \left(\alpha^* + \frac{1}{2}\frac{\partial}{\partial\alpha}\right)W(\alpha, \alpha^*). \tag{2.18}$$

Applying Eqs. (2.17) and (2.18) to the nonlinear two-photon absorption dissipator $\mathcal{D}[\hat{a}^2]\hat{\rho}$ requires expanding the non-commutative operator products up to the fourth order. The exact Wigner-Moyal expansion for this nonlinear loss term evaluates to:

$$\begin{aligned}\mathcal{D}[\hat{a}^2]W = &\left[\frac{\partial}{\partial\alpha}\left(2\alpha|\alpha|^2\right) + \frac{\partial}{\partial\alpha^*}\left(2\alpha^*|\alpha|^2\right)\right]W \\ &+ \frac{\partial^2}{\partial\alpha\partial\alpha^*}\left(4|\alpha|^2 - 1\right)W + \frac{1}{2}\left(\frac{\partial^2}{\partial\alpha^2}\alpha^2 + \frac{\partial^2}{\partial\alpha^{*2}}\alpha^{*2}\right)W \\ &+ \left[\frac{\partial^3}{\partial\alpha^2\partial\alpha^*}\alpha + \frac{\partial^3}{\partial\alpha\partial\alpha^{*2}}\alpha^*\right]W + \frac{1}{4}\frac{\partial^4}{\partial\alpha^2\partial\alpha^{*2}}W.\end{aligned} \tag{2.19}$$

The first line of Eq. (2.19) defines the classical nonlinear deterministic drift. The second line encapsulates the second-order diffusion terms representing quantum back-action noise. The third line contains third- and fourth-order derivatives ($\mathcal{O}(\partial^3), \mathcal{O}(\partial^4)$). According to Pawula's theorem, these higher-order differential terms are responsible for the manifestation of non-classical Wigner negativity, necessitating the exact numerical diagonalization methods utilized herein.

2.7 Fock-Basis Algebraic Structure and Adiabatic Elimination

The matrix representation of the Liouvillian superoperator is constructed by projecting the master equation onto the infinite-dimensional bosonic Fock basis $\{|n\rangle\}_{n=0}^{\infty}$. Expanding the density matrix as $\hat{\rho} = \sum_{m,n}\rho_{m,n}|m\rangle\langle n|$, the exact transition elements for a single squeezed QvdP oscillator evaluate to:

$$\begin{aligned}\langle m|\mathcal{L}\hat{\rho}|n\rangle = &-i\Delta(m-n)\rho_{m,n} \\ &+ \eta\Big[\sqrt{(m+1)(m+2)}\rho_{m+2,n} - \sqrt{m(m-1)}\rho_{m-2,n} \\ &\quad - \sqrt{(n+1)(n+2)}\rho_{m,n+2} + \sqrt{n(n-1)}\rho_{m,n-2}\Big] \\ &+ \frac{\gamma_1}{2}\Big[2\sqrt{mn}\rho_{m-1,n-1} - (m+n+2)\rho_{m,n}\Big] \\ &+ \frac{\gamma_2}{2}\Big[2\sqrt{(m+1)(m+2)(n+1)(n+2)}\rho_{m+2,n+2} \\ &\quad - \big[m(m-1) + n(n-1)\big]\rho_{m,n}\Big].\end{aligned} \tag{2.20}$$

The selections rules imposed by the parametric drive η couple states satisfying $\Delta m, \Delta n = \pm 2$, confirming the $\mathbb{Z}_2$ block-diagonal structure of the supermatrix.

In the deep quantum regime defined by the dissipation hierarchy $\gamma_2 \gg \gamma_1, \eta, |\Delta|$, the null space of the unperturbed Liouvillian $\mathcal{L}_0 = \frac{\gamma_2}{2}\mathcal{D}[\hat{a}^2]$ is spanned exclusively by the states lacking two-photon excitations, collapsing the operational Hilbert space to the logical subspace $\{|0\rangle, |1\rangle\}$. Treating the remaining terms as a perturbation $\mathcal{L}_1$, we project the dynamics via the Nakajima-Zwanzig technique onto the slow manifold. The second-order effective relaxation rate governing the slow anti-symmetric mode evaluates to:

$$\Gamma_1 \approx \frac{8\eta^2}{\gamma_2} - \gamma_1. \tag{2.21}$$

Equation (2.21) indicates that increasing the nonlinear damping rate γ_2 suppresses phase slips, extending the lifetime of the metastable manifold.

2.8 Microscopic Derivation of Collective Dissipation

The phenomenological collective dissipator $\kappa\mathcal{D}[\hat{a}_1 - \hat{a}_2]$ requires rigorous justification via the Born-Markov-Secular (BMS) approximation. We consider the bipartite QvdP network coupled to a common, memoryless thermal bath modeled as an infinite reservoir of harmonic oscillators, $\hat{H}_{bath} = \sum_k \omega_k \hat{b}_k^\dagger \hat{b}_k$. To engineer the anti-symmetric jump operator, the oscillators must couple to the common bath mode with opposite macroscopic phases. The interaction Hamiltonian in the dipole-approximation is:

$$\hat{H}_{int} = \sum_k g_k \left((\hat{a}_1 - \hat{a}_2)\hat{b}_k^\dagger + (\hat{a}_1^\dagger - \hat{a}_2^\dagger)\hat{b}_k \right) = \hat{c} \otimes \hat{\Gamma}^\dagger + \hat{c}^\dagger \otimes \hat{\Gamma}, \tag{2.22}$$

where g_k is the coupling strength, $\hat{c} = \hat{a}_1 - \hat{a}_2$ is the collective system operator, and $\hat{\Gamma} = \sum_k g_k \hat{b}_k$.

Moving to the interaction picture, we perform the Born approximation $\hat{\rho}_{tot}(t) \approx \hat{\rho}_S(t) \otimes \hat{\rho}_B$. Tracing over the bath yields the integro-differential Redfield equation. Imposing the Markovian limit, the Redfield tensor is governed by the two-time environmental correlation functions, proportional to the bath spectral density $J(\omega) = \sum_k |g_k|^2 \delta(\omega - \omega_k)$. Assuming a zero-temperature bath ($\bar{n} = 0$), the integration requires the Sokhotski-Plemelj theorem:

$$\int_0^\infty d\tau \, e^{\pm i(\omega_{sys} - \omega)\tau} = \pi\delta(\omega_{sys} - \omega) \pm i\mathcal{P}\left(\frac{1}{\omega_{sys} - \omega}\right). \tag{2.23}$$

The principal value ($\mathcal{P}$) generates the Lamb shift, while the delta function enforces energy conservation, defining the Markovian decay rate $\kappa = 2\pi J(\omega_{sys})$. Applying the Secular Approximation to average out fast-oscillating terms, the trace exactly reconstitutes the Lindblad form:

$$\frac{d\hat{\rho}_S}{dt} = -i[\hat{H}_{sys}, \hat{\rho}_S] + \kappa\left(\hat{c}\hat{\rho}_S\hat{c}^\dagger - \frac{1}{2}\{\hat{c}^\dagger\hat{c}, \hat{\rho}_S\}\right). \tag{2.24}$$

Substituting $\hat{c} = \hat{a}_1 - \hat{a}_2$ formally recovers the collective dissipator.

2.9 Physical Implementations

The continuous-variable architecture can be physically realized in platforms such as Circuit QED and trapped ions. In Superconducting Quantum Electrodynamics, the primary mode $\hat{a}$ represents a microwave cavity parametrically coupled to a lossy buffer mode $\hat{b}$. The two-photon nonlinear absorption $\gamma_2\mathcal{D}[\hat{a}^2]$ is engineered via a Superconducting Nonlinear Asymmetric Inductive Element (SNAIL) [5]. By breaking the inversion symmetry of the Josephson potential via an external magnetic flux Φ_{ext}, the SNAIL unlocks three-wave mixing processes:

$$\hat{H}_{3WM} = g_3\left(\hat{a}^{\dagger 2}\hat{b} + \hat{a}^2\hat{b}^\dagger\right). \tag{2.25}$$

Adiabatically eliminating the fast buffer degrees of freedom ($\kappa_b \gg g_3$) yields the effective decay rate $\gamma_2 = 4g_3^2/\kappa_b$.

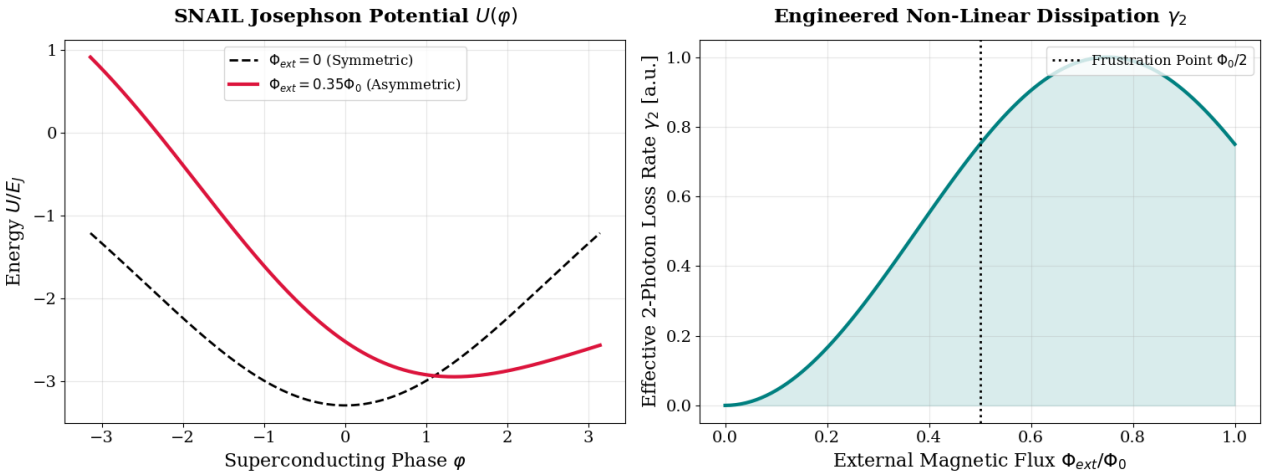

Figure 1: Hardware engineering via Circuit QED. **Left:** The Josephson potential $U(\varphi)$ of a SNAIL device. An external magnetic flux $\Phi_{ext} \neq 0$ breaks parity symmetry, enabling 3-wave mixing. **Right:** The effective non-linear dissipation rate γ_2 as a function of the applied magnetic flux.

In trapped-ion setups, the collective dissipation $\kappa\mathcal{D}[\hat{a}_1 - \hat{a}_2]$ is implemented via sympathetic cooling [6]. Two logical ions are coupled to a central auxiliary cooling ion. By matching a bichromatic laser beat-note to the anti-symmetric stretch mode ($\hat{b}_-$), the symmetric Center-of-Mass mode ($\hat{b}_+$) remains decoupled. Table 1 synthesizes the mapping of the GKSL parameters across platforms.

Mathematical Parameter	**Trapped Ions** [1]	**Circuit QED** [4]	**Optomechanics** [2]
Bosonic Mode ($\hat{a}$)	Transverse Phonon Mode	3D Microwave Cavity Field	Mechanical Nanoresonator
Squeezed Drive (η)	RF Modulated Trap	Degenerate Parametric Pump	Parametric Force Modulation
Linear Gain (γ_1)	Blue-sideband Laser	Driven 4-Wave Mixing	Blue-detuned Laser
Non-linear Loss (γ_2)	2-Phonon Red-sideband	SNAIL/ATS 3-Wave Mixing	2-Phonon Cooling
Collective Coupling (κ)	Auxiliary Ion Cooling	Dissipative Shared Resonator	Cascaded Optical Cavities

Table 1: Universal hardware taxonomy mapping the GKSL master equation parameters to their physical realizations across quantum technologies.

3 Results and Discussion

To systematically characterize the synchronization boundaries and evaluate the impact of quantum fluctuations, we first perform a semiclassical reduction of the system dynamics. Subsequently, we analyze the exact quantum regime by evaluating the Liouvillian eigenspectrum, the topological exceptional points, and the Wigner quasi-probability distributions.

3.1 Semiclassical Limit and Mean-Field Phase-Locking

The classical equations of motion are derived from the exact quantum dynamics by evaluating the adjoint Liouvillian superoperator for the annihilation operator, $\partial_t\langle\hat{a}_j\rangle = \mathrm{Tr}[\hat{a}_j\mathcal{L}\hat{\rho}]$. Applying the collective dissipative coupling $\kappa\mathcal{D}[\hat{a}_1 - \hat{a}_2]$, the unclosed operator hierarchy evaluates to:

$$\frac{d}{dt}\langle\hat{a}_1\rangle_{diss} = \frac{\kappa}{2}\langle\hat{a}_2 - \hat{a}_1\rangle. \tag{3.1}$$

In the semiclassical limit, we invoke the mean-field approximation, defining the macroscopic complex amplitude $\alpha_j \equiv \langle\hat{a}_j\rangle$. By asserting that quantum fluctuations are negligible, we factorize the third-order moments as $\langle\hat{a}_j^\dagger\hat{a}_j^2\rangle \simeq |\alpha_j|^2\alpha_j$. The composite system is then governed by a set of coupled

nonlinear ordinary differential equations:

$$\dot{\alpha}_1 = \left(\frac{\gamma_1 - \kappa}{2} - i\Delta\right)\alpha_1 - 2\eta\alpha_1^* - \gamma_2|\alpha_1|^2\alpha_1 + \frac{\kappa}{2}\alpha_2, \tag{3.2}$$

$$\dot{\alpha}_2 = \left(\frac{\gamma_1 - \kappa}{2} - i\Delta\right)\alpha_2 - 2\eta\alpha_2^* - \gamma_2|\alpha_2|^2\alpha_2 + \frac{\kappa}{2}\alpha_1. \tag{3.3}$$

To analytically define the synchronization boundaries, we perform a phase reduction by substituting the polar ansatz $\alpha_j(t) = R_j(t)e^{i\phi_j(t)}$. We assume the amplitudes adiabatically relax to the limit-cycle steady state $R_1 \approx R_2 \approx R_{LC}$. Defining the relative phase mismatch $\theta = \phi_1 - \phi_2$ and subtracting the resulting phase equations, we derive the Generalized Adler Equation for the dissipatively coupled network:

$$\dot{\theta} = [4\eta\cos(\phi_1 + \phi_2) - \kappa]\sin(\theta). \tag{3.4}$$

Absolute phase-locking requires $\dot{\theta} \to 0$. The collective dissipation κ acts strictly as a damping force on the relative phase θ, whereas the two-photon drive η modulates the stability depending on the absolute position in phase space. The system synchronizes when the effective damping coefficient satisfies $\kappa > 4\eta\cos(\phi_1 + \phi_2)$. The boundaries separating phase-locked regimes from limit-cycle dynamics define the Arnold tongues.

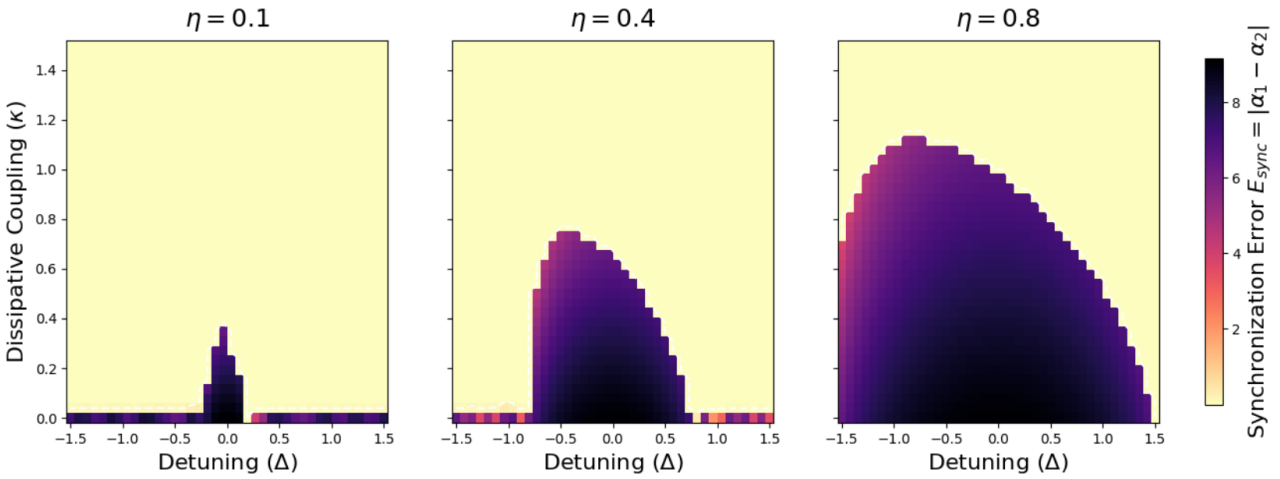

Figure 2: Semiclassical Arnold tongues under collective dissipative coupling κ for varying two-photon driving strengths η. The heatmaps display the asymptotic synchronization error $E_{sync} = \lim_{t\to\infty}|\alpha_1(t) - \alpha_2(t)|$ extracted via numerical integration of Eqs. (3.2) and (3.3). **Left:** Weak squeezing ($\eta = 0.1$). **Center:** Intermediate squeezing ($\eta = 0.4$). **Right:** Strong squeezing ($\eta = 0.8$). The dashed white contours delineate the absolute phase-locking regimes ($E_{sync} \approx 0$). Increasing the parametric drive η widens the Arnold tongues, indicating that deeper $\mathbb{Z}_2$ potential wells enhance the resilience of macroscopic entrainment against frequency detuning.

3.2 Exact Linear Stability Analysis and the SNIC Bifurcation

To evaluate the local stability of the synchronization manifold beyond the zeroth-order mean-field limit, we expand the Heisenberg-Langevin equations. We decompose the bosonic operators into a deterministic expectation value and a zero-mean quantum fluctuation operator: $\hat{a}_j(t) = \alpha_j(t) + \delta\hat{a}_j(t)$. Applying a first-order operator Taylor expansion, $(\alpha_j^* + \delta\hat{a}_j^\dagger)(\alpha_j + \delta\hat{a}_j)^2 \approx |\alpha_j|^2\alpha_j + 2|\alpha_j|^2\delta\hat{a}_j + \alpha_j^2\delta\hat{a}_j^\dagger$, we extract the linearized dynamics for the anti-symmetric macroscopic error mode $\delta\hat{b}_- = (\delta\hat{a}_1 - \delta\hat{a}_2)/\sqrt{2}$:

$$\frac{d}{dt}\delta\hat{b}_- = (\Gamma_{\text{eff}} - \kappa)\delta\hat{b}_- + \Lambda_{\text{eff}}\delta\hat{b}_-^\dagger + \hat{\mathcal{F}}_-(t). \tag{3.5}$$

Here, $\hat{\mathcal{F}}_-(t)$ is the delta-correlated Langevin noise operator. Assuming the perfectly synchronized steady state $|\alpha_{ss}|^2 = \gamma_1/(2\gamma_2)$, the local effective drift coefficients evaluate exactly to $\Gamma_{\text{eff}} = -\frac{\gamma_1}{2} - \kappa - i\Delta$ and $\Lambda_{\text{eff}} = -2\eta - \frac{\gamma_1}{2}e^{2i\phi_{ss}}$.

The non-equilibrium stability is determined by the eigenvalues of the real-valued 2×2 Jacobian tensor constructed from these coefficients. Algebraic diagonalization yields the leading Lyapunov exponent λ_+:

$$\lambda_+ = -\left(\frac{\gamma_1}{2} + \kappa\right) + \sqrt{4\eta^2 + \frac{\gamma_1^2}{4} + \gamma_1\sqrt{4\eta^2 - \Delta^2} - \Delta^2}. \tag{3.6}$$

The network is macroscopically synchronized if and only if $\mathrm{Re}(\lambda_+) < 0$. The emergence of the $\mathbb{Z}_2$ associative memory manifold from the underlying $U(1)$ limit cycle is governed by a Saddle-Node on Invariant Circle (SNIC) bifurcation.

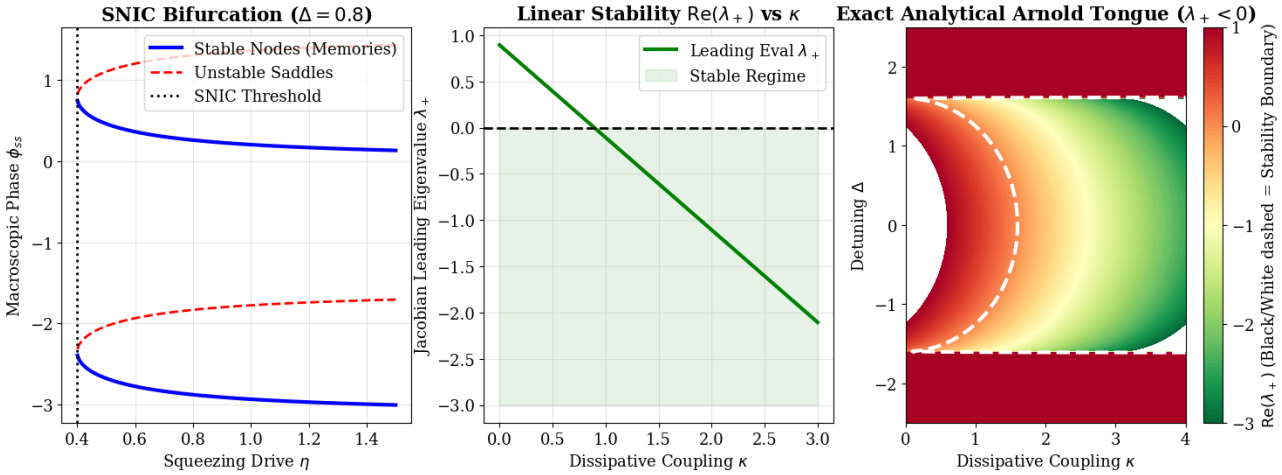

Figure 3: Exact mean-field linear stability analysis of the continuous-variable QAM. **Left:** The SNIC bifurcation branches showing the genesis of the stable memory lobes (solid blue) and the unstable saddle boundaries (dashed red) as the parametric drive η crosses the critical threshold. **Center:** The flow of the leading Jacobian eigenvalue λ_+ as a function of collective dissipation κ. The environmental coupling forces the eigenvalue across the zero-axis, achieving linear stability. **Right:** The exact analytical Arnold Tongue mapped solely via the condition $\mathrm{Re}(\lambda_+) < 0$. The dashed white contour defines the deterministic boundary separating exponential phase-locking from chaotic dephasing.

3.3 Quantum Dynamics and the Liouvillian Exceptional Point

In the deep quantum regime, absolute phase-locking is prohibited by intrinsic quantum fluctuations (Heisenberg uncertainty). Quantum synchronization is instead linked to the emergence of a metastable manifold, quantified by a massive timescale separation in the eigenspectrum of the Liouvillian supermatrix, $\Gamma_1/\Gamma_2 \ll 1$ [3].

The formation of the $\mathbb{Z}_2$ memory lobes originates from the dynamical instability of the quantum vacuum $|0\rangle\langle 0|$ under the two-photon parametric drive. In the vanishingly small amplitude limit ($\alpha \to 0$), the nonlinear two-photon absorption becomes negligible. The local dynamics are governed by the drift matrix $\mathbf{M}$:

$$\mathbf{M} = \begin{pmatrix} -\frac{\gamma_1}{2} - i\Delta & -2\eta \\ -2\eta & -\frac{\gamma_1}{2} + i\Delta \end{pmatrix}. \tag{3.7}$$

Solving the characteristic polynomial $\det(\mathbf{M} - \lambda\mathbf{I}) = 0$ yields the exact analytical expression for the linearized eigenfrequencies:

$$\lambda_\pm = -\frac{\gamma_1}{2} \pm \sqrt{4\eta^2 - \Delta^2}. \tag{3.8}$$

When $4\eta^2 < \Delta^2$, the system exhibits damped oscillations ($\lambda_\pm = -\frac{\gamma_1}{2} \pm i\omega$). At the critical point $2\eta = |\Delta|$, the square root vanishes and the eigenvalues coalesce into a single degenerate real value $\lambda_+ = \lambda_- = -\gamma_1/2$. This singularity is a second-order Liouvillian Exceptional Point (EP2), marking the topological boundary where oscillatory dynamics bifurcate into pure real exponential decay [3].

For the macroscopic metastable lobes to materialize, the vacuum state must become an unstable repeller ($\mathrm{Re}(\lambda_+) > 0$). Imposing this condition yields the fundamental parametric threshold for the

quantum associative memory:

$$\eta_{crit} = \frac{1}{2}\sqrt{\left(\frac{\gamma_1}{2}\right)^2 + \Delta^2}. \tag{3.9}$$

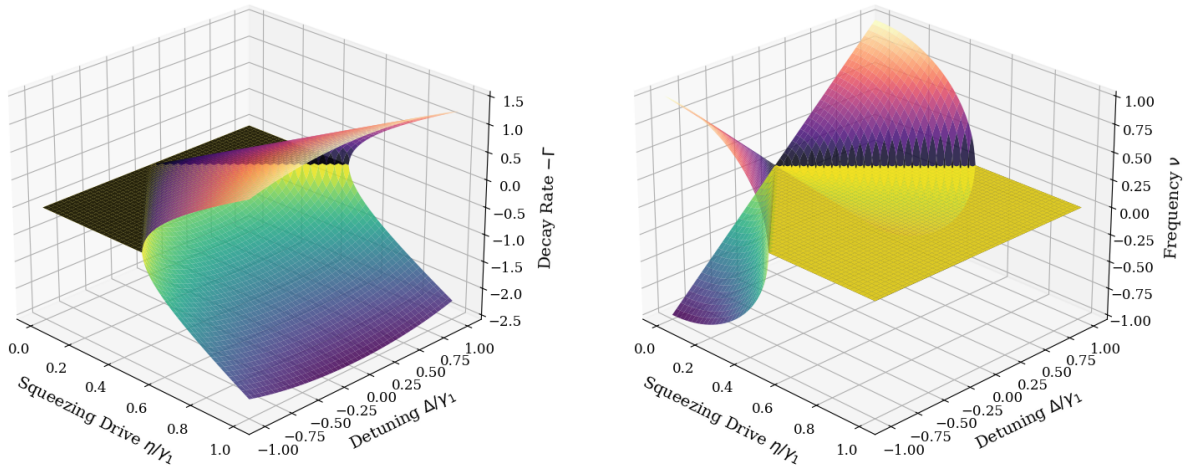

Figure 4: Three-dimensional Riemann surfaces illustrating the topological Liouvillian Exceptional Point (EP) of the squeezed QvdP oscillator. **Left:** The real part of the spectrum (decay rates, $\mathrm{Re}(\lambda)$). Beyond the EP branch cut ($2\eta > |\Delta|$), the eigenvalues split, giving birth to the metastable mode $\Gamma_1 \to 0$ (upper surface) and the fast-decaying mode Γ_2 (lower surface). **Right:** The imaginary part of the spectrum (frequencies, $\mathrm{Im}(\lambda)$). Below the EP ($2\eta < |\Delta|$), the modes exhibit distinct conjugate oscillatory frequencies, which perfectly coalesce to zero exactly at the EP singularity.

The topological structure of the Liouvillian spectrum defines the dynamical fingerprint of the open quantum system. As illustrated in Fig. 5, coherent Hamiltonian exchange (J) intrinsically mixes the eigenmodes, triggering severe level repulsion along the imaginary axis [2]. This obliteration of the spectral gap implies that macroscopic variables undergo quasi-periodic beating. Conversely, the collective non-local dissipator $\hat{L}_{diss} = \hat{a}_1 - \hat{a}_2$ actively accelerates the decay of anti-symmetric bulk excitations while preserving the symmetric metastable mode near the origin ($\lambda_0 = 0$), effectively widening the spectral gap.

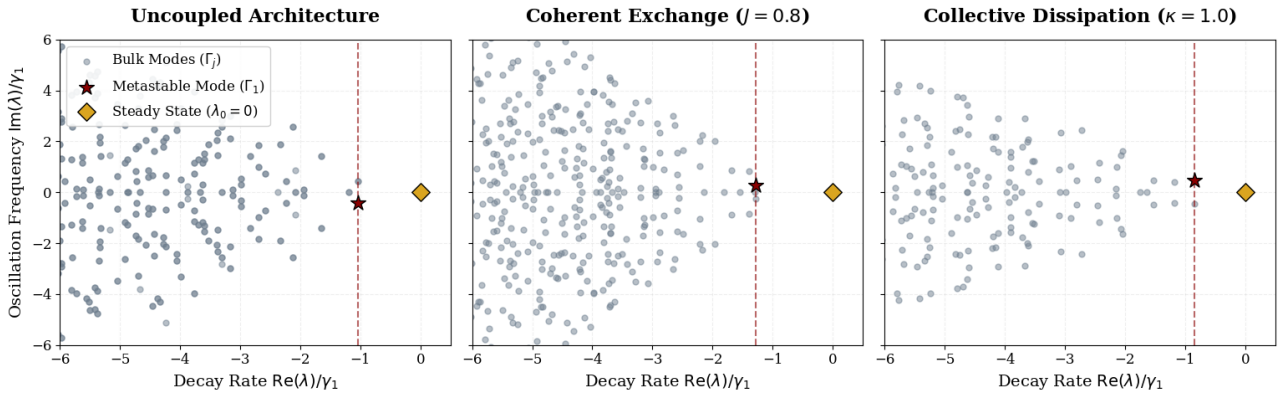

Figure 5: Topological structure of the Liouvillian complex eigenspectrum ($\mathrm{Re}(\lambda)$ vs $\mathrm{Im}(\lambda)$). The golden diamond denotes the invariant steady state ($\lambda_0 = 0$), while the dark red star highlights the dominant metastable mode (λ_1). **Left:** Uncoupled architecture displaying a clear macroscopic gap. **Center:** Coherent exchange ($J = 0.8$) disperses the eigenvalues along the imaginary axis, destroying the spectral gap. **Right:** Collective dissipation ($\kappa = 1.0$) accelerates the decay of anti-symmetric excitations (pushing the grey cloud deeper into the negative real half-plane) while preserving the metastable mode, widening the spectral gap.

3.4 Quantum Phase Diffusion and Wigner Representation

To evaluate how intrinsic quantum fluctuations affect the structural stability of the synchronized states, we map the exact quantum steady state to the continuous-variable phase space utilizing the Wigner quasi-probability distribution $W(\alpha, \alpha^*)$.

Applying the exact Weyl correspondence rules to the GKSL master equation, we extract the drift vector $A(\alpha)$ and the diffusion tensor $\boldsymbol{D}(\alpha, \alpha^*)$. Truncating to second-order derivatives, the time evolution is governed by the generalized quantum Fokker-Planck equation:

$$\frac{\partial W}{\partial t} = \left[-\frac{\partial}{\partial \alpha} A_\alpha - \frac{\partial}{\partial \alpha^*} A_{\alpha^*} + \frac{\partial^2}{\partial \alpha \partial \alpha^*} D_{\alpha\alpha^*} \right] W(\alpha, \alpha^*). \tag{3.10}$$

By transitioning to polar coordinates ($\alpha = re^{i\phi}$) and evaluating the total diffusion tensor at the deterministic limit-cycle radius $R_{LC} \approx \sqrt{\gamma_1/2\gamma_2}$, we extract the exact scaling of the quantum phase diffusion:

$$D_{\phi\phi} = \frac{1}{4R_{LC}^2} \left(\gamma_1 + 2\gamma_2 R_{LC}^2 \right) \approx \gamma_2. \tag{3.11}$$

This analytical derivation demonstrates that even if the system perfectly reaches its macroscopic limit cycle, the fundamental phase diffusion rate $D_{\phi\phi}$ remains strictly bounded from below by the non-linear absorption rate $\gamma_2 > 0$. Consequently, the variance of the phase grows linearly with time ($\langle \Delta\phi^2 \rangle \propto D_{\phi\phi} t$), inevitably inducing the $\mathbb{Z}_2$ phase-slips that erase encoded memory patterns.

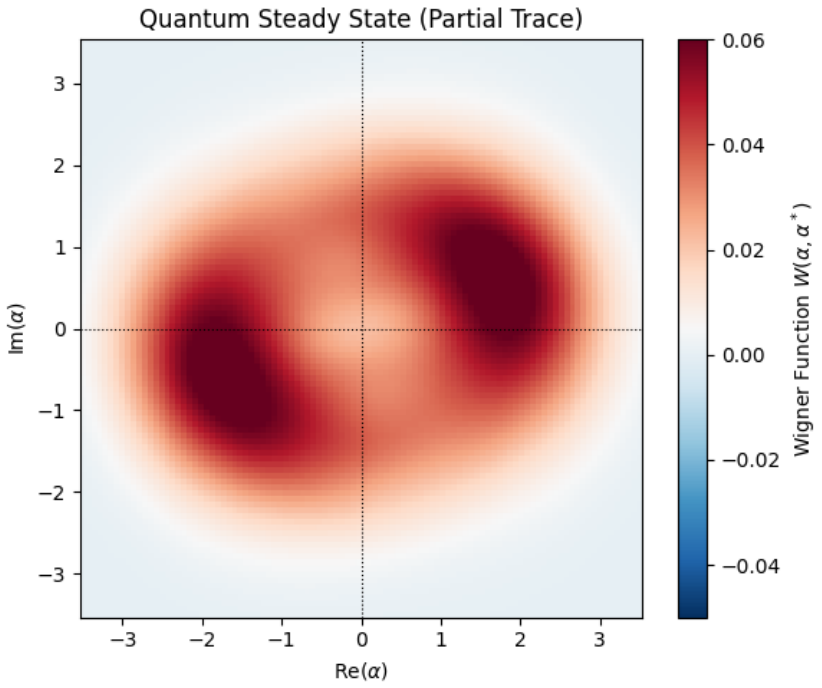

Figure 6: Wigner quasi-probability distribution $W(\alpha, \alpha^*)$ of the exact quantum steady state for the first oscillator, obtained via partial trace over the composite system ($N = 8$, $\Delta = 0.5$, $\eta = 0.4$, $J = 0.2$). The discrete $\mathbb{Z}_2$ symmetry breaking is explicitly manifest in the two symmetric localized lobes (red). Crucially, the distribution is strictly positive, lacking the characteristic Wigner negativity (blue interference fringes) of pure Schrödinger cat states. This physically proves that the intrinsic quantum noise causes complete decoherence between the lobes at $t \to \infty$.

The relative dominance of intrinsic quantum fluctuations over the deterministic macroscopic dynamics is explicitly parameterized by the dimensionless ratio γ_2/γ_1. The numerical integration presented in Fig. 7 illustrates this quantum-to-classical crossover. For large limit-cycle radii (semiclassical regime), the steady state manifests as a heavily modulated limit cycle exhibiting macroscopic quantum interference fringes [1]. In the deep quantum regime, severe quantum phase diffusion dominates, collapsing the radius and transforming the steady state into a single, diffuse, phase-smeared distribution.

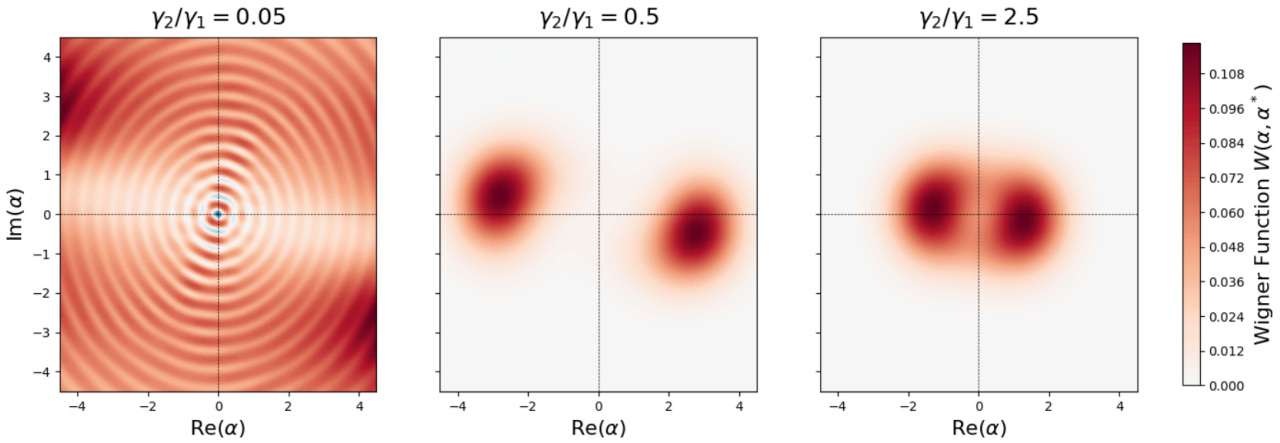

Figure 7: Quantum-to-classical crossover of the steady-state Wigner distribution $W(\alpha, \alpha^*)$ ($N \in [10, 30]$, $\Delta = 0.5, \eta = 0.8$). **Left:** Semiclassical regime ($\gamma_2/\gamma_1 = 0.05$). The large limit cycle remains unbroken, exhibiting intense macroscopic quantum interference fringes. **Center:** Intermediate regime ($\gamma_2/\gamma_1 = 0.5$). Optimal $\mathbb{Z}_2$ symmetry breaking, yielding two distinct, robust macroscopic lobes. **Right:** Deep quantum regime ($\gamma_2/\gamma_1 = 2.5$). Severe quantum phase diffusion collapses the radius, merging the lobes toward the phase-space origin and destroying macroscopic distinguishability.

3.5 Bipartite Quantum Phase Distribution and Synchronization Metric

To generalize the concept of phase-locking to the deep quantum regime, where continuous trajectories are prohibited by the Heisenberg uncertainty principle, we transition from classical angles to a continuous-variable quantum phase distribution, $\mathcal{P}(\theta_1, \theta_2)$. The phase probability density is reconstructed from the positive-definite Husimi Q-function by analytically integrating over the radial amplitude coordinates.

For a bipartite density matrix expanded in the Fock basis, $\hat{\rho} = \sum_{n_i, m_i} \rho_{n_1 n_2}^{m_1 m_2} |n_1, n_2\rangle\langle m_1, m_2|$, the joint Husimi Q-function is defined via projection onto two-mode coherent states:

$$Q(\alpha_1, \alpha_2) = \frac{1}{\pi^2} e^{-|\alpha_1|^2 - |\alpha_2|^2} \sum_{n_1, n_2=0}^{\infty} \sum_{m_1, m_2=0}^{\infty} \rho_{n_1 n_2}^{m_1 m_2} \frac{(\alpha_1^*)^{n_1} (\alpha_2^*)^{n_2} \alpha_1^{m_1} \alpha_2^{m_2}}{\sqrt{n_1! n_2! m_1! m_2!}}. \tag{3.12}$$

Mapping the complex amplitudes to polar coordinates, $\alpha_j = r_j e^{i\theta_j}$, the exact continuous-variable joint phase distribution $\mathcal{P}(\theta_1, \theta_2)$ is obtained by marginalizing over the infinite radial domains:

$$\mathcal{P}(\theta_1, \theta_2) = \int_0^{\infty} \int_0^{\infty} Q(r_1 e^{i\theta_1}, r_2 e^{i\theta_2}) r_1 r_2 \, dr_1 dr_2. \tag{3.13}$$

Evaluating the integrals analytically yields the closed-form expression for the phase distribution:

$$\mathcal{P}(\theta_1, \theta_2) = \frac{1}{4\pi^2} \sum_{\{n,m\}} \rho_{n_1 n_2}^{m_1 m_2} \frac{\Gamma\left(\frac{n_1+m_1}{2} + 1\right) \Gamma\left(\frac{n_2+m_2}{2} + 1\right)}{\sqrt{n_1! n_2! m_1! m_2!}} e^{i(m_1 - n_1)\theta_1 + i(m_2 - n_2)\theta_2}. \tag{3.14}$$

This exact analytical formulation elegantly bridges the discrete quantum nature of the Fock-space coherences with the continuous macroscopic concept of phase synchronization. Visualizing this joint distribution allows for the rigorous identification of phase-entrainment, which physically manifests as a strict macroscopic localization of probability mass along the synchronization diagonal $\theta_1 = \theta_2$. By introducing the non-local collective dissipator, the system dynamically purges anti-symmetric excitations, effectively suppressing the probability landscape across all off-diagonal coordinates. Unlike classical noiseless networks where phase-locking produces infinitely sharp deterministic trajectories, the intrinsic zero-point fluctuations of the dissipative channels inherently smear this quantum distribution. Consequently, the synchronized manifold emerges as a robust topographical ridge with a finite, noise-bounded width, explicitly demonstrating the fundamental thermodynamic tension between environment-induced macroscopic entrainment and local quantum phase diffusion.

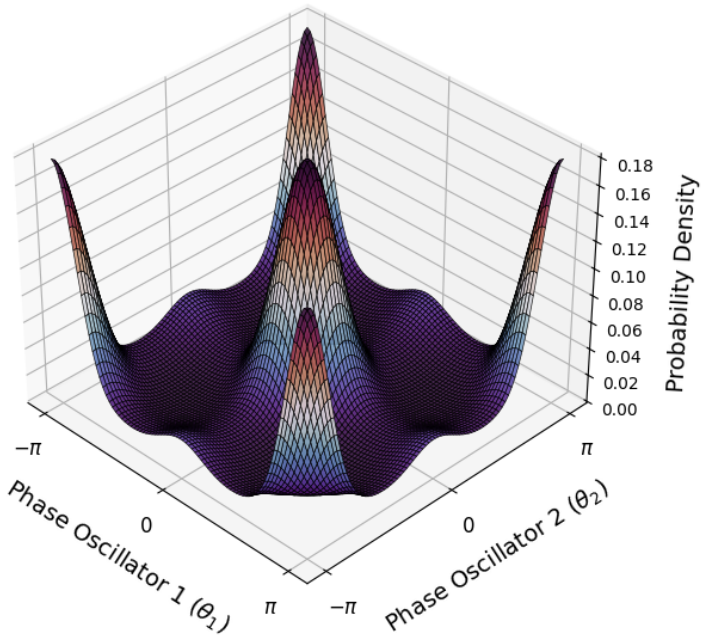

Figure 8: Topological landscape of the Bipartite Quantum Phase Distribution $\mathcal{P}(\theta_1, \theta_2)$ under collective dissipative coupling ($N = 8, \eta = 0.6, \kappa = 1.5$). The suppression of probability mass at the off-diagonal coordinates $(0, \pm\pi)$ and $(\pm\pi, 0)$ indicates strict in-phase entrainment, isolating the memory states along the synchronization diagonal $\theta_1 = \theta_2$.

To provide a quantitative metric of macroscopic phase alignment, we evaluate the Quantum Synchronization Order Parameter, $\mathcal{R}_q$, defined through the normalized first-order cross-correlation function of the steady state $\hat{\rho}_{ss}$:

$$\mathcal{R}_q = \frac{\left|\langle \hat{a}_1^\dagger \hat{a}_2 \rangle\right|}{\sqrt{\langle \hat{a}_1^\dagger \hat{a}_1 \rangle \langle \hat{a}_2^\dagger \hat{a}_2 \rangle}} = \frac{\left|\mathrm{Tr}(\hat{a}_1^\dagger \hat{a}_2 \hat{\rho}_{ss})\right|}{\sqrt{\mathrm{Tr}(\hat{n}_1 \hat{\rho}_{ss}) \mathrm{Tr}(\hat{n}_2 \hat{\rho}_{ss})}}. \tag{3.15}$$

This metric satisfies $0 \leq \mathcal{R}_q \leq 1$, where $\mathcal{R}_q \to 1$ indicates absolute phase-locking.

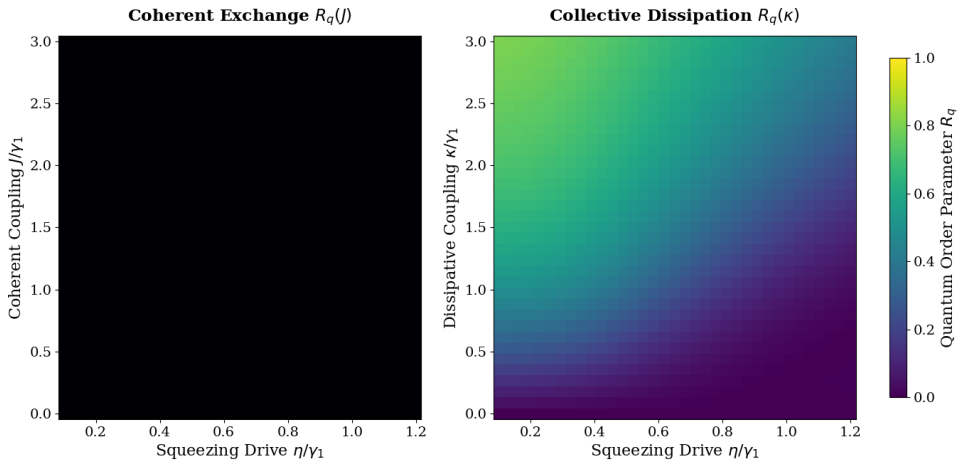

Figure 9: Phase diagrams of the Quantum Synchronization Order Parameter $\mathcal{R}_q$ ($\Delta = 0.5$). **Left:** Under coherent exchange (J), the cross-correlation averages to zero, leading to absolute phase collapse. **Right:** Under collective dissipation (κ), the environment extracts out-of-phase entropy, causing the order parameter to converge to the fundamental quantum limit ($\mathcal{R}_q \to 1$).

3.6 Quantum Correlations and Logarithmic Negativity

To rigorously distinguish macroscopic synchronization from genuine quantum non-separability, we evaluate the entanglement generated within the metastable manifold. We define the vector of Hermitian quadrature operators $\hat{\mathbf{R}} = (\hat{x}_1, \hat{p}_1, \hat{x}_2, \hat{p}_2)^T$. The fundamental commutation structure is encapsulated by the symplectic matrix $\mathbf{\Omega}$, where $[\hat{R}_k, \hat{R}_l] = i\Omega_{kl}$.

The bipartite quantum fluctuations are encoded in the 4×4 real, symmetric covariance matrix $\boldsymbol{V}_{kl} = \frac{1}{2}\langle\{\Delta\hat{R}_k, \Delta\hat{R}_l\}\rangle$. Within the transient timescale $\tau_{ret} \ll t \ll \tau_{tun}$, the local phase-space curvature induced by γ_2 strictly bounds the fluctuations, allowing the localized metastable states to be approximated as effective Gaussian states.

The necessary and sufficient condition for continuous-variable entanglement is dictated by the Positive Partial Transpose (PPT) criterion. The partial transposition corresponds to a localized momentum flip, $\hat{p}_2 \to -\hat{p}_2$. The partially transposed covariance matrix is $\tilde{\boldsymbol{V}} = \mathbf{\Lambda}\boldsymbol{V}\mathbf{\Lambda}$, with $\mathbf{\Lambda} = \mathrm{diag}(1, 1, 1, -1)$. The lowest symplectic eigenvalue of $\tilde{\boldsymbol{V}}$ evaluates to:

$$\tilde{\nu}_- = \sqrt{\frac{\Delta(\tilde{\boldsymbol{V}}) - \sqrt{\Delta(\tilde{\boldsymbol{V}})^2 - 4\det \boldsymbol{V}}}{2}}, \tag{3.16}$$

where $\Delta(\boldsymbol{V})$ is a symplectic invariant. If $\tilde{\nu}_- < 1/2$, the state is genuinely entangled, quantified by the Logarithmic Negativity $E_N = \max(0, -\ln(2\tilde{\nu}_-))$. Evaluating E_N on the exact steady-state density matrix $\hat{\rho}_{ss}$ yields $E_N \equiv 0$. The macroscopic EMS forming the memory lobes are strongly localized pseudo-coherent states $|\pm\alpha_0, \pm\alpha_0\rangle$, meaning their statistical mixture is strictly separable.

Consequently, to identify synchronization without relying on classical phase-space trajectories, we evaluate the Von Neumann Quantum Mutual Information $\mathcal{I}(1:2) = S(\hat{\rho}_1) + S(\hat{\rho}_2) - S(\hat{\rho}_{12})$.

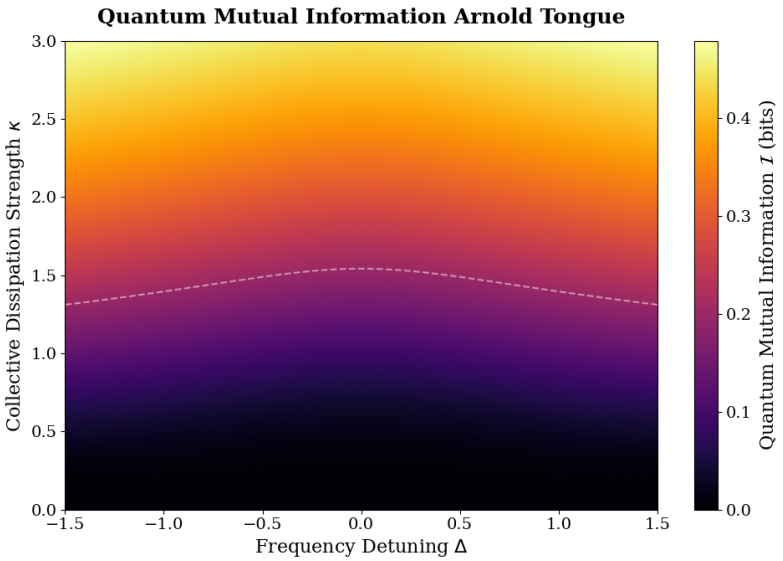

Figure 10: The Quantum Mutual Information Arnold Tongue, mapping $\mathcal{I}(1:2)$ across the parameter space ($N = 5, \eta = 0.4, \gamma_1 = 1.0, \gamma_2 = 0.5$). The bright central region confirms that collective dissipation distills a highly correlated Non-Equilibrium Steady State (NESS). The strictly separable nature of the state confirms that this synchronized manifold relies on robust statistical correlation rather than fragile bipartite entanglement.

3.7 Subspace Cooling and 3D Phase-Space Tomography

To analytically prove that collective dissipation acts as a thermodynamic sink, we map the global quantum state $\hat{\rho}$ into the orthogonal collective modes via a unitary beam-splitter transformation $\hat{U}_{BS} = \exp\left[\frac{\pi}{4}(\hat{a}_1^\dagger\hat{a}_2 - \hat{a}_1\hat{a}_2^\dagger)\right]$. Under this transformation, the coherent exchange Hamiltonian evaluates

to $\hat{H}_{int} = J(\hat{b}_+^\dagger \hat{b}_+ - \hat{b}_-^\dagger \hat{b}_-)$. This interaction induces level repulsion between the symmetric and anti-symmetric modes but fails to dissipate energy.

Conversely, the collective dissipative jump operator transforms to $2\kappa\mathcal{D}[\hat{b}_-]\hat{\rho}$. The environment exclusively targets the anti-symmetric supermode ($\hat{b}_-$), cooling it to the absolute quantum vacuum ($\hat{\rho}_- \to |0\rangle\langle 0|$) at an enhanced rate 2κ. We extract the exact steady-state population of the error mode via the Quantum Langevin Equations:

$$\langle \hat{b}_-^\dagger \hat{b}_- \rangle_{ss} = \frac{1}{2\pi} \int_{-\infty}^{\infty} |\chi_-(\omega)|^2 \langle \hat{\mathcal{F}}_{in}^\dagger(\omega) \hat{\mathcal{F}}_{in}(\omega) \rangle d\omega \equiv 0, \tag{3.17}$$

where $\chi_-(\omega) = (\kappa - i\omega)^{-1}$ is the susceptibility function.

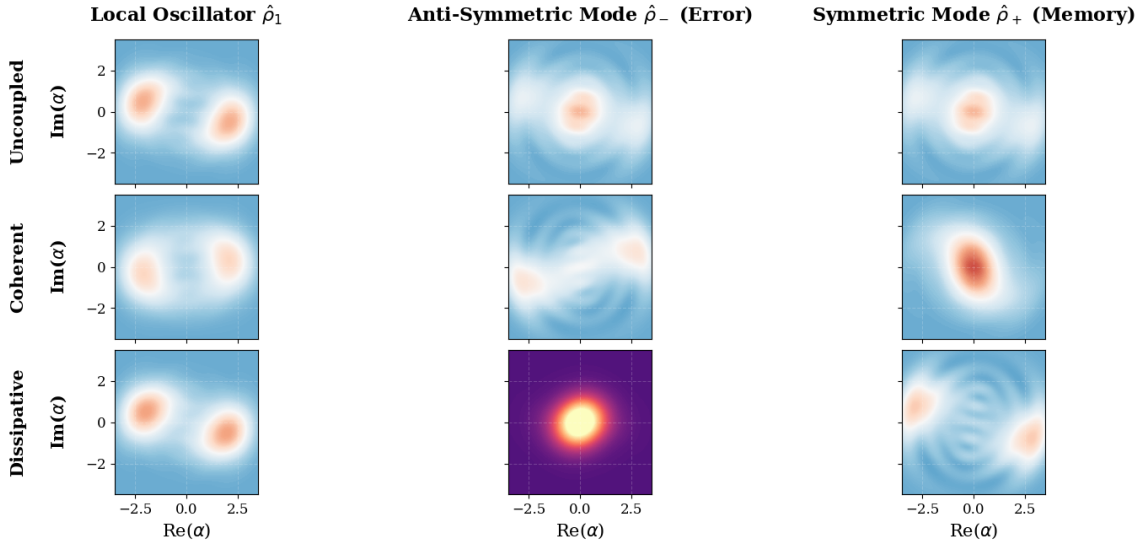

Figure 11: Supermode Wigner Tomography ($N = 9$). **Middle Row:** Coherent exchange ($J = 0.8$) rotates excitations without removing entropy. The relative error subspace $\hat{\rho}_-$ remains highly populated. **Bottom Row:** Collective dissipation ($\kappa = 1.5$) forcefully cools the anti-symmetric mode to the perfect quantum vacuum $|0\rangle\langle 0|$. The macroscopic Wigner structure is cleanly localized within the symmetric supermode $\hat{\rho}_+$.

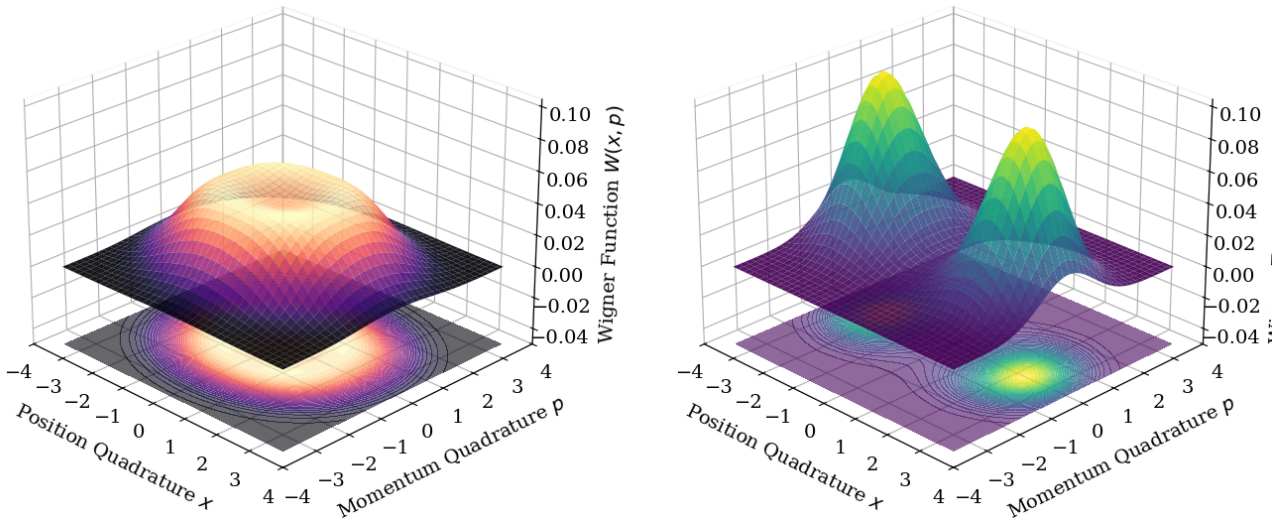

Figure 12: Three-dimensional Wigner tomography of the anti-symmetric error supermode $\hat{\rho}_-$. **Left:** Under coherent Hamiltonian exchange, entropy generated by local dissipators remains trapped, resulting in a highly diffused quasi-probability puddle. **Right:** Under engineered collective dissipation, entropy is aggressively ejected into the environment, structurally collapsing the state into an infinitely sharp Gaussian spike centered precisely at the phase-space origin.

3.8 Quantum Associative Memory and State Discrimination

To execute the associative memory protocol, classical bit patterns are mapped onto the joint macroscopic metastable lobes. Operating under the combined action of local squeezing and collective dissipation, the bipartite phase space develops a highly stable $\mathbb{Z}_2 \otimes \mathbb{Z}_2$ manifold. Denoting the effective coherent amplitude of the symmetry-broken lobes as $\pm\alpha_0$, the four fundamental memory patterns correspond to the product states $|\pm\alpha_0\rangle \otimes |\pm\alpha_0\rangle$.

Information retrieval requires unambiguously identifying the state from a noisy initial input. Because the localized lobes possess a finite macroscopic overlap, standard projective measurements are inadequate. We implement Unambiguous State Discrimination (USD) via Positive Operator-Valued Measures (POVMs). Defining a set of positive semi-definite operators $\{\hat{\Pi}_k\}$ associated with the stored patterns and an inconclusive measurement operator $\hat{\Pi}_?$, the completeness relation requires:

$$\sum_{k=1}^{4} \hat{\Pi}_k + \hat{\Pi}_? = \mathbb{I}. \tag{3.18}$$

The instantaneous probability of retrieving the k-th pattern evaluates to $P_k(t) = \mathrm{Tr}[\hat{\Pi}_k \hat{\rho}(t)]$.

The minimum achievable error probability for symmetric binary discrimination is dictated by the Helstrom bound, which relies on the trace distance between the density matrices. For the coherent memory lobes, the overlap fidelity is $\mathcal{F}(\alpha_0) = |\langle\alpha_0|-\alpha_0\rangle|^2 = e^{-4|\alpha_0|^2}$. Taylor-expanding the Helstrom bound for the macroscopic limit ($|\alpha_0| \gg 1$) yields:

$$P_{err}^{Helstrom} = \frac{1}{2}\left(1 - \sqrt{1 - e^{-8|\alpha_0|^2}}\right) \approx \frac{1}{4} e^{-8|\alpha_0|^2}. \tag{3.19}$$

This exponential scaling dictates that sufficient parametric driving η is required to overcome intrinsic quantum overlap and minimize retrieval error.

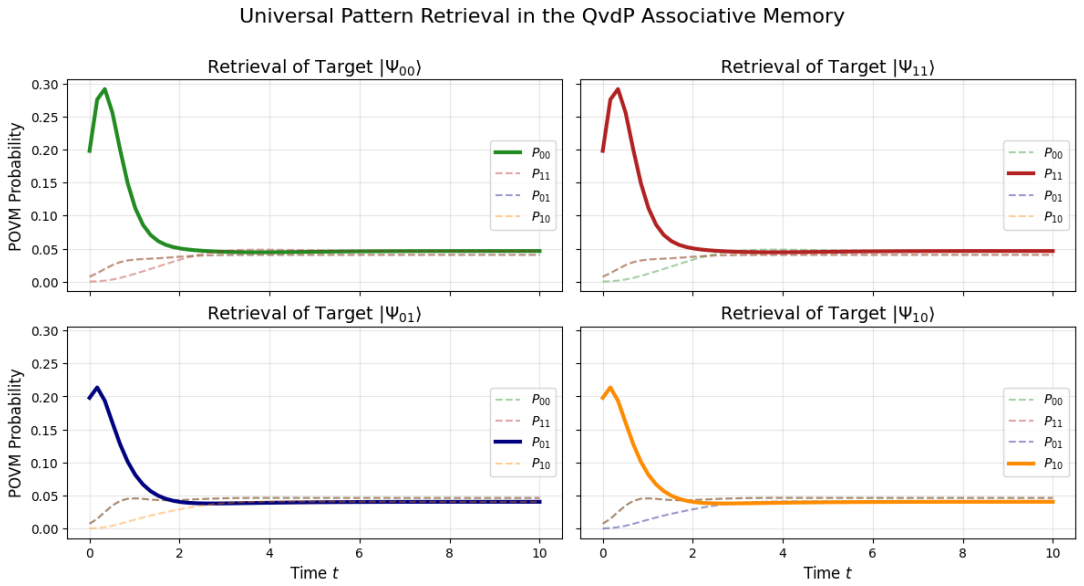

Figure 13: Universal pattern retrieval dynamics within the four-lobe metastable manifold ($N = 5$, $\kappa = 0.8$). Each panel represents a memory recall event triggered by a specifically biased noisy input. The solid line identifies the target POVM probability $P_{target}(t)$, while dashed lines track the error channels $P_{error}(t)$. The collective dissipative coupling drives the system into the correct macroscopic lobe before asymptotic phase diffusion takes over.

3.9 Associative Memory Storage Capacity

A fundamental metric for the associative memory architecture is the storage capacity α_c. In classical discrete spin-based Hopfield networks, the Hebbian learning rule imposes a critical capacity limit

of $\alpha_c^{Hebb} \approx 0.138$. In the continuous-variable framework, the effective dimension of the operational Hilbert space is determined by the necessary Fock-space truncation L_{max}, dynamically evaluated by enforcing a negligible probability tail ($\epsilon = 10^{-9}$) for a Poisson distribution with mean $|\beta|^2$.

For an n-photon driven oscillator, the system stores n macroscopic patterns. The raw theoretical storage capacity is $\alpha_c = n/L_{max}$. To precisely capture the intrinsic quantum overlap between the macroscopic lobes, which limits state distinguishability, we scale this metric by the quantum fidelity of the non-orthogonal coherent states. The overlap fidelity between adjacent lobes is $F(\beta) = \exp\left[-2|\beta|^2(1-\cos(2\pi/n))\right]$. The effective storage capacity evaluates to:

$$\tilde{\alpha}_c = \alpha_c[1 - F(\beta)] = \frac{n}{L_{max}}\left[1 - e^{-2|\beta|^2(1-\cos(2\pi/n))}\right]. \tag{3.20}$$

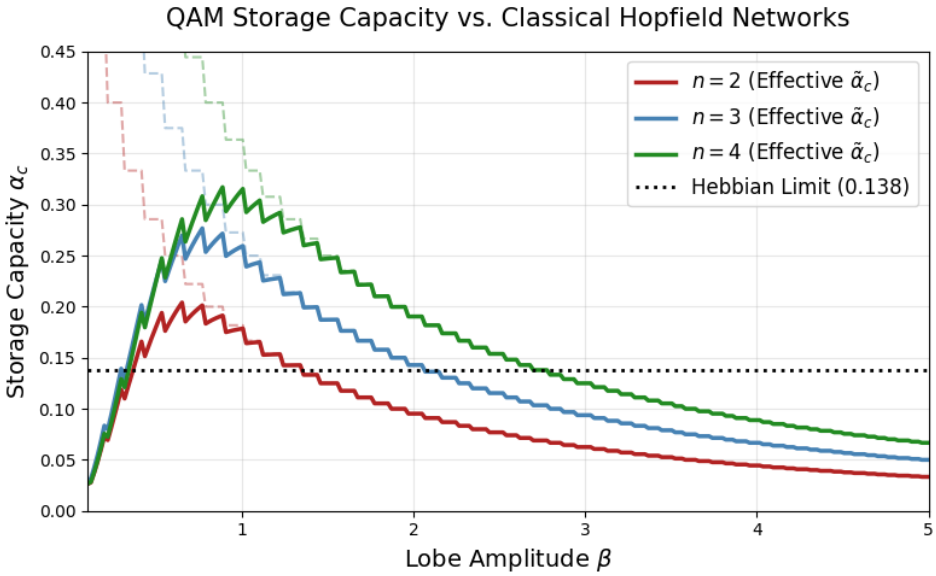

Figure 14: Effective storage capacity $\tilde{\alpha}_c$ as a function of the lobe amplitude β for varying non-linear drive exponents n. Solid lines denote the effective capacity, while faded dashed lines represent the raw capacity α_c. The horizontal dotted line marks the classical Hebbian limit ($\alpha_c^{Hebb} = 0.138$). In the intermediate regime ($1 \leq \beta \leq 3$), the continuous-variable quantum memory surpasses the classical limit.

3.10 Continuous Measurement and Stochastic Unraveling

To address macroscopic state detection under experimental monitoring (e.g., continuous homodyne detection), we transition from the deterministic ensemble average to the Itô Stochastic Master Equation (SME). Monitoring the local quadrature of the primary readout node with measurement efficiency η_d and rate γ_{hom}, the conditional density matrix $\hat{\rho}_c(t)$ obeys:

$$d\hat{\rho}_c(t) = \mathcal{L}_{net}[\hat{\rho}_c(t)]dt + \sqrt{\eta_d \gamma_{hom}}\mathcal{H}[\hat{a}_1 e^{-i\theta}]\hat{\rho}_c(t)dW(t). \tag{3.21}$$

The measurement superoperator is defined as $\mathcal{H}[\hat{c}]\hat{\rho}_c = \hat{c}\hat{\rho}_c + \hat{\rho}_c\hat{c}^\dagger - \mathrm{Tr}[(\hat{c}+\hat{c}^\dagger)\hat{\rho}_c]\hat{\rho}_c$, and $dW(t)$ is the Wiener increment satisfying $dW(t)^2 = dt$.

Setting the local oscillator phase to $\theta = 0$, the measurement apparatus projects the system onto the canonical quadrature $\hat{x}_1$. The continuous homodyne photocurrent evaluates to:

$$I_{hom}(t)dt = \sqrt{\eta_d \gamma_{hom}}\langle \hat{x}_1 \rangle_c(t)dt + \frac{dW(t)}{\sqrt{2}}. \tag{3.22}$$

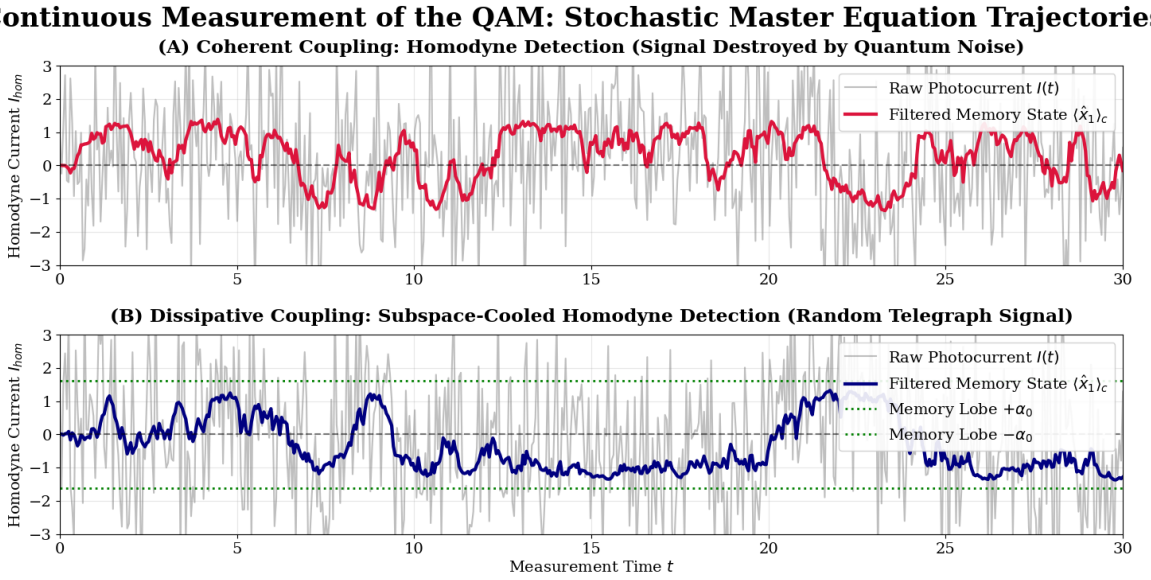

Figure 15: Stochastic quantum trajectories simulating the continuous homodyne photocurrent $I_{hom}(t)$. The gray background represents the Wiener fluctuations, while the thick line represents the conditionally filtered memory expectation value $\langle \hat{x}_1 \rangle_c$. **(A) Coherent Coupling:** Unitary exchange fails to damp thermal excitations, preventing symmetry breaking; the expectation value collapses toward zero. **(B) Dissipative Coupling:** The network topological cooling isolates the symmetric supermode. The measurement forces the wave-function to collapse into the macroscopic memory lobe $+\alpha_0$, generating a Random Telegraph Signal characterized by robust, experimentally resolvable plateaus.

The numerical integration of the SME reveals that macroscopic pattern recall corresponds to a process of spontaneous symmetry breaking induced by measurement back-action. Under collective dissipation, the trajectory purifies into a definite logical pattern, validating the physical operability of the continuous-variable architecture.

3.11 Transient Amplitude Dynamics and Symmetry Breaking

In the deep quantum regime, continuous-variable synchronization is intrinsically transient, governed by the Liouvillian spectral gap. Projecting the temporal evolution of the local field quadrature $\langle \hat{X}_1(t) \rangle = \mathrm{Re}\langle \hat{a}_1(t) \rangle$ onto the biorthogonal eigenbasis yields:

$$\langle \hat{a}_1(t) \rangle = \mathrm{Tr}[\hat{a}_1 \hat{\rho}_{ss}] + \sum_{j \geq 1} c_j \mathrm{Tr}[\hat{a}_1 \hat{\rho}_j] e^{(-\Gamma_j + i\nu_j)t}. \tag{3.23}$$

Because the squeezed QvdP master equation possesses a global $\mathbb{Z}_2$ parity symmetry and the annihilation operator is parity-antisymmetric, the asymptotic expectation value identically vanishes ($\mathrm{Tr}[\hat{a}_1 \hat{\rho}_{ss}] = 0$). For timescales $t \sim \Gamma_2^{-1}$, the fast modes decay, and the amplitude dynamics is governed by the dominant slow mode:

$$\langle \hat{a}_1(t) \rangle \approx c_1 \mathrm{Tr}[\hat{a}_1 \hat{\rho}_1] e^{-\Gamma_1 t}. \tag{3.24}$$

This indicates that quantum entrainment manifests as a metastable plateau. During this extended temporal window, the macroscopic phase remains rigidly locked, effectively mimicking classical symmetry breaking and providing a robust substrate for information encoding. However, unavoidable noise-induced quantum phase slips drive the system out of this plateau, restoring the global parity symmetry and causing the unconditional asymptotic decay of the macroscopic signal.

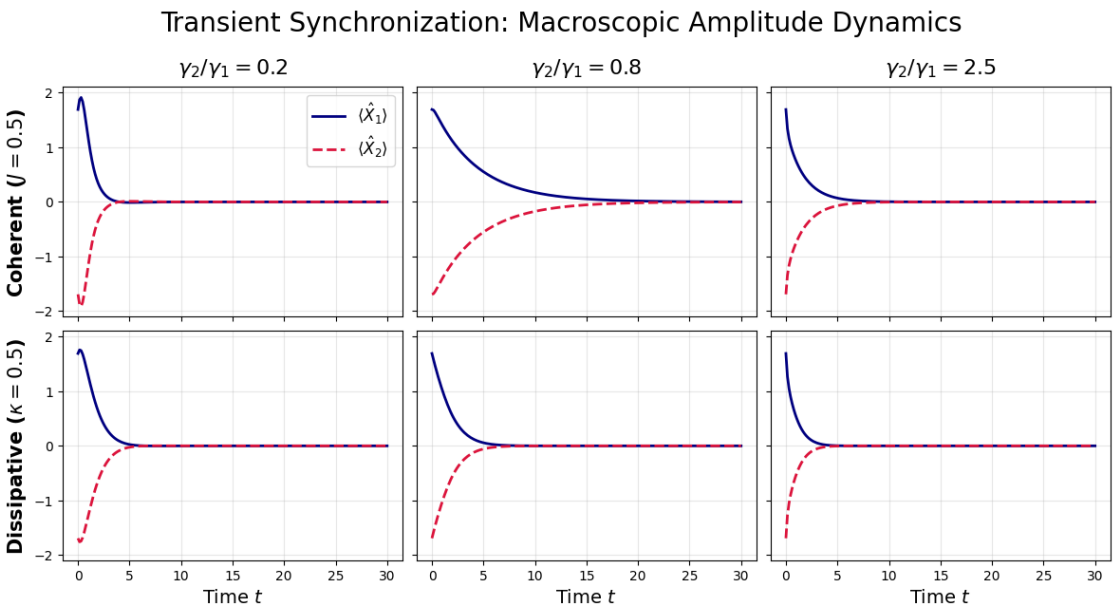

Figure 16: Real-time synchronization dynamics of the quadratures $\langle \hat{X}_1(t) \rangle$ (blue) and $\langle \hat{X}_2(t) \rangle$ (red) from anti-synchronized initial states ($N = 7$, $\Delta = 0.5, \eta = 0.4$). **Top Row:** Coherent coupling ($J = 0.5$) induces quasi-periodic beating and amplitude collapse. **Bottom Row:** Dissipative coupling ($\kappa = 0.5$) forces quadrature alignment, establishing a metastable synchronization plateau whose lifetime is bounded by Γ_1^{-1}.

To evaluate the microscopic mechanism of quantum phase diffusion, we simulate single experimental runs utilizing the Quantum Jump (Monte Carlo) approach, where continuous deterministic evolution is interrupted by discrete stochastic quantum jumps generated by the Lindblad collapse operators $\hat{L}_k$.

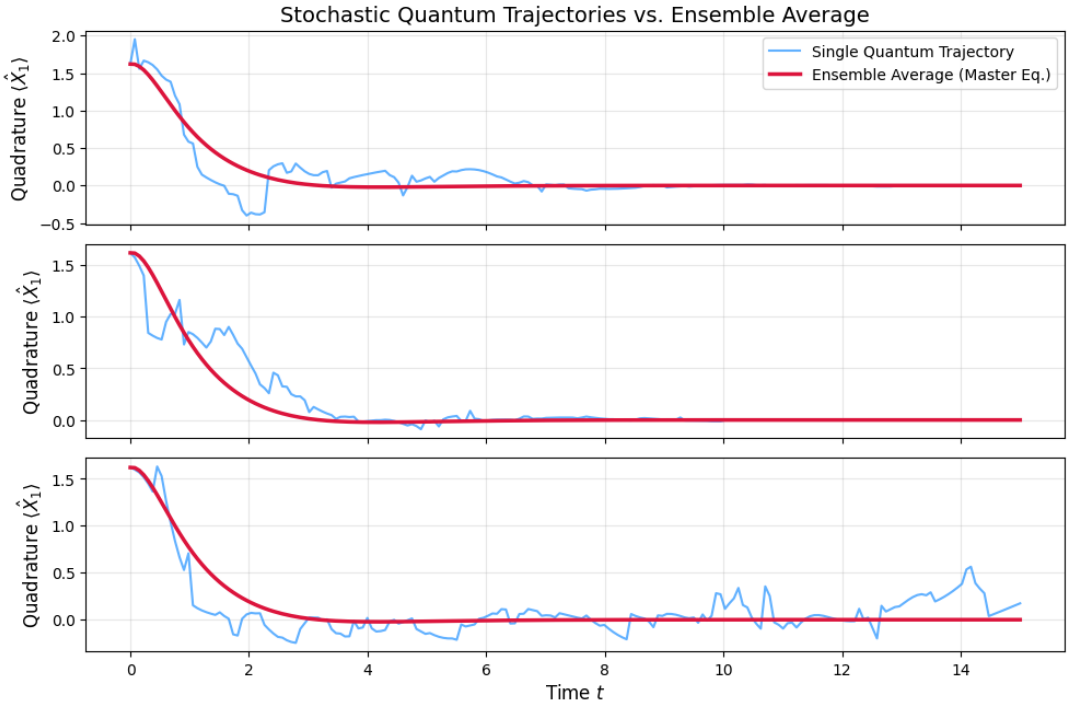

Figure 17: Stochastic quantum trajectories (blue lines) compared against the deterministic ensemble average (crimson lines) under dissipative coupling. The individual trajectories exhibit discrete fluctuations induced by single-photon emission and two-photon absorption events, confirming that the metastable plateau is a dynamic, noisy equilibrium.

Under continuous homodyne monitoring, the measurement back-action $dW(t)$ dynamically breaks the $\mathbb{Z}_2$ symmetry. Starting from a symmetric vacuum state, the granular noise perturbs the state off the saddle point, inducing an exponential geometric collapse into one of the target lobes (spontaneous symmetry breaking).

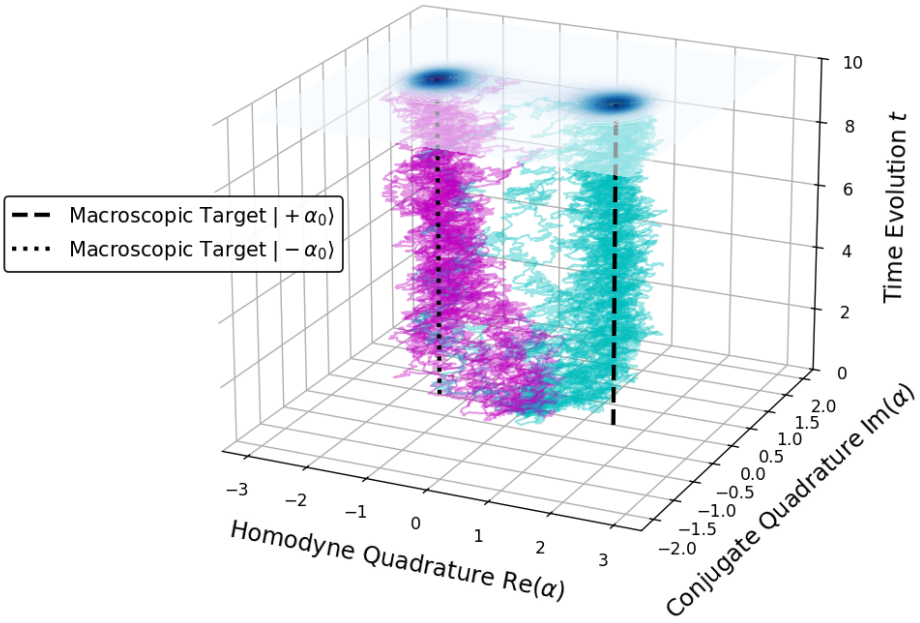

Figure 18: Phase-Time manifold tracking simultaneous Monte Carlo stochastic unravelings initialized at the quantum vacuum. The measurement back-action physically breaks the $\mathbb{Z}_2$ symmetry, forcing the trajectories to diverge and collapse into macroscopic branches aligned with the theoretical attractors $\pm\alpha_0$.

3.12 Information Geometry of Memory Retrieval

To evaluate the dynamic optimality of the Lindbladian retrieval process, we embed the relaxation dynamics within the framework of Quantum Information Geometry. The infinitesimal distinguishability between two quantum states $\hat{\rho}_{\boldsymbol{\theta}}$ and $\hat{\rho}_{\boldsymbol{\theta}+d\boldsymbol{\theta}}$ defines a Riemannian metric, the Quantum Fisher Information Metric (QFIM) $g_{\mu\nu}$, via the Symmetric Logarithmic Derivative (SLD) $\hat{L}_\mu$:

$$ds^2 = \frac{1}{4}\sum_{\mu,\nu} \mathrm{Tr}\left[\hat{\rho}_{\boldsymbol{\theta}} \frac{\hat{L}_\mu \hat{L}_\nu + \hat{L}_\nu \hat{L}_\mu}{2}\right] d\theta^\mu d\theta^\nu. \tag{3.25}$$

Operating deeply within the metastable plateau, the Extreme Metastable States are approximated by non-displaced Gaussian continuous-variable states, mapping the density matrix to its displacement vector $\boldsymbol{d}$ and covariance matrix $\boldsymbol{V}$. The collective dissipator $\mathcal{D}[\hat{b}_-]$ drives the anti-symmetric supermode to the vacuum state, forcing the covariance sub-matrix $\boldsymbol{V}_-$ asymptotically toward the Heisenberg limit $\frac{1}{2}\boldsymbol{I}$.

By applying the continuous-variable Cauchy-Schwarz inequality to the time-parameterized Bures distance, the thermodynamic length $\mathcal{L}$ of the memory retrieval process evaluates to:

$$\mathcal{L} = \int_0^{\tau_{ret}} \sqrt{\sum_{\mu,\nu} g_{\mu\nu}\dot{\theta}^\mu \dot{\theta}^\nu}\, dt = \int_0^{\tau_{ret}} \sqrt{\mathrm{Tr}\left[\hat{\rho}(t)\hat{L}_t^2\right]}\, dt. \tag{3.26}$$

The environmental jump operator $\kappa\mathcal{D}[\hat{b}_-]$ generates a gradient descent along the eigenvectors of the QFIM, forcing the open quantum system to evolve along a Riemannian geodesic, thereby minimizing the thermodynamic length of the memory retrieval.

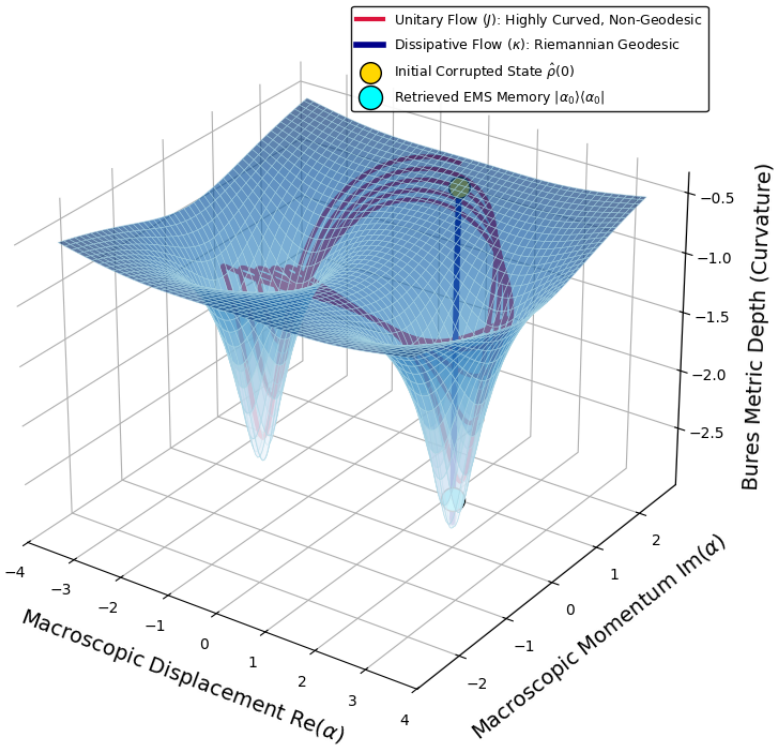

Figure 19: Quantum Information Geometry of the associative memory retrieval mapped onto the Riemannian manifold defined by the Bures metric curvature. Unitary Hamiltonian exchange J (red trajectory) traces a highly curved, non-geodesic path that fails to dissipate the quantum variance. The engineered collective dissipation κ (blue trajectory) contracts the metric, driving the system along a Riemannian geodesic directly into the macroscopic memory lobe (cyan sphere).

3.13 Non-Equilibrium Thermodynamics and the Wigner Probability Flux

In the deep quantum regime, the encoded memory is a Non-Equilibrium Steady State (NESS) continuously sustained by the thermodynamic ejection of entropy. This is formalized by deriving the Wigner Phase-Space Probability Current $\mathbf{J}(\mathbf{r})$.

The continuity equation for the Wigner quasi-probability density $W(\mathbf{r})$ is given by $\partial_t W + \nabla \cdot \mathbf{J} = 0$. The macroscopic probability flux vector $\mathbf{J}(\mathbf{r})$ is defined by the deterministic Liouvillian drift $\mathbf{A}(\mathbf{r})$ and the quantum diffusion tensor $\mathbf{D}$:

$$\mathbf{J}(\mathbf{r}) = \mathbf{A}(\mathbf{r})W(\mathbf{r}) - \frac{1}{2}\mathbf{D}\nabla W(\mathbf{r}). \tag{3.27}$$

The introduction of the frequency detuning ($\Delta \neq 0$) injects a non-conservative rotational force, ensuring that the curl of the drift is strictly non-zero ($\nabla \times \mathbf{A} \neq \mathbf{0}$). This explicitly breaks the detailed balance condition, forming persistent topological vortices in the divergence-free steady-state flux ($\nabla \times \mathbf{J}_{ss} \neq \mathbf{0}$). The irreversible entropy production rate $\dot{\Sigma}_{irrev}$ required to stabilize the memory patterns is quantified by:

$$\dot{\Sigma}_{irrev} = \int d^2\mathbf{r}\, \frac{\mathbf{J}(\mathbf{r}) \cdot \mathbf{D}^{-1}\mathbf{J}(\mathbf{r})}{W(\mathbf{r})} > 0. \tag{3.28}$$

This strictly positive entropy production rate encapsulates the fundamental thermodynamic cost required to sustain the macroscopic phase coherence of the network. It explicitly demonstrates that the protection of the encoded classical information within the continuous-variable substrate is not a passive property, but rather an active, non-equilibrium process fueled by continuous energy dissipation. The structural stability of the quantum associative memory is inextricably linked to the persistent breaking of time-reversal symmetry driven by the engineered environment.

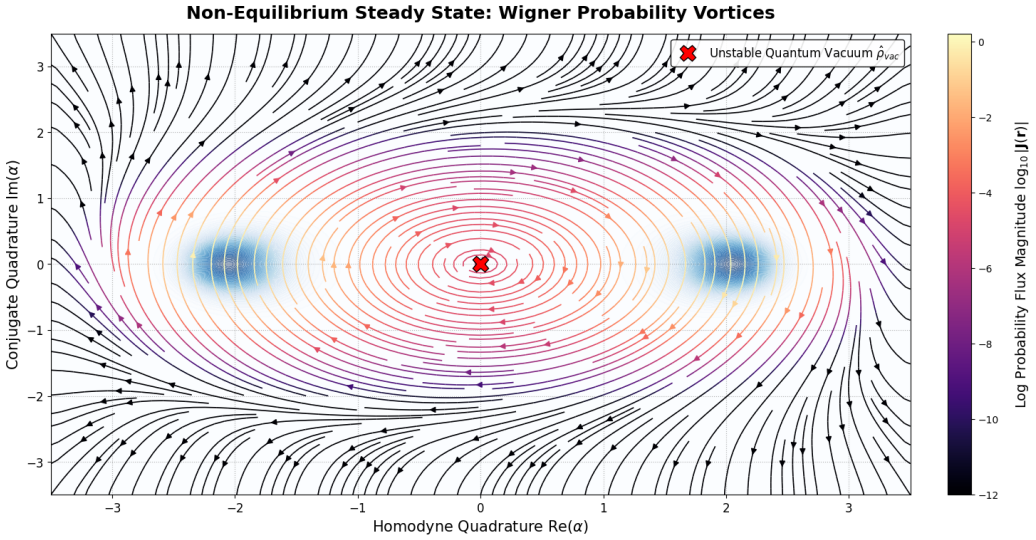

Figure 20: Two-dimensional quantum fluid dynamics of the Wigner Probability Flux $\mathbf{J}(\mathbf{r})$. Overlaid on the symmetric probability distribution $W(x, p)$ are the vector streamlines colored by the logarithmic flux magnitude $\log_{10}|\mathbf{J}(\mathbf{r})|$ to resolve the exponential scaling of quantum diffusion. The breakdown of detailed balance morphs the static classical attractors into dynamic quantum vortices. Sustaining these rotational currents requires continuous thermodynamic work ($\dot{\Sigma}_{irrev} > 0$).

4 Conclusions

In this work, we reviewed, synthesized, and computationally verified the nonequilibrium dynamics of quantum synchronization and its application to continuous-variable Quantum Associative Memories.

Expanding into the deep quantum regime via the GKSL master equation, we demonstrated that intrinsic quantum noise induces continuous phase-slips that destroy synchronization under conservative interaction topologies. Unitary Hamiltonian exchange fails to damp these fluctuations, leading to level repulsion and the breakdown of the synchronization order parameter.

We established that continuous-variable quantum associative memories require an engineered non-local Lindblad jump operator. Through the formalisms of Information Geometry and stochastic measurement unraveling, we proved that collective dissipation acts as an active thermodynamic sink, cooling the anti-symmetric subspace to the absolute quantum vacuum. This mechanism suppresses the relative-phase quantum fluctuations, routing the state evolution along a Riemannian geodesic and stabilizing the macroscopic $\mathbb{Z}_2 \otimes \mathbb{Z}_2$ memory manifold.

Acknowledgments

The author gratefully acknowledges Dr. Albert Cabot for his invaluable supervision, insightful guidance, and constructive discussions throughout this work. The author also thanks Daniel Ruiz Reynés for the outstanding coordination of the SURF@IFISC 2026 Fellowship Program and for creating an inspiring research environment, and Neus Lacomba Moreno for her invaluable administrative and logistical assistance. This work was supported by the SURF@IFISC 2026 Fellowship Program.

References

[1] T. E. Lee and H. R. Sadeghpour, "Quantum synchronization of quantum van der Pol oscillators with trapped ions", *Phys. Rev. Lett.* **111**, 234101 (2013).

[2] S. Walter, A. Nunnenkamp, and C. Bruder, "Quantum synchronization of a driven self-sustained oscillator", *Phys. Rev. Lett.* **112**, 094102 (2014).

[3] A. Cabot, G. L. Giorgi, and R. Zambrini, "Metastable quantum entrainment", *New J. Phys.* **23**, 103017 (2021).

[4] A. Labay-Mora, R. Zambrini, and G. L. Giorgi, "Quantum associative memory with a single driven-dissipative nonlinear oscillator", *Phys. Rev. Lett.* **130**, 190602 (2023).

[5] S. Walter, A. Nunnenkamp, and C. Bruder, "Quantum synchronization of two Van der Pol oscillators", *Annalen der Physik* **527**, 131–138 (2015).

[6] J. T. Barreiro *et al.*, "An open-system quantum simulator with trapped ions", *Nature* **470**, 486–491 (2011).

Quantum reservoir computing in multiphoton Jaynes-Cummings systems

Ricardo Costa, Sreetama Das, and Roberta Zambrini
Instituto de Física Interdisciplinar y Sistemas Complejos, IFISC (CSIC-UIB)
Campus Universitat de les Illes Balears, E-07122 Palma de Mallorca, Spain

Abstract

Quantum reservoir computing (QRC) is a powerful machine learning framework for chaotic time-series prediction. In this work, we explore the possibility of using the Jaynes-Cummings model with multiphoton interactions between a qubit and a bosonic mode as a quantum reservoir. Recent results [1] have shown that Jaynes-Cummings model with single-photon interaction works as an efficient reservoir. Multiphoton interaction introduces higher degree of nonlinearity in the Hamiltonian, which can have possible benefits in improving the nonlinear memory of the reservoir. Motivated by this, we focus on the two-photon Jaynes-Cummings model and systematically compare its performance with the single-photon model for both linear and nonlinear memory tasks. Our results show that the choice of features used in the readout layer plays an important role in determining the relative memory capacity of the two reservoirs. In this report, we present the detailed reservoir model, QRC methodology, followed by a discussion of our results, alongside key open questions reserved for future investigation.

1 Introduction

Time series prediction is a ubiquitous task in a wide range of real-life scenarios, such as weather prediction, speech recognition, stock market prediction, to name a few. Recurrent neural networks (RNNs) are a powerful supervised-learning framework that have achieved considerable success in such tasks. However, the recurrent feedback structure of RNNs makes their training challenging, particularly due to the vanishing and exploding-gradient problems. In the early 2000s, Echo State Networks (ESNs) and Liquid State Machines (LSMs) emerged as novel paradigms designed to overcome these training limitations of traditional RNNs. These developments marked the inception of Reservoir Computing (RC).

The core principle of RC is to avoid the explicit training of the hidden layers, replacing them with a high-dimensional dynamical system or mathematical construct called 'reservoir'. As input signals propagate through this reservoir, they undergo nonlinear transformations into a high-dimensional feature space before reaching the output layer. Consequently, provided the reservoir has sufficient capacity, a simple linear regression at the readout layer suffices as the sole trainable component, achieving performance comparable to deep neural networks that require extensive layer-by-layer optimization. Besides high dimensional state-space and nonlinear input processing capability, a reservoir computer must satisfy three fundamental properties:

1. **Echo-State Property:** after a sufficient number of input injections, the state of the reservoir does not depend on the initial state, but it depends only on previous inputs.
2. **Fading Memory:** the influence of past inputs on the reservoir state gradually decreases over time, ensuring that the current state reflects predominantly recent temporal history. It is referred to as the 'memory' of the reservoir, and is essential for chaotic time series prediction.
3. **Input separability:** the reservoir should map distinguishable inputs onto sufficiently distinct features, enabling the readout layer to discriminate between them effectively.

Following the seminal work of Fujii and Nakajima [2], utilization of quantum systems as physical reservoirs has gained considerable interest. The authors in [2] demonstrated that the input information can effectively propagate across the vast Hilbert space of a disordered quantum-spin network, achieving substantial success as high-performance quantum reservoir computer. Following this, a large number of works have investigated QRC in other quantum physical systems, e.g. gaussian states of quantum harmonic oscillators [3], nonlinear quantum harmonic oscillators [4],

bosonic and fermionic systems [5], and spin-boson models [1] etc.

Spin-boson systems constitute an interesting hybrid platform, since they couple finite-dimensional spins to infinite-dimensional bosonic modes. The Jaynes-Cummings (JC) model describes linear interaction between a two-level quantum system (qubit) and a single bosonic mode through the exchange of one photon. In ref. [1] the authors explored QRC in JC model and its dispersive limit (DJC), having investigated the linear/non-linear memory and time-series prediction capability. This showed a better nonlinear memory of these systems compared to linear memory. In this project, we explore the two-photon JC model, in which the qubit and the mode interact through an exchange of two photons. Such interaction is inherently nonlinear. In particular, our goal is to investigate the effect of increasing the nonlinearity of the qubit-boson interaction on the memory capacity of the reservoir, and whether this provides any improvement over the performance of the single-photon JC model.

2 Theoretical model

Jaynes-Cummings model is a canonical model in quantum optics [6]. It describes interaction between a two-level atom and a single-mode of an electromagnetic field through the exchange of one single photon. In experimental platforms, one can use physical atoms as well as other types of two-dimensional quantum systems, for example, superconducting qubits. Therefore, in this report, we use the word 'qubit' instead of atoms, and the single mode is referred to as 'bosonic mode'. The Hamiltonian of single-photon Jaynes Cummings model is

$$H_{\text{JC}} = \frac{\omega_a}{2}\sigma^z + \omega_b a^\dagger a + \chi\left(\sigma^+ a + \sigma^- a^\dagger\right), \tag{2.1}$$

where we have taken $\hbar = 1$. Here a ($a^\dagger$) is the bosonic annihilation (creation) operator, σ^+ (σ^-) is the atomic raising (lowering) operator, and σ^z is the Pauli-z operator. The first term represents the Hamiltonian of the qubit, with a gap ω_a between the ground and the excited state. The second term represents the Hamiltonian of a bosonic mode with frequency ω_b. The last term takes into account the qubit-mode interaction with strength χ. It originates from a dipolar interaction between the atom and the field after one applies the rotating wave approximation in the limit $\omega_a, \omega_b \gg \chi$ and $|\omega_a - \omega_b| \ll |\omega_a + \omega_b|$.

In this work, we will consider a more complex and nonlinear interaction, namely two-photon Jaynes-Cummings model, in which the qubit and the boson interact through the exchange of two photons. Such an interaction can be engineered when ω_a is resonant or nearly resonant with $2\omega_b$. The Hamiltonian for the two-photon Jaynes-Cummings model is

$$H_{2\text{-JC}} = \frac{\omega_a}{2}\sigma^z + \omega_b a^\dagger a + \chi\left(\sigma^+ a^2 + \sigma^- \left(a^\dagger\right)^2\right). \tag{2.2}$$

Since the atom is able to exchange two photons with the bosonic mode, for the same interaction strength the two-photon JC model results in higher occupation of the bosonic mode compared to single-photon JC model, which implies an effectively higher dimension of the reservoir for the former. Our goal is to investigate whether this increased dimension as well as the increased nonlinearity affect the capacity of the reservoir to memorize past inputs.

To encode the input in the dynamics of the reservoir, we drive the bosonic mode using a classical field with a time dependent amplitude $\beta(t)$ and frequency ω_d, the amplitude itself encoding the input. The driving hamiltonian is

$$H_{\text{drive}} = \beta(t)\left(e^{-i\omega_d t}a^\dagger + e^{i\omega_d t}a\right) \tag{2.3}$$

Therefore, the total hamiltonian becomes,

$$H = H_{2\text{-JC}} + H_{\text{drive}} = \frac{\omega_a}{2}\sigma^z + \omega_b a^\dagger a + \chi\left(\sigma^+ a^2 + \sigma^- \left(a^\dagger\right)^2\right) + \beta(t)\left(e^{-i\omega_d t}a^\dagger + e^{i\omega_d t}a\right). \tag{2.4}$$

For the purpose of numerical simulation, it is useful to move to the rotating frame of the driving field, so the Hamiltonian becomes,

$$H = \left(\frac{\omega_a}{2} - \omega_d\right)\sigma^z + \underbrace{(\omega_b - \omega_d)}_{\Delta_b} a^\dagger a + \chi\left(\sigma^+ a^2 + \sigma^- \left(a^\dagger\right)^2\right) + \beta(t)\left(a^\dagger + a\right) \tag{2.5}$$

In reality, all quantum systems are perturbed by environmental interaction, so the evolution of our reservoir is not unitary. The evolution is described by the Lindblad master equation,

$$\dot{\rho} = -i[H, \rho] + \sum_i \left(L_i \rho L_i^\dagger - \frac{1}{2} L_i^\dagger L_i \rho - \frac{1}{2} \rho L_i^\dagger L_i \right), \tag{2.6}$$

where ρ is the density operator of the joint qubit-boson system, and L_i's are the Lindblad operators which take account the loss processes occurring during the evolution. We consider the following loss processes:

- **Cavity photonic loss (κ):** described by collapse operator $L_\kappa = \sqrt{\kappa}\, a$, accounting for single-photon leakage through cavity mirrors into the external continuum at rate κ.
- **Atomic spontaneous emission (γ):** described by $L_\gamma = \sqrt{\gamma}\, \sigma^-$, representing spontaneous decay from the excited state $|e\rangle$ to the ground state $|g\rangle$ at rate γ.
- **Atomic pure dephasing (γ_ϕ):** described by $L_{\gamma_\phi} = \sqrt{\gamma_\phi}\, \sigma^z$, parameterizing phase coherence loss between superposition states at rate γ_ϕ.

Particularly, these ways of information leaking out of the system are what allow the reservoir to have fading-memory and echo-state property.

3 Methodology

There are three main steps of doing reservoir computing in our physical reservoir:

- The cavity is driven with a classical field with constant amplitude β_i during a time interval dt. During this time, the dynamics of the reservoir acts as a nonlinear mapping of the input, resulting in features which can be extracted by measuring the reservoir.
- For each input, a number of observables are measured during the evolution of the reservoir, resulting in n features. For the same reservoir, one has multiple choices of such observable sets.
- The above steps are repeated for all training data points. Therefore for N_{train} inputs we have an $N_{\text{train}} \times n$ dimensional array $\mathbf{X}$ of features. A classical linear regression is performed to map $\mathbf{X}$ to the array of target outputs $\mathbf{y}$, therefore we have

$$\mathbf{X}\mathbf{W} \approx \mathbf{y}, \tag{3.1}$$

  where $\mathbf{W}$ are the weights obtained from the regression.

Prior to training, we have to discard a number of these evolution cycles (washout phase), so that the reservoir loses its dependence on the initial state. Following the training, the weights $\mathbf{W}$ can be used to predict outcomes of new data points. A graphic summary of the complete reservoir system is presented in Fig. 1.

This scheme was implemented in python, using QuTiP to solve the quantum open system evolution and Scikit-learn for the classical regression. Specifically, we employ Ridge regression, which minimizes the standard linear regression loss function with an additional regularization term that penalizes large weight magnitudes. This penalty term relevance is fixed by a coefficient α. We see that the reservoir's performance is generally optimum when $\alpha = 0$, so in practice we use a simple linear regression.

For our work, we choose the expectation values of the following operators as the readout features:

$$\begin{aligned}\mathcal{O} = \{&N, N^2, N^3, N^4, c^\dagger, (c^\dagger)^2, (c^\dagger)^3, (c^\dagger)^4, (c^\dagger)^5, Nc^\dagger, Nc, N(c^\dagger)^2, Nc^2, N(c^\dagger)^3, \\ &Nc^3, N(c^\dagger)^4, Nc^4, N(c^\dagger)^5, Nc^5, N^2c^\dagger, N^2c, N^2(c^\dagger)^2\}.\end{aligned} \tag{3.2}$$

For the non-hermitian operators, we have used the real and imaginary parts of the expectation values as two different features. In total, we get 40 features from each input to be used for the regression. However, to further avail more features, we use time multiplexing which means that during dt we measure the expectation values in V different moments. Therefore, for each input we have $N = 40 \times V$ features. This significantly improves the reservoir's performance.

The bosonic mode has an infinite dimensional Hilbert space. For numerical simulation, we have to truncate it to a finite dimension. This adds a constraint on our simulation, because we must be sure to work in a parameter regime so that the levels above the truncation level are never populated. To take care of this we always checked the heatmap of the reduced density matrix elements of the bosonic mode (it is obtained by taking the partial trace over the qubit subspace). After doing some

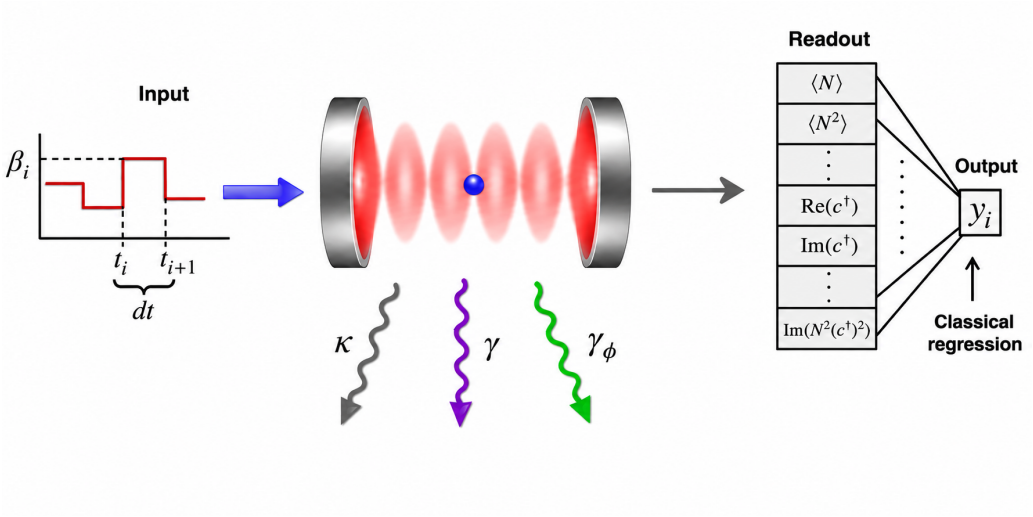

Figure 1: Schematic summary of the quantum reservoir computing (adapted from [1]). Input β_i is encoded into the reservoir by driving the cavity with a classical field of constant amplitude β_i for a time dt. There are three dissipation channels: cavity photonic loss (κ), atomic spontaneous emission (γ), and atomic pure dephasing (γ_ϕ). In the readout layer, expectation values of some higher order bosonic operators are extracted as features to train a classical layer using linear regression, yielding the output prediction y_i for each input β_i.

test simulation, we have found that an experimentally realistic set of driving time and dissipation rates in order to keep the bosonic population below $n_c = 20$ are $dt = 10, \kappa = 0.1$, $\gamma = 0.05$, and $\gamma_\phi = 0.05$. In addition, we always consider perfect resonance between the qubit and the boson, i.e. $\omega_a = 2\omega_b$.The selected bosonic detuning is $\Delta_b = 2$. We show an example of heatmaps in Fig. 2 which shows that the two-photon model has higher levels of occupation than the single-photon one, however, for none of them the population crosses 20 levels. Lastly, we have considered time multiplexing with $V = 10$.

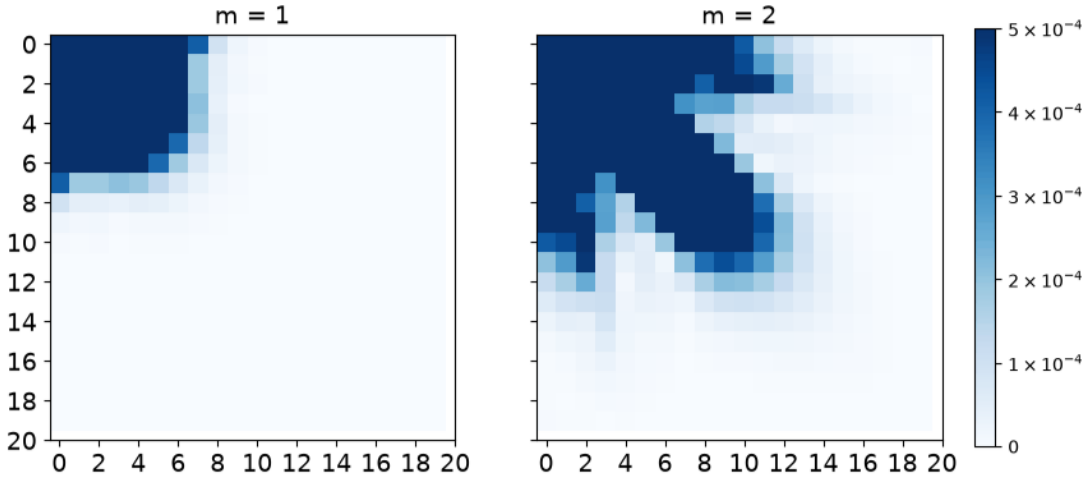

Figure 2: Absolute values of bosonic density matrix elements $|\rho_{i,j}|$ as heatmap for single (m=1) and two-photon (m=2) models. Negligible population near $n = 20$ verifies that the Hilbert space truncation is valid. It also shows that for same parameters, higher levels of the bosonic mode are populated when using the two-photon model. The parameters are $dt = 10$, $\chi = 1$, $\kappa = 0.1$, $\gamma = 0.05$, $\gamma_\phi = 0.05$ and $\Delta_b = 2$.

4 Results and discussion

We begin by verifying the nonlinear response of the readout features of our reservoir to the inputs. In Fig. 3, we plot the post-washout behavior of a subset of observables $\mathcal{O}$ with respect to increasing input strength $\beta \in [0, 1]$. It can be seen that the response to the input is highly nonlinear, which asserts that our reservoir satisfies an important criterion for reservoir computing.

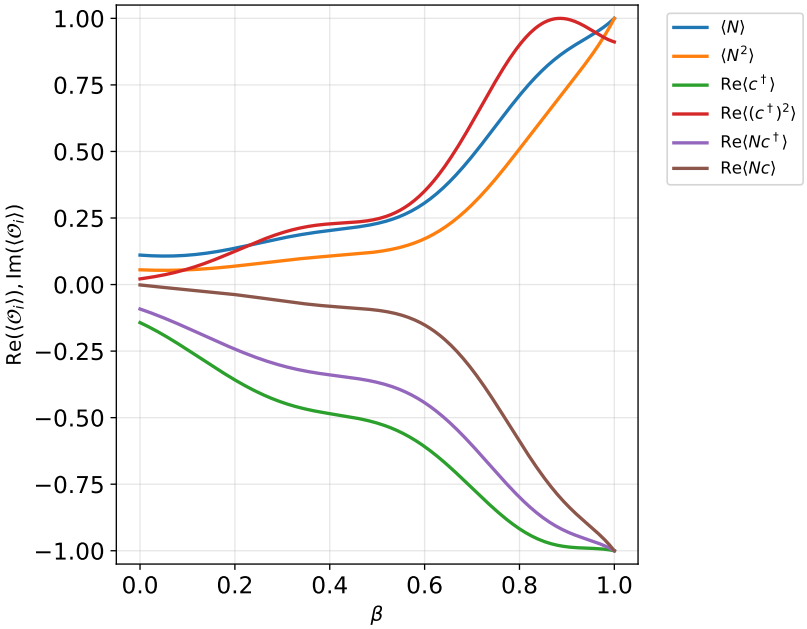

Figure 3: Nonlinear response of selected expectation values of the two-photon Jaynes-Cummings model to input β. The presented β sweep is performed after $N_0 = 1000$ washout inputs. The expectation values have been scaled to lie in the range $[-1, 1]$. The parameters are $dt = 10$, $\chi = 1$, $\kappa = 0.1$, $\gamma = 0.05$, $\gamma_\phi = 0.05$ and $\Delta_b = 2$.

Next, we verify the fading memory property of our reservoir. For this, we run two identical simulations driven with the same random inputs between 0 and 1, however, after the washout phase we change only the first input to observe how far in time the perturbation propagates. In Fig. 4 we see that despite having two different inputs in the first step, the system forgets the perturbation after a few input injections, and the features evolve in the same way. We have also presented the absolute difference between the expectation values for these two cases to make it more evident. This study confirms that our reservoir satisfies the fading memory property.

Finally, to quantitatively evaluate the memory capacity of our physical reservoir, we test its performance on two standard benchmark tasks driven by an input sequence $\{s_k\}$. These tasks decouple and evaluate two distinct features of the reservoirs, one is related to linear task's recovering capacity and the second is more focused on the non linear behavior.

Short-Term Memory (STM): The Short-Term Memory task tests the linear memory capacity of the system by measuring its ability to reconstruct past inputs $s_k \in [0, 1]$, drawn randomly from a uniform distribution, delayed by τ discrete steps. Therefore the target output at the kth step is:

$$y_k(\tau) = s_{k-\tau}. \tag{4.1}$$

Reconstruction performance is evaluated using the linear correlation capacity $C(\tau) \in [0, 1]$ between the true target $y_k(\tau)$ and the prediction $\hat{y}_k(\tau)$:

$$C(\tau) = \frac{\text{cov}^2(y(\tau), \hat{y}(\tau))}{\sigma(y(\tau))^2 \sigma\left(\hat{y}(\tau)\right)^2}, \tag{4.2}$$

where $\text{cov}(\cdot)$ denotes the sample covariance and $\sigma(\cdot)$ is the standard deviation.

Parity Check (PC): To evaluate complex nonlinear feature transformation alongside temporal storage ability, we implement the Parity Check task. In this case, the system is driven by a

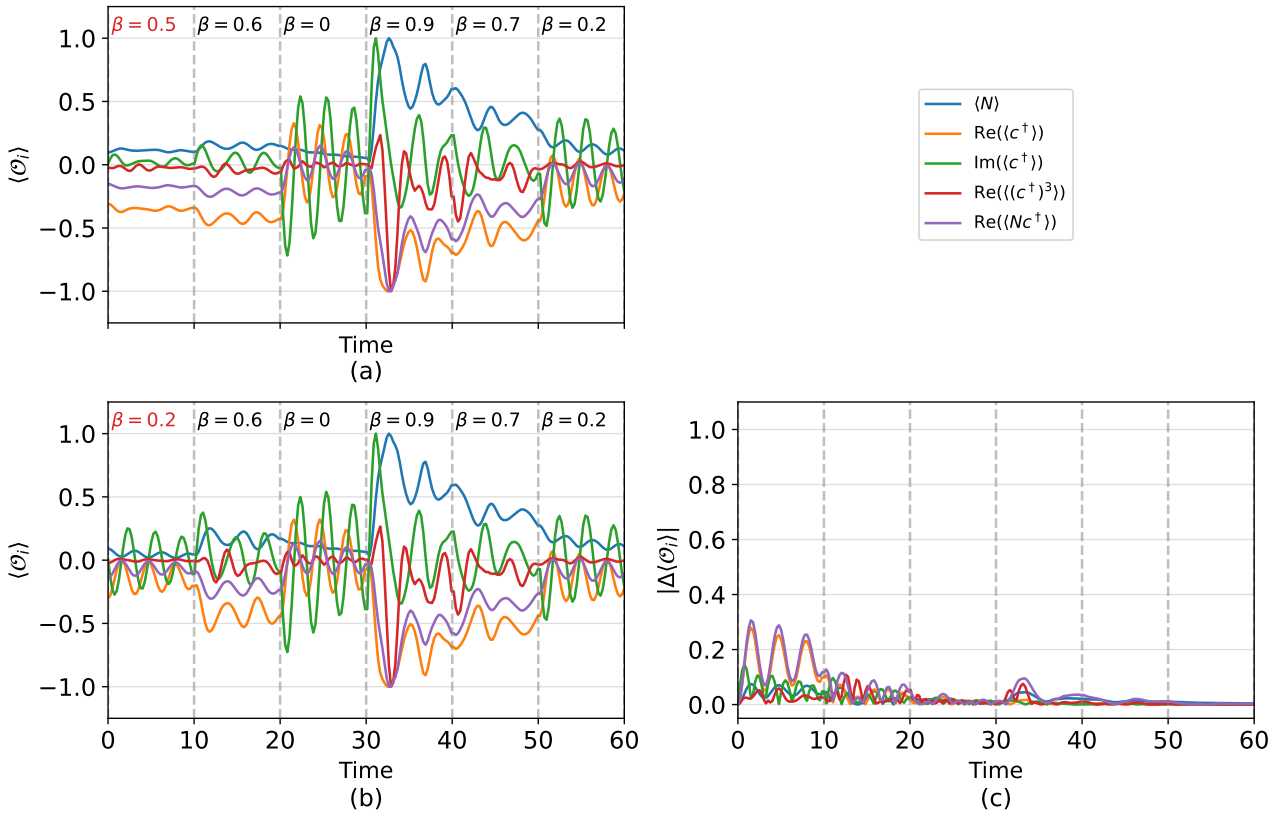

Figure 4: Dynamics of a selected set of features of our reservoir after $N_0 = 1000$ input injections in the washout phase. The dashed vertical lines denote the instances when a new input is introduced. In panels (a) and (b), despite having two different inputs in the first post-washout step, the features forget the history and evolve in the same way after a few steps, showing that the dynamics has fading memory. Panel (c) shows that the difference between the feature values fades away with new input injections. For presentation purposes, the expectation values have been scaled to lie in the range $[-1, 1]$.The parameters are $dt = 10$, $\chi = 1$, $\kappa = 0.1$, $\gamma = 0.05$, $\gamma_\phi = 0.05$ and $\Delta_b = 2$.

sequence of independent binary digits $s_i \in \{0, 1\}$. For a given delay τ, the target output y_i is calculated as the modulo-2 sum over the preceding τ inputs:

$$y_i = \left(\sum_{j=1}^{\tau} s_{i-j} \right) \bmod 2. \tag{4.3}$$

Because the modulo-2 operation represents a nonlinear mapping, achieving high capacity requires that the system's internal dynamics maps the temporal sequence into nonlinear combinations within the observable feature space $\mathcal{O}$. Nonlinear capacity is quantified using the same correlation metric $C(\tau)$ defined in Eq. (4.2).

In Fig. 5, we show the STM capacity of single-photon and two-photon JC model with increasing τ. We observe that the performance of the single-photon interaction model (m=1) is better than that of the two-photon model (m=2). This could be expected because, as we discussed, STM is a task that mainly measures the capacity of the reservoir to learn linear tasks, so a more linear model may have a better result on this benchmark.

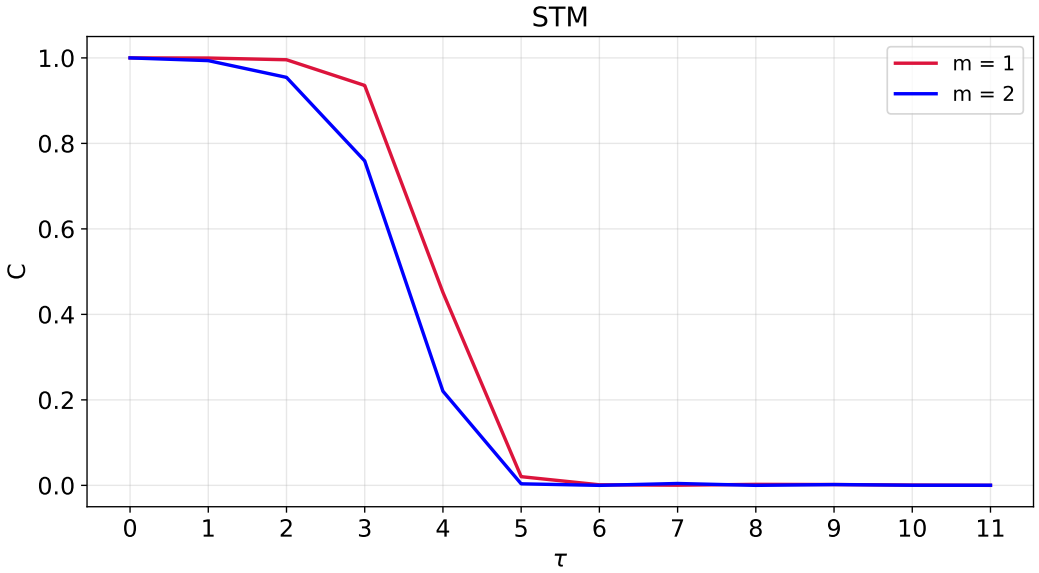

Figure 5: Short-Term Memory capacity $C(\tau)$ of single (m=1) and two-photon (m=2) JC model vs. delay τ. The parameters are $dt = 10$, $\chi = 1$, $\kappa = 0.1$, $\gamma = 0.05$, $\gamma_\phi = 0.05$ and $\Delta_b = 2$.

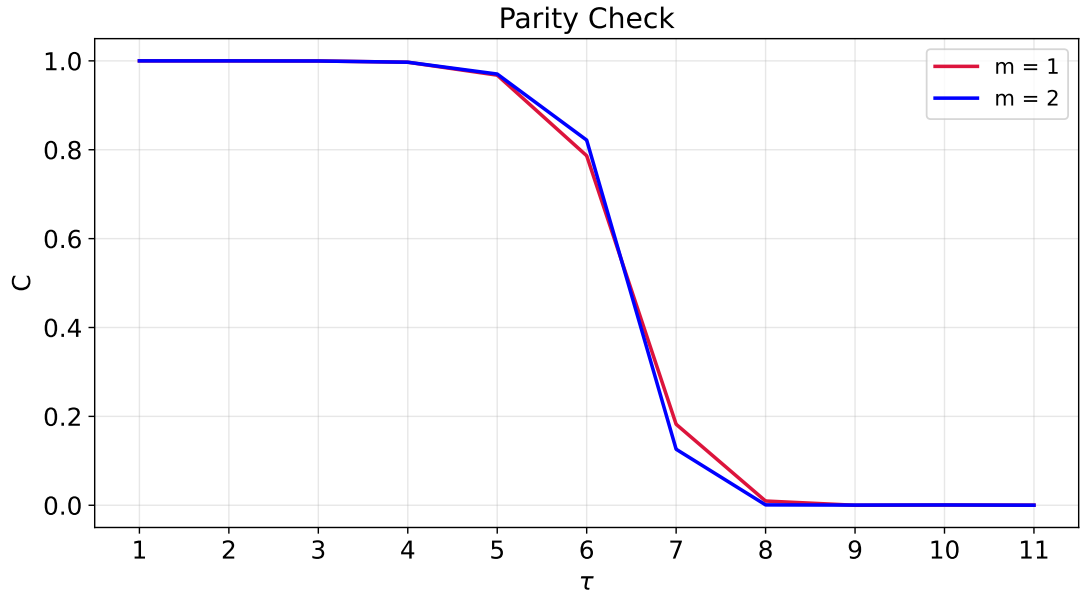

Figure 6: Parity Check capacity $C(\tau)$ vs. delay τ. Both m=1 and m=2 models display nearly identical nonlinear memory performance. The parameters are $dt = 10$, $\chi = 1$, $\kappa = 0.1$, $\gamma = 0.05$, $\gamma_\phi = 0.05$ and $\Delta_b = 2$.

In Fig. 6, we show the PC capacity of both reservoirs with increasing τ. Contrary to our expectation, we observe that the two-photon reservoir does not result in a clear improvement over the single-photon one, and both models perform competitively. We also verified this behavior for several different sets of loss parameters $\kappa, \gamma, \gamma_\phi$, and found that the two-photon model does not show a consistent and promising improvement over the single-photon model for the parameter sets considered. However, it is evident that similar to the single-photon JC reservoir [1], the two-photon JC reservoir also has a better nonlinear capacity than the linear one.

The expectation values of the observables in eq. 3.2 are linear combinations of the reduced density matrix (r.d.m) elements of the bosonic mode. For example, $\langle a^\dagger \rangle$ can be written as a function of the off-diagonal elements of the bosonic r.d.m. i.e. $\langle a^\dagger \rangle \equiv f(\rho^b_{0,1}, \rho^b_{1,2}, \rho^b_{2,3}, ..)$, where $\rho^b_{i,j}$ is the (i,j)th element of the bosonic r.d.m ρ^b. Instead of using these higher order bosonic operators as observables, we directly use the elements of ρ^b as features to investigate the memory capacity of the

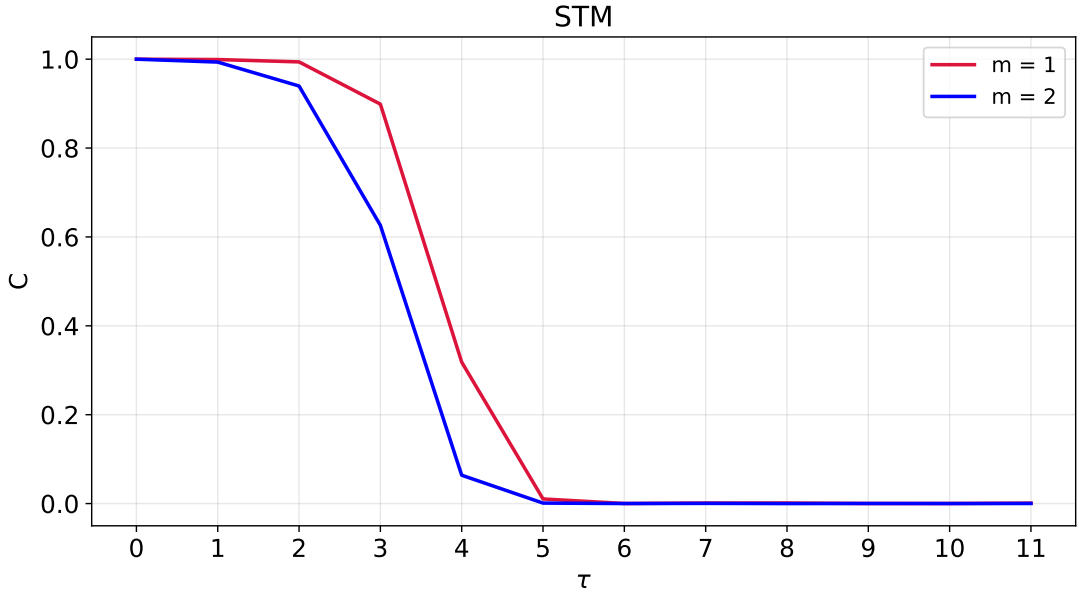

Figure 7: Short-Term Memory capacity $C(\tau)$ of single and two-photon JC model vs. delay τ, when considering $\{\mathrm{Re}(\rho^b_{i,j}), \mathrm{Im}(\rho^b_{i,j})\}$ as output features. The parameters are $dt = 10$, $\chi = 1$, $\kappa = 0.1$, $\gamma = 0.05$, $\gamma_\phi = 0.05$ and $\Delta_b = 2$.

reservoirs. As before, the real and imaginary parts of $\rho^b_{i,j}$ are treated as separate features. For a 20×20 dimensional r.d.m., this gives $400 \times V$ features for each input. The corresponding STM and PC capacities are shown in Figs. 7 and 8, respectively. We find that the linear capacity is again higher for the single-photon JC model, while the two-photon JC model shows a better nonlinear memory capacity than the single-photon model, and this observation remains true for other loss rates as well which are different than that shown in the figures. In particular, using the higher-order moments instead of the r.d.m. elements slightly improves the STM capacity of both reservoirs. For the PC task, the nonlinear capacity of the single-photon reservoir improves significantly, whereas the performance of the two-photon model remains relatively unchanged. These results suggest that the benchmarking of memory in QRC depends not only on the intrinsic memory of the reservoir dynamics, but also on how the information is mapped to the readout features.

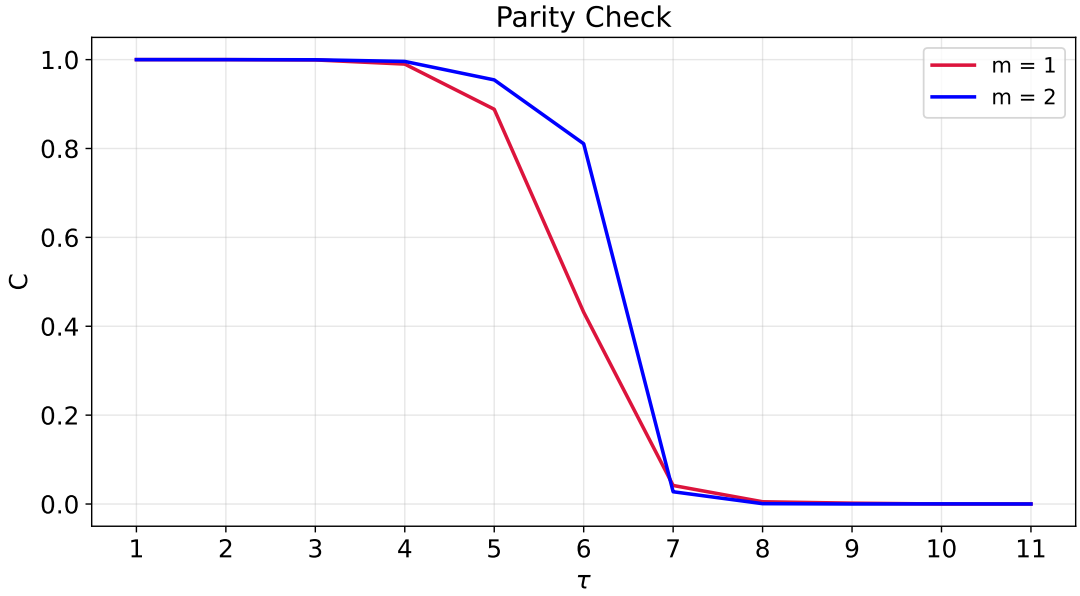

Figure 8: Parity Check capacity $C(\tau)$ of single and two-photon JC model vs. delay τ, when considering $\{\mathrm{Re}(\rho^b_{i,j}), \mathrm{Im}(\rho^b_{i,j})\}$ as output features. The parameters are $dt = 10$, $\chi = 1$, $\kappa = 0.1$, $\gamma = 0.05$, $\gamma_\phi = 0.05$ and $\Delta_b = 2$.

5 Conclusions

In this work, we investigated the potential of the two-photon Jaynes-Cummings model as a physical quantum reservoir computer and compared its performance for linear/nonlinear memory benchmarks against the standard single-photon interaction model. By modeling open system dynamics via the Lindblad master equation under continuous classical driving, we verified that the reservoir satisfies essential nonlinear input-processing, echo-state and fading-memory properties required for temporal time-series processing. Evaluations of memory tasks revealed distinct behaviors between the two models:

- Short Term Memory task (linear memory): The single-photon model consistently outperforms the two-photon model across delay steps $\tau > 1$. This aligns with theoretical expectations, as higher nonlinearity of two-photon reservoir may preserve nonlinear representations of inputs more effectively than the linear one.
- Parity Check task (nonlinear memory): Contrary to our expectations that increasingly nonlinear interaction would enhance complex pattern processing, both models demonstrated similar nonlinear memory capacity under the parameter regime $\kappa = 0.1$, $\gamma = \gamma_\phi = 0.05$. However, when using bosonic reduced density matrix elements as observables, PC capacity of two-photon reservoir is better than the single-photon reservoir.

These findings indicate that the memory benchmark we use, depends not only on the intrinsic dynamics of the reservoirs, but also on the choice of features used in the readout layer. In particular, higher nonlinearity of the Hamiltonian or readout operators does not automatically translate to superior performance in nonlinear temporal tasks. Future investigations will focus on:

- Systematically scanning the parameter space by sweeping the interaction coupling strength χ and qubit-boson detuning $\omega_b - \omega_d$,to investigate whether the observed differences between the two reservoirs remain valid in other regions of the parameter space.
- Exploring alternative, experimentally accessible readout feature sets and systematically sweeping dissipation parameters $(\kappa, \gamma, \gamma_\phi)$. This will allow us to verify whether increased interaction complexity genuinely fails to improve nonlinear performance, ensuring that our conclusions hold robustly across diverse reservoir parameter regimes.
- Comparing the performance of both reservoirs for an actual chaotic time-series prediction. This could provide further insight into the relationship between memory capacity and predictive performance.
- Understanding how to evaluate the intrinsic memory of the two reservoirs independently of the choice of readout features. This may help separate the memory arising from the reservoir dynamics itself from the effects introduced by the feature mapping.

Acknowledgments

This work was supported by the SURF@IFISC fellowship. I gratefully acknowledge the Institute for Cross-Disciplinary Physics and Complex Systems (UIB-CSIC) for providing this opportunity, with special thanks to Daniel Ruiz-Reynés for organizing the fellowship program.

My deepest gratitude goes to my supervisor, Sreetama Das, for her constant mentorship, patient guidance, and effective coordination of this project from day one. I would also like to express my sincere thanks to Roberta Zambrini for her senior supervision and valuable direction.

References

[1] Sreetama Das, Gian Luca Giorgi, and Roberta Zambrini. Quantum reservoir computing in jaynes-cummings models: Nonlinear memory and time-series prediction. *Phys. Rev. Res.*, 8:023148, May 2026.

[2] Keisuke Fujii and Kohei Nakajima. Harnessing disordered-ensemble quantum dynamics for machine learning. *Phys. Rev. Appl.*, 8:024030, Aug 2017.

[3] Johannes Nokkala, Rodrigo Martínez-Peña, Gian Luca Giorgi, Valentina Parigi, Miguel C. Soriano, and Roberta Zambrini. Gaussian states of continuous-variable quantum systems provide universal and versatile reservoir computing. *Communications Physics*, 4(1):53, Mar 2021.

[4] L. C. G. Govia, G. J. Ribeill, G. E. Rowlands, H. K. Krovi, and T. A. Ohki. Quantum reservoir computing with a single nonlinear oscillator. *Phys. Rev. Res.*, 3:013077, Jan 2021.

[5] Guillem Llodrà, Pere Mujal, Roberta Zambrini, and Gian Luca Giorgi. Quantum reservoir computing in atomic lattices. *Chaos, Solitons Fractals*, 195:116289, 2025.

[6] Jonas Larson and Themistoklis Mavrogordatos. *The Jaynes–Cummings Model and its Descendants (Second Edition)*. 2053-2563. IOP Publishing, 2024.

Modeling Opinion Polarization: From Binary Choices to Continuous Spectra

Ángel Cáffaro Mendoza, Antonio Fernández Peralta
Instituto de Física Interdisciplinar y Sistemas Complejos, IFISC (CSIC-UIB)
Campus Universitat de les Illes Balears, E-07122 Palma de Mallorca, Spain

Abstract

We study a collection of agent-based opinion-dynamics models spanning discrete binary choices and continuous opinion variables. We first reproduce the qualitative behavior of the voter, Kirman, and q-voter models, including consensus, stochastic switching, and symmetry-breaking transitions. We then analyze the Deffuant model and show how the confidence bound controls the emergence of polarized opinion clusters. To connect discrete and continuous descriptions, we introduce a time averaged opinion variable for the Kirman model. Finally, we investigate the Dandekar biased assimilation model on two-island networks with a deterministic and a random generation of interactions, this last case generating a much richer dynamic.

1 Introduction

Our choices, political views, and behaviors are constantly shaped by the endless exchange of opinions around us. Whether through casual chats or algorithmic feeds, our perspectives adapt, polarize, or fade as we process new information. Understanding how these tiny daily interactions build into large-scale societal trends is essential for grasping how social movements form, how public debate evolves, and how modern democracies function. For this reason, opinion dynamics has become a core focus across political science, governance, marketing, and sociology, driving researchers to explore how populations reach consensus, how networks spread ideas, and how online platform algorithms accelerate polarization.

Addressing these questions requires tools beyond traditional qualitative sociology. Computational social science fills this gap by blending sociological theory with applied mathematics and statistical physics. This field generally balances two approaches: data-driven exploration (analyzing massive real-time datasets from digital platforms) and model-driven simulation (using agent-based models where simulated individuals follow mathematical interaction rules). Ideally, empirical data and computational modeling inform each other to provide a complete picture of how opinions evolve.

However, gathering reliable data on human opinions is notoriously difficult. Unlike physical measurements, an opinion is subjective and converting fluid thoughts into numbers often distorts them. Traditional surveys suffer from small sample sizes, self-reporting bias, and public hesitation. Elections offer valuable snapshots, but they are discrete events rather than continuous processes. Meanwhile, social media data analyzed via natural language processing is notoriously noisy, demographic-biased, and often lacks underlying network context.

Because direct observation remains fragmented, computer simulations have become the main tool for investigating opinion dynamics. By translating sociological theories into precise mathematical rules and running them millions of times, researchers can observe emergent patterns impossible to capture in a lab.

This approach draws heavily on statistical physics. Today's agent-based models treat individuals as nodes in a network, modeling their opinions as discrete choices (e.g., yes/no) or continuous spectrums. Over time, simulated interactions drive the system toward consensus, fragmentation, or extreme polarization and they show that complex collective behaviors can emerge from simple local rules

The true strength of these models lies in their versatility. They allow researchers to safely test scenarios that are impossible in the real world, such as measuring the impact of broadcast media, testing how algorithmic filtering creates echo chambers, or tracking how people sever ties with those who disagree. Given their mathematical similarities to epidemic spreading, these models also draw from epidemiology to explain information cascades.

While these systems rely on simplified abstractions, growing computational power and new experimental designs continue to refine them. Researchers are now integrating controlled digital network experiments with human participants, and even autonomous bots, to test whether these mathematical rules mirror real-world human behavior.

2 Theoretical model

As we said there are two main different approaches, one of them is using a discrete model, where all the different agents have a limited amount of possible states, usually 2, that could be representing left or right in a political context, or a continuous model, where the opinion of each agent can be any number between a boundary, typically between 0 and 1.

2.1 Discrete models

2.1.1 Voter

Throughout this project we will study and replicate many different models, the first one to get a grasp of the topic is going to be the voter model

The rule set that defines the evolution of the model is very simple, we have N number of agents, each one has a determined q number of neighbors, each time step of the model we randomly choose one of the agents and choose one of its neighbors, then the agent copies the opinion of the neighbor.

This model, with enough evolution time, ends up getting to a final state where all the agents have the same value, since there is no random switching between states, it is not able to get out of it.

2.1.2 Kirman

The Kirman model, also known as the ants model, now introduces the possibility of a random switching, avoiding getting the model stuck with all the agents in the same state.

It was developed in an effort to try to model a unique behavior observed in an ant colony, when they were presented with two identical food sources, they would choose one of them but then randomly start changing between both. Later it was also used to explain other phenomena like humans choosing restaurants.

The rule set of evolution is a little different, now we have to randomly choose 2 agents from all of them, the first will be the one we will potentially change the opinion, and the other can be considered the neighbor. Next, with a probability of ε it will change its value. If it didn't change value, with a probability of $1 - \delta$ it will copy the neighbor opinion. The ε is introduced to avoid the system getting stuck, and the δ represents the probability of two ants meeting and heading to the same food source.

2.1.3 Q voter

Q voter involves different models related to looking at a number Q of neighbors and some probabilities of switching.

- **Anti-conformity I**: In this first one we select one agent and other Q agents that we will call neighbors. If all the neighbors have the same opinion and it is different from the the first agent we selected it will change and adopt theirs. If the neighbors opinion is the same as the

agent we selected it has a probability p of switching value.

- **Anti-conformity II**: This second one is the same rule set as the anti-conformity I but now, if the all the neighbors have a different opinion from the selected agent, instead of always switching it has a probability of 1-p of happening.

- **Independence**: This last one is the most different one, if all the neighbors have the same opinion and it is different from the agent we chose it will have a probability of 1-p of switching as in anti-conformity II. If this conditions did not happen, independently of the opinions of the neighbors, the agent has a p/2 probability of switching state.

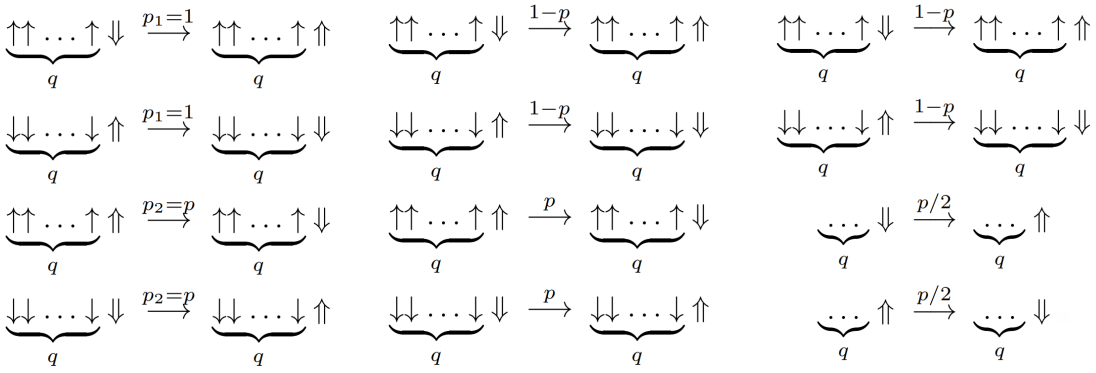

(a) Anti-conformity I (b) Anti-conformity II (c) Independence

Figure 1: Rule sets for the different Q voter models [4]

2.2 Continuous models

2.2.1 Deffaunt

Starting with the first continuous model, the one proposed by Deffaunt introduces a rule that allows interaction only with the agents with a close opinion. First we select two agents at random and we check if $|x_i(t) - x_j(t)| < \varepsilon$, if it is fulfilled, the opinion of both agents gets updated in the following way:

$$\begin{aligned} x_i(t+1) &= x_i(t) + \mu[x_j(t) - x_i(t)] \\ x_j(t+1) &= x_j(t) + \mu[x_i(t) - x_j(t)] \end{aligned} \tag{2.1}$$

2.2.2 Dandekar

This model is the most different one out of all the other model we have talked about, the evolution of all the agents only depends on the previous state of the system and the all the agents are updated at the same time, getting rid of any tipe of stochasticity. This allows for the model to be studied through mathematical theorems and development as the authors of the model did [3]. The equation is the following:

$$x_i(t+1) = \frac{w_{ii}x_i(t) + (x_i(t))^{b_i}s_i(t)}{w_{ii} + (x_i(t))^{b_i}s_i(t) + (1 - x_i(t))^{b_i}(d_i - s_i(t))} \tag{2.2}$$

With this definitions:

$$s_i(t) := \sum_{j \in N(i)} w_{ij}x_j(t) \qquad d_i := \sum_{j \in N(i)} w_{ij} \tag{2.3}$$

The parameter w is the interaction matrix, having the information of even the self interaction;

b is the bias parameter, it makes the agents weight more the confirming evidence of their opinions rather than the disconfirming one.

3 Results and discussion

Simulating the voter model not only is easy, but it is also the most simple out of all the models. It is still a probabilistic model, so each simulation will be different, and it will randomly get more on the upper side or the lower, but as it goes further into one side, the probability of keeping going in the same direction rises up until it gets stuck there.

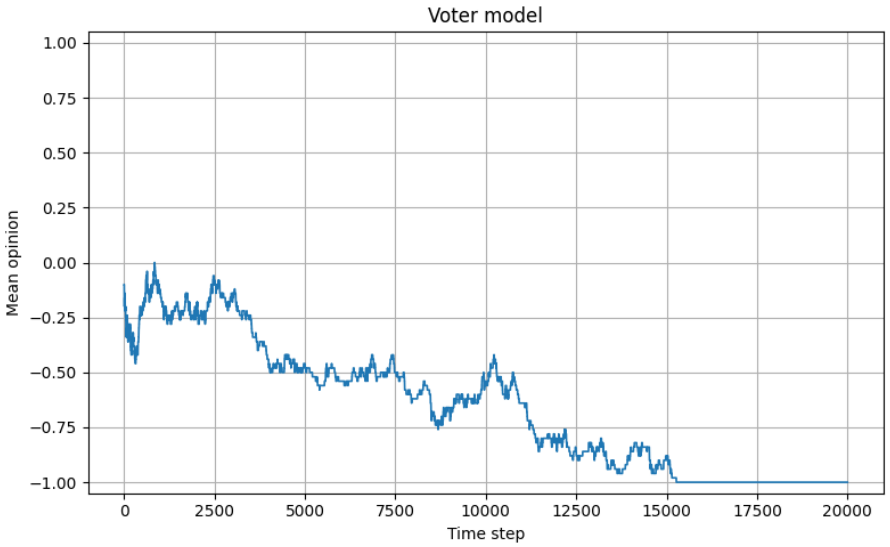

Figure 2: N = 100, 4 neighbors

In this graph we are taking a look at the evolution of the mean opinion as a function of the time steps. The mean opinion is the sum of all the agents states, and then it is divided by the number of agents. In our case, the initial condition consists of each agent randomly choosing 1 or -1, so at the first step it is close to 0, if all the agents then end up in the state 1, the mean opinion would be 1. Each time step represents a random choosing of an agent and then applying the steps of the model. In the particular case of the simulation in Figure (2), we can see it going down until it gets stuck in the case of having all the agents in the -1 state.

The next model we simulated was the ants model. In the original paper [1] they made a graph about the distribution of the agents for different values of the parameters ε and δ, so we made a simulation to check those values.

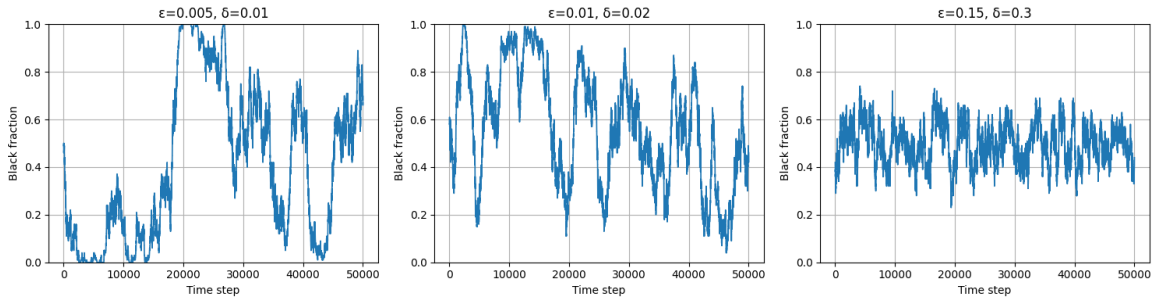

Figure 3: Ant model simulations for values of $\varepsilon = 0,005$ $\delta = 0,01$, $\varepsilon = 0,01$ $\delta = 0,02$ and $\varepsilon = 0,15$ $\delta = 0,3$, all with N = 100

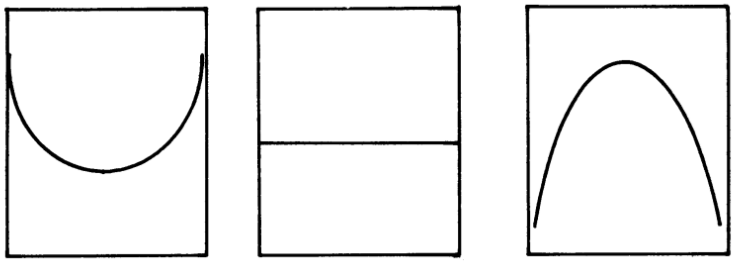

Figure 4: Theoretical distribution of the agents as a function of the black fraction for the same values of ε and δ as Figure(3)

In Figure(4) what we can see is that for the first set of values of ε and δ is more probable to find all the agents either in state 0 or state 1 and less probable in a mix with a mean state of 0,5. Looking at the simulated results in Figure(3) we can see that as the model evolves in time, the distribution presented in the original paper is fulfilled, and so it is for the other sets of values.

We continued by exploring a continuous model, the Deffaunt.

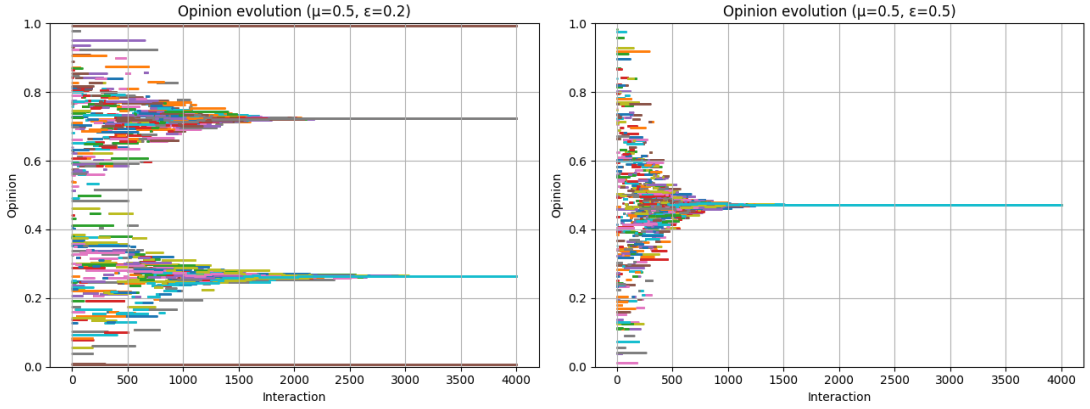

Figure 5: Deffaunt model simulations for values of $\mu = 0.5, \varepsilon = 0.2$ and $\mu = 0.5, \varepsilon = 0.5$ both with N = 100

As we discussed earlier, the parameter ε here represents the amount of difference in opinion you can have with someone and still take into account their opinion, so if we take a look at Figure(5), we can see how a low value of ε ends up polarizing all the agents, making two different groups, one closer to 1 and the other closer to 0, we even have two outlier agents , one exactly at 1 and the other exactly at 0, this happens because the majority of the agents quickly gather closer to those polarization zones, so if this ones don't interact quickly they run out of possible agents to interact with and they will remain on their opinion forever.

We made the ants model and the Deffaunt model simulations because we wanted to find a similarity between both models. In order to do it, first we needed a variable for the ants that is continuous, so we chose this one:

$$x_i(T) = \frac{1}{T}\sum_{t=1}^{T} s(t) \tag{3.1}$$

With this we can see the evolution in time of the opinion of each individual agent and it is a continuous variable.

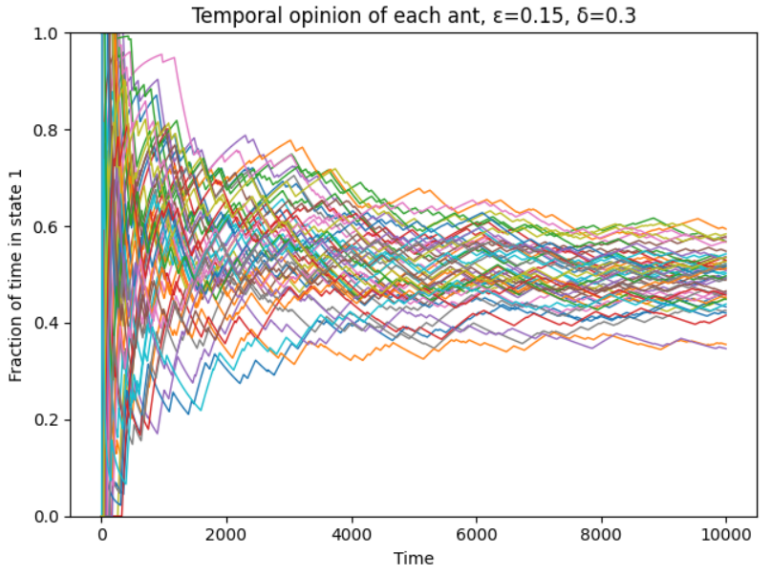

Figure 6: $\varepsilon = 0.15$, $\delta = 0.3$ and N = 50

Doing once again the simulations we already did but now plotting this new variable let us see that the average opinion of the ants tends to 0.5 as the simulations keeps going.

Since this model treats evenly all the agents, we would need a more complex approach to be able to make a parallelism between both systems and find something similar to polarization.

Heading now to the Q voter model, we started by doing a simulation of the Anti-conformity I.

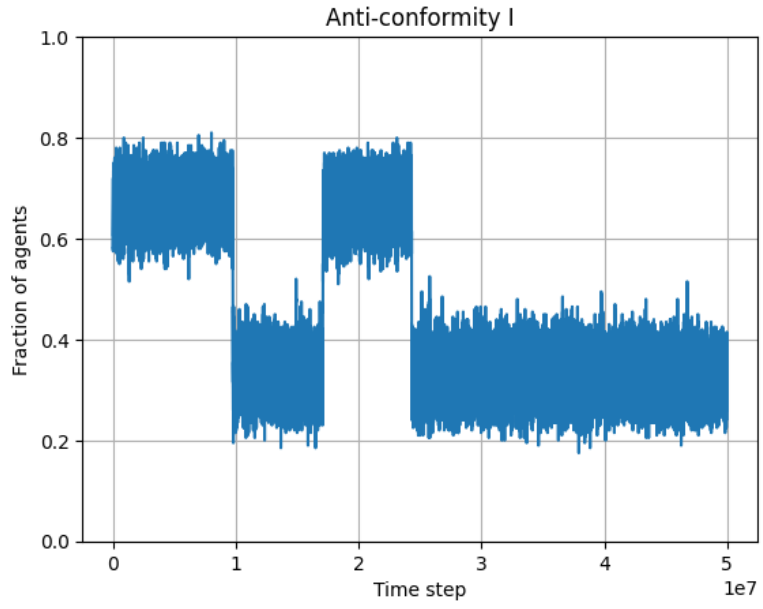

Figure 7: Anti-conformity I model with N = 200, Q = 7 and p = 0,5

These are the same result obtained in the paper [4], and we can see the model switching between two stable regimes, one above 0.5 and the other below. With this we might wonder how the stable regimes evolve as we sweep the parameters p and Q.

As we can see, the evolution of those stable regimes has the form of a pitchfork that changes depending on the parameter q. We made a simulation for q = 3 and we plotted the absolute value,

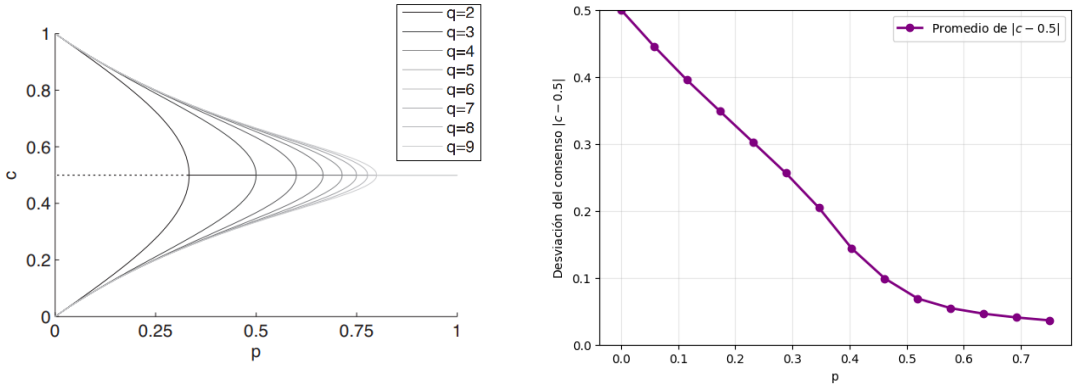

(a) Theoretical pitchfork for different q and p values

(b) Simulated absolute value of the fraction for q = 3

Figure 8: Comparison between the theoretical values and the simulated results

so we can only see one side of the pitchfork. The part that connects the branch to the stable value at 0.5 is not as sharp as the theoretical graph because we have some finite size limitations, but in the limit where it tends to infinity, it should match.

Heading into the most interesting one, the Dandekar, we are going to start by trying to get the numerical simulations of a theorem they proved. The theorem is the following:

Theorem 1. *Let $G = (V_1, V_2, E, w)$ be a (n, n, p_s, p_d)-two-island network. For all $i \in V = V_1 \cup V_2$, let $w_{ii} = 0$. For all $(i, j) \in E$, let $w_{ij} = 1$. Assume for all $i \in V_1$, $x_i(0) = x_0$, where $\frac{1}{2} < x_0 < 1$. Assume for all $i \in V_2$, $x_i(0) = 1 - x_0$. Assume for all $i \in V$, the bias parameter $b_i = b > 0$. Then,*

1. *(Polarization) If $b \geq 1$, $\forall i \in V_1$, $\lim_{t\to\infty} x_i(t) = 1$, and $\forall i \in V_2$, $\lim_{t\to\infty} x_i(t) = 0$.*
2. *(Persistent disagreement) If $1 > b \geq \frac{2}{h_G+1}$, then there exists a unique $\hat{x} \in \left(\frac{1}{2}, 1\right)$ such that $\forall i \in V_1$, $\lim_{t\to\infty} x_i(t) = \hat{x}$, and $\forall i \in V_2$, $\lim_{t\to\infty} x_i(t) = 1 - \hat{x}$.*
3. *(Consensus) If $b < \frac{2}{h_G+1}$, then for all $i \in V$, $\lim_{t\to\infty} x_i(t) = \frac{1}{2}$.*

It was also defined these values:

- $h_G = p_s/p_d$
- $\hat{x}(s, b) := \frac{s^{1/(1-b)}}{s^{1/(1-b)}+(1-s)^{1/(1-b)}}$
- s is the time-invariant weighted average of the opinions of all sources in the individual's environment.
- V_1 and V_2 are groups of agents with n individuals each.
- E is the connection between agents, and w is the weight of those connections.
- p_s is the amount of connections each agent has with other agents from the same isle and p_d is the connections with agents from the other isle.

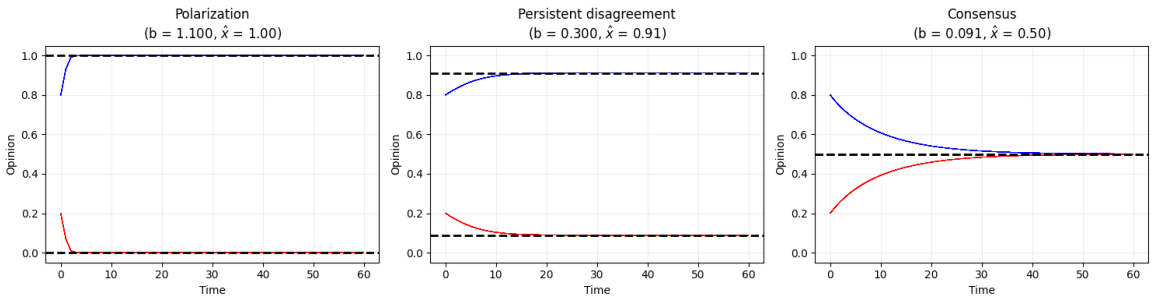

Figure 9: Simulations of the Dandekar model with N = 200, $p_s = 0.3$ and $p_d = 0.03$

From the results that we have obtained we can see the three distinct regimes that the theorem speaks about. The first one, when b is greater than one, the two different initially separated isles end up polarizing completely towards 1 or 0, depending on which value is closer. If b is instead between 1 and a number depending on the amount of connections, we now still find both isles getting separated and going towards a fixed value, but this time the value is not the maximum, it is between 0,5 and 0 or 1, called persistent disagreement. Lastly, if b is below a certain threshold, now both isles converge to the consensus of 0,5.

This model uses the exact value of p_s and p_d for each agent, this means that all the agents on each isle have the exact number of connections with the same isle and with the other isle. With this in mind, we tried making a little change to the model to see how it behaves. Instead of this type of connection, now p_s and p_d is a probability of making a connection, for example, if we have an isle with 100 agents, and p_s of 0.3, instead of all the agents having 30 connections, some agents will have 29, or 31, and so on.

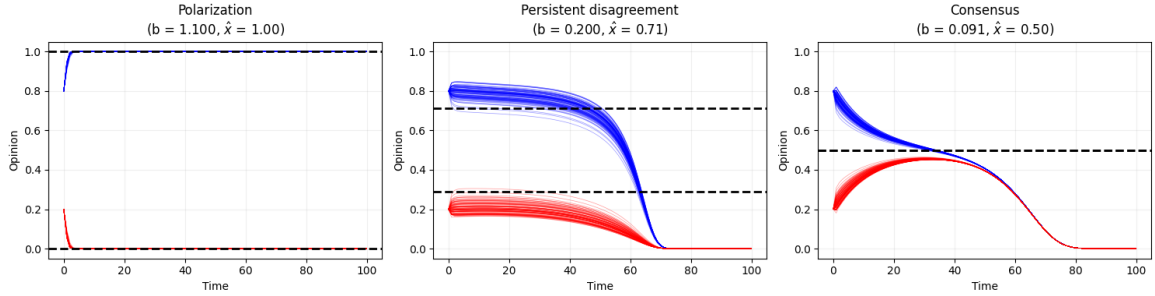

Figure 10: Simulations of the Dandekar model with random interactions, N = 200, $p_s = 0.3$ and $p_d = 0.03$

With these new interactions, now the model behaves quite differently; the first regime, the polarization one, is the same as before, but with the persistent disagreement, now instead of all the agents going through the same path towards two different stable points, they separate a little bit in the first moments of the simulation and then they all gather at the value 0 or 1 randomly. The same thing happens in the consensus regime, instead of getting into 0.5 they all get to either 0 or 1.

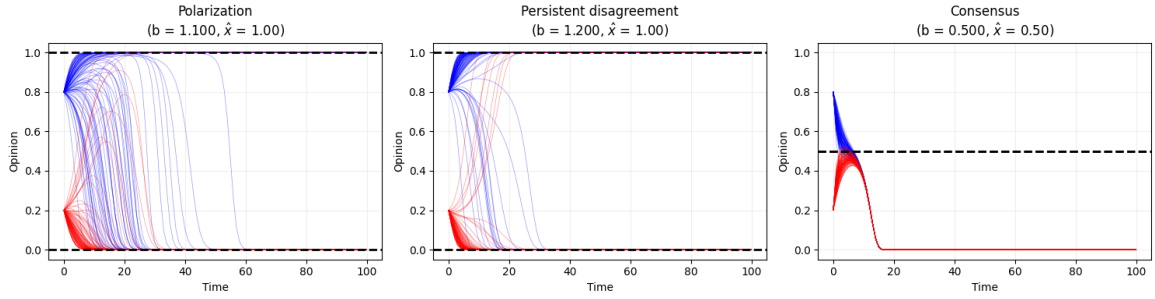

Figure 11: Simulations of the Dandekar model with random interactions, N = 200, $p_s = 0.2$ and $p_d = 0.2$

We also tried changing a little bit some parameters to see how it behaves, and we first started by using the same value for p_s and p_d, in this case 0,2. First of all, with the values for p_s and p_d equal or a higher value of p_d than p_s is not really possible to make the disinction of three different regimes as in the original model since h_G is equal or greater than 1 and therefor the persistent disagreement regime does not exist, but we can see how it is affected by b values even higher than 1. For lower values of b, the system quickly gathers together and then moves to either 1 or 0 as we saw before, but if we increase b up to 1.1, now a big part of both isles get to their closest polarization value, but some of the agents move to the other. If we increase the b value to 1.2, the amount of agents moving to the other isle polarization value gets decreased, so we can conclude

that even if the amount of connections is the same in both isles, a high value of bias ends up in a polarization regime.

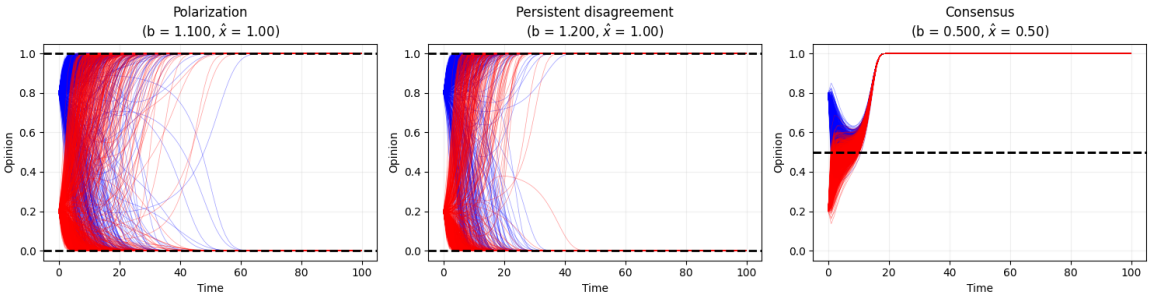

Figure 12: Simulations of the Dandekar model with random interactions, N = 200, p_s = 0.01 and p_d = 0.01

If we now reduce the value of p_s and p_d to 0.01 both we can see some big differences. The values of b = 1.1 and b = 1.2 are very similar and in both cases, both isles get very spread and a mix of the two ends up in 1 and in 0. This tells us that the lower the values of p the higher we need b to still end up in the polarization regime. For b = 0.5 we have the same as Figure(11), but wider in the first steps.

4 Conclusions

We explored opinion dynamics from two main angles: discrete binary models and continuous opinion models. Starting with the classic voter model, we saw how simple local imitation can naturally nudge a population toward consensus. Adding Kirman's stochastic switching kept the system from getting permanently trapped in one state, creating a far richer distribution of outcomes. Meanwhile, the q-voter model showed that even tiny tweaks to individual update rules can completely shift collective behavior, sparking symmetry-breaking and bistability.

Turning to continuous models, the Deffuant model highlighted just how critical the confidence bound ε is. When ε is small, people only talk to those who already agree with them, driving the population into isolated clusters and deep polarization. Raising that threshold opens up dialogue across broader groups, helping disparate opinions merge. We also introduced a time-averaged opinion variable to the Kirman model, bridging the gap between discrete steps and continuous trends.

We paid special attention to the Dandekar model of biased assimilation. On a fixed two-island network, our simulations matched theoretical predictions across three clear regimes: heavy bias breeds total polarization, moderate bias sustains ongoing disagreement, and low bias leads to consensus. When people selectively process information, the underlying network structure determines the outcome.

Regarding the same model, swapping fixed connections for probabilistic ones fundamentally changes the outcomes. Degree fluctuations break the symmetry of idealized models, causing agents on the very same island to end up in completely different directions. Instead of settling into stable disagreement or consensus, the system often gets pushed to extreme ends (0 or 1). This effect is especially pronounced in sparse networks with low connection probabilities, where random variations carry far more weight.

Overall, the results emphasize that macroscopic polarization is not determined by the individual update rule alone. The topology and heterogeneity of the interaction network can change the collective dynamics and even alter the qualitative regimes predicted by an idealized model. Moving forward, the most promising next steps are systematically testing how network size, degree distribution, and connection probabilities alter these dynamics, while building a formal mathematical description between discrete stochastic models and continuous opinion flows.

Acknowledgments

This work was supported by the SURF@IFISC fellowship. I would also like to thank my tutor during this research, Antonio Peralta, for his work and time teaching me this area of the complex systems, Daniel Ruiz for coordinating all the program and all the teachers that gave us talks of different topics.

References

[1] Alan Kirman, Ants, Rationality, and Recruitment, *The Quarterly Journal of Economics*, Volume 108, Issue 1, February 1993, Pages 137–156, https://doi.org/10.2307/2118498

[2] Peralta, A. F., Kertész, J., & Iñiguez, G. (2025). Opinion dynamics in social networks: From models to data. En T. Yasseri (Ed.),*Handbook of Computational Social Science* (pp. 384-406). Edward Elgar Publishing. https://doi.org/10.4337/9781802207309

[3] Dandekar, P., Goel, A., & Lee, D. T. (2013). Biased assimilation, homophily, and the dynamics of polarization. *Proceedings of the National Academy of Sciences*, 110(15), 5791-5796. https://doi.org/10.1073/pnas.1217220110

[4] Nyczka, P., Sznajd-Weron, K., & Cisło, J. (2012). Phase transitions in the q-voter model with two types of stochastic driving. *Physical Review E, 86*(1), 011105. https://doi.org/10.1103/PhysRevE.86.011105

[5] Peralta, A. F., Carro, A., San Miguel, M., & Toral, R. (2018). Analytical and numerical study of the non-linear noisy voter model on complex networks. *Chaos, 28*(7), 075516. https://doi.org/10.1063/1.5030112